
Doctoral Dissertations


Student Theses and Dissertations

Summer 2016

Modeling and control of fuel cell-battery hybrid energy sources

Nima Lotfi

Follow this and additional works at: https://scholarsmine.mst.edu/doctoral_dissertations

 Part of the [Electrical and Computer Engineering Commons](#), and the [Mechanical Engineering Commons](#)

Department: Mechanical and Aerospace Engineering

Recommended Citation

Lotfi, Nima, "Modeling and control of fuel cell-battery hybrid energy sources" (2016). *Doctoral Dissertations*. 2513.

https://scholarsmine.mst.edu/doctoral_dissertations/2513

This thesis is brought to you by Scholars' Mine, a service of the Missouri S&T Library and Learning Resources. This work is protected by U. S. Copyright Law. Unauthorized use including reproduction for redistribution requires the permission of the copyright holder. For more information, please contact scholarsmine@mst.edu.

MODELING AND CONTROL OF FUEL CELL-BATTERY HYBRID ENERGY
SOURCES

by

NIMA LOTFI YAGIN

A DISSERTATION

Presented to the Faculty of the Graduate School of the
MISSOURI UNIVERSITY OF SCIENCE AND TECHNOLOGY

In Partial Fulfillment of the Requirements for the Degree

DOCTOR OF PHILOSOPHY

in

MECHANICAL ENGINEERING

2016

Approved
Robert G. Landers, Advisor
S.N. Balakrishnan
Jonghyun Park
Mehdi Ferdowsi
Jonathan W. Kimball

© 2016

Nima Lotfi Yagin

All Rights Reserved

PUBLICATION DISSERTATION OPTION

This dissertation contains the following four articles, formatted in the style used by the Missouri University of Science and Technology:

Paper I: N. Lotfi, P. Fajri, S. Novosad, J. Savage, R.G. Landers, and M. Ferdowsi, “Development of an Experimental Testbed for Research in Lithium-ion Battery Management Systems,” *Energies*, vol. 6, pp. 5231 – 5258, 2013.

Paper II: N. Lotfi, R.G. Landers, J. Lie, and J. Park, “Reduced-order Electrochemical Model-based SOC Observer with Output Model Uncertainty Estimation,” under revision for publication in *IEEE Transactions on Control Systems Technology*.

Paper III: N. Lotfi, H. Zomorodi, and R.G. Landers, “Performance Characterization and Control-oriented Modeling of Open-cathode Fuel Cell Systems,” to be submitted to *Journal of Electrochemical Energy Conversion and Storage*.

Paper IV: N. Lotfi, H. Zomorodi, and R.G. Landers, “Active Disturbance Rejection Control for Voltage Stabilization in Open-Cathode Fuel Cells through Temperature Regulation,” under revision for publication in *Control Engineering Practice*.

ABSTRACT

Environmental, political, and availability concerns regarding fossil fuels in recent decades have garnered substantial research and development in the area of alternative energy systems. Among various alternative energy systems, fuel cells and batteries have attracted significant attention both in academia and industry considering their superior performances and numerous advantages. In this dissertation, the modeling and control of these two electrochemical sources as the main constituents of fuel cell-battery hybrid energy sources are studied with ultimate goals of improving their performance, reducing their development and operational costs and consequently, easing their widespread commercialization. More specifically, Paper I provides a comprehensive background and literature review about Li-ion battery and its Battery Management System (BMS). Furthermore, the development of an experimental BMS design testbench is introduced in this paper. Paper II discusses the design of a novel observer for Li-ion battery State of Charge (SOC) estimation, as one of the most important functionalities of BMSs. Paper III addresses the control-oriented modeling and analysis of open-cathode fuel cells in order to provide a comprehensive system-level understanding of their real-time operation and to establish a basis for control design. Finally, in Paper IV a feedback controller, combined with a novel output-injection observer, is designed and implemented for open-cathode fuel cell temperature control. It is shown that temperature control not only ensures the fuel cell temperature reference is properly maintained, but, along with an uncertainty estimator, can also be used to adaptively stabilize the output voltage.

ACKNOWLEDGMENTS

First of all, I would like to express my deepest gratitude to my advisor, Dr. Robert G. Landers, for giving me the wonderful opportunity of pursuing my PhD studies under his supervision and mentoring me. My doctoral studies at Missouri S&T have been extremely rewarding and I owe my success mainly to my advisor. I have always been able to count on his support whenever I came across an obstacle and his guidance and feedback have been instrumental during my journey as a PhD student. Finally, I am grateful to Dr. Landers for financially supporting me during these years through funding from the Department of Energy and Intelligent Systems Center.

I would also like to thank my committee members, Dr. S.N. Balakrishnan, Dr. M. Ferdowsi, Dr. J.W. Kimball, and Dr. J. Park. I am truly fortunate to have these wonderful scholars in my committee as they have been very helpful in my research progress. I have learnt a lot during my interactions with each and every one of them. Finally, I would like to thank Mitch Cottrell in Electronics Shop in Mechanical Engineering Department for his valuable guidance in regards to some of my experimental projects.

In the end, I would like to extend my appreciation to my father, my mother, and my sister. They have relentlessly supported me during these years and have been the main source of my encouragement. I owe my entire life to my family and I am indebted to them eternally for their love and support.

TABLE OF CONTENTS

	Page
PUBLICATION DISSERTATION OPTION.....	iii
ABSTRACT.....	iv
ACKNOWLEDGMENTS	v
LIST OF ILLUSTRATIONS.....	ix
LIST OF TABLES.....	xii
SECTION	
1. INTRODUCTION	1
1.1. LI-ION BATTERIES.....	2
1.2. OPEN-CATHODE PEM FUEL CELLS.....	4
REFERENCES.....	9
PAPER	
I. DEVELOPMENT OF AN EXPERIMENTAL TESTBED FOR RESEARCH IN LITHIUM-ION BATTERY MANAGEMENT SYSTEMS	10
ABSTRACT.....	10
1. INTRODUCTION.....	12
2. EXPERIMENTAL LI-ION BATTERY RESEARCH TESTBED	19
3. EXPERIMENTAL BATTERY CHARACTERIZATION AND MODELING	28
3.1. CHARACTERIZATION	28
3.1.1. Static Capacity Test	31
3.1.2. HPPC Test.....	33
3.1.3. Open-Circuit Voltage Test.....	36
3.2. MODELING.....	38
4. CELL BALANCING	43
4.1. RESISTIVE SHUNTING.....	44
4.2. SWITCHED CAPACITOR.....	45
4.3. DOUBLE-TIERED SWITCHED CAPACITOR.....	45
4.4. SINGLE-SWITCHED CAPACITOR.....	46
4.5. STEP-UP/BOOST CONVERTER.....	46

5. PROTECTION	48
6. INDICATION OF BATTERY STATES	54
7. SUMMARY AND CONCLUSIONS.....	57
REFERENCES	59
II. REDUCED-ORDER ELECTROCHEMICAL MODEL-BASED SOC OBSERVER WITH OUTPUT MODEL UNCERTAINTY ESTIMATION.....	63
ABSTRACT	63
1. INTRODUCTION.....	64
2. MODELING.....	70
3. SOC OBSERVER DESIGN.....	80
3.1. OBSERVER FORMULATION	80
3.2. EFFECT OF MEASUREMENT NOISE ON THE STATE ESTIMATION ...	86
3.3. IMPLEMENTATION RESULTS	89
4. IMPROVED SOC OBSERVER BASED ON OUTPUT MODEL UNCERTAINTY ESTIMATION	95
4.1. FORMULATION AND STABILITY ANALYSIS	95
4.2. SIMULATION RESULTS	101
5. SUMMARY AND CONCLUSIONS.....	110
REFERENCES	112
III. PERFORMANCE CHARACTERIZATION AND CONTROL-ORIENTED MODELING OF OPEN-CATHODE FUEL CELL SYSTEMS.....	116
ABSTRACT	116
1. INTRODUCTION.....	117
2. EXPERIMENTAL PERFORMANCE INVESTIGATIONS.....	125
3. MODELING.....	134
3.1. VOLTAGE.....	134
3.2. AIR DELIVERY SYSTEM DYNAMICS.....	140
3.2.1. Fan Operating Point Determination	140
3.2.2. Modeling Experimental Fuel Cell Fans	143
3.3. TEMPERATURE	146
3.4. PURGING.....	148
4. SUMMARY AND CONCLUSIONS.....	152

REFERENCES.....	153
IV. ACTIVE DISTURBANCE REJECTION CONTROL FOR VOLTAGE STABILIZATION IN OPEN-CATHODE FUEL CELLS THROUGH TEMPERATURE REGULATION	157
ABSTRACT	157
1. INTRODUCTION.....	158
2. TEMPERATURE CONTROL.....	163
2.1. EXPERIMENTAL SYSTEM.....	163
2.2. CONTROLLER DESIGN	163
2.3. OUTPUT-INJECTION OBSERVER DESIGN	168
2.4. TEMPERATURE CONTROLLER PERFORMANCE	173
3. VOLTAGE CONTROL	177
4. SUMMARY AND CONCLUSIONS.....	185
REFERENCES.....	186
SECTION	
2. SUMMARY, CONCLUSIONS, AND FUTURE WORK	189
2.1. SUMMARY AND CONCLUSIONS.....	189
2.2. FUTURE WORK	191
VITA	193

LIST OF ILLUSTRATIONS

Figure	Page
PAPER I	
1.1. Distribution of different battery technologies in the transportation sector during the last 30 years [3].	13
2.1. Characteristic curve for a 32 V rated Mega fuses from Littlefuse.	25
2.2. Single cell research platform with its schematic diagram.	26
2.3. Cell balancing research platform with its schematic diagram.	27
2.4. Battery pack research platform with its schematic diagram.	27
3.1. Battery charge profile.	30
3.2. Battery discharge profile.	30
3.3. Voltage and current evolution during discharge tests for static capacity determination.	31
3.4. State of charge (SOC) and capacity evolution during discharge tests for static capacity determination.	32
3.5. Hybrid pulse power characterization (HPPC) test profile [8].	34
3.6. Complete HPPC test sequence.	35
3.7. Battery voltage and SOC evolution during HPPC profile.	36
3.8. First step in open-circuit voltage tests.	37
3.9. Battery open-circuit voltage and internal resistance versus SOC.	38
3.10. First-order resistor-capacitor (RC) model with one-state hysteresis [25].	39
3.11. Equivalent circuit battery model [12].	40
4.1. Resistive shunting configuration.	44
4.2. Switched capacitor configuration.	45
4.3. Double-tiered switched capacitor configuration.	46
4.4. Single-switched capacitor configuration.	46
4.5. Boost converter configuration.	47
5.1. Equivalent-circuit battery model.	49
5.2. Experimental and modeled battery open-circuit voltage.	50
5.3. Comparison of different voltage levels during a discharge profile: (a) the whole profile; and (b) end of discharge.	51

PAPER II

2.1. OCP of (a) negative electrode and (b) positive electrode as a function of normalized surface concentrations [34, 35].	78
2.2. Voltages for P2D and reduced-order electrochemical models during (a) 0.2C, (b) 1C, (c) 3C, and (d) 5C constant current discharge tests.	79
3.1. Actual versus estimated output voltage for (a) 0.2C, (b) 1C, (c) 3C, and (d) 5C constant discharge tests with the output injection observer.	91
3.2. Actual versus estimated SOC for (a) 0.2C, (b) 1C, (c) 3C, and (d) 5C constant discharge tests with the output injection observer.	92
3.3. Actual versus estimated SOC when subject to current and voltage measurement noise with (a) $\kappa = 1000$, (b) $\kappa = 200$, and (c) $\kappa = 5000$, with the output injection observer.	93
3.4. SOC estimation MAPE values with increasing (a) current noise variance, (b) current bias, and (c) voltage noise variance with the output injection observer.	94
4.1. Actual versus estimated output voltage for (a) 3C and (b) 5C constant discharge simulations with the adaptive observer.	103
4.2. Actual versus estimated SOC for (a) 3C and (b) 5C constant discharge simulations with the adaptive observer.	104
4.3. Output model uncertainty coefficients identified offline and online for (a) 3C and (b) 5C current profiles.	105
4.4. HiL test bench for emulating HEVs.	106
4.5. Current profile and current profile time derivative for (a) UDDS and (b) HWFET drive cycles.	106
4.6. Actual versus estimated output voltage for (a) UDDS and (b) HWFET simulations with the adaptive observer.	108
4.7. Actual versus estimated SOC for (a) UDDS and (b) HWFET simulations with the adaptive observer.	109

PAPER III

2.1. Experimental air-forced open-cathode PEMFC system.	126
2.2. Fans' PWM command (a) in order to maintain the temperature profile (b) and the corresponding fuel cell voltage for 0.16 A cm^{-2} current density.	128
2.3. Fans' PWM command (a) in order to maintain the temperature profile (b) and the corresponding fuel cell voltage for 0.24 A cm^{-2} current density.	129
2.4. Fuel cell voltage during purging for test performed in Figure 2.2.	129
2.5. Fuel cell voltage during purging for test performed in Figure 2.3.	130

2.6. Output fuel cell voltage when changing the purge period from (a) 15 to 7.5 s, (b) 15 to 15 s, and (c) 15 to 30 s.	131
2.7. Output fuel cell voltage when changing the purge duration from (a) 600 to 300 ms, (b) 600 to 600 ms, and (c) 600 to 1200 ms.	132
3.1. Experimental and model fuel cell voltages with 50% fan PWM command.	140
3.2. Fans' performance curve and fuel cell pressure drop-air flow rate curves.	144
3.3. Validation results for fan rotational speed model versus experimental data.	145
3.4. Experimental and model temperatures for step changes in current density.	148
3.5. Anode pressure and hydrogen mass flow rate models versus experimental data during purge pulse.	151
PAPER IV	
2.1. (a) Controlled average fuel cell temperature, (b) fan duty cycle, and (c) output voltage for $i_{FC} = 0.2 \text{ A cm}^{-2}$	167
2.2. (a) Reference and estimated temperatures when using controller with temperature estimate from observer as feedback signal and corresponding (b) control signal and (c) output voltage.	175
2.3. Temperature tracking error and duty cycle for $i_{FC} = 0.2 \text{ A cm}^{-2}$ and (a) $q = 0.5$ and (b) $q = 5$	176
3.1. Fuel cell stack voltage regulation scheme.	178
3.2. Measured and reference voltages, estimated and reference temperatures, and temperature tracking error for (a) constant-temperature and (b) constant-voltage fuel cell operations.	182
3.3. Reference and measured (a) fuel cell voltage and (b) temperature for voltage regulation experiments.	183
3.4. Fuel cell voltage and temperature for voltage regulation at (a) $V_{FC,ref} = 22.5 \text{ V}$ and (b) $V_{FC,ref} = 23.5 \text{ V}$	184

LIST OF TABLES

Table	Page
PAPER I	
2.1. LiMnPO ₄ battery cell specification [22].	22
3.1. Battery capacity values.	32
PAPER II	
2.1. Reduced-order model parameters.	77
3.1. Maximum and minimum slopes in Eq. (38) and maximum bound for observer gain.	90
4.1. Observer computational time for UDDS and HWFET current profiles	109
PAPER III	
3.1. Experimental fuel cell system physical parameters	144
3.2. MAPE of pressure and mass flow rate models for data in Figure 3.5.	150

SECTION

1. INTRODUCTION

In the past few decades, there has been an increasing interest towards the employment of clean and sustainable energy sources in various applications. Although traditional fossil fuels such as gasoline and diesel have enabled the majority of industrial and transportation advancements, they introduce numerous concerns considering the political and economic implications of dependence on oil import, the environmental impacts such as global warming, and their sustainability issues. Therefore, federal regulations in recent years have mandated companies to invest their resources towards research and development of alternative and renewable energy sources to substitute their traditional counterparts. Among different such technologies, fuel cells and batteries have received a special attention both in industry and academia. These electrochemical energy sources offer efficient and clean operation and can be used to overcome the drawbacks of the traditional sources. Furthermore, they are the enabling technology behind some of the technological advancements in the past decades such as consumer electronics, portable applications, and the integration of renewable energy sources to the existing power grids. Fuel cells and batteries are also used alongside each other in hybrid energy sources to complement their individual advantages. Therefore, aiming to improve the performance and reduce the development and operational costs of these energy sources, this dissertation addresses modeling and control of fuel cells and batteries. More specifically, Li-ion batteries and open-cathode Polymer Electrolyte Membrane (PEM) fuel cells are considered in this dissertation.

1.1. LI-ION BATTERIES

Li-ion batteries are electrochemical energy storage devices that operate by converting the chemical energy of their material into electrical energy. They were first introduced in 1976 [1], and subsequently commercialized in cell phones and laptops by Sony Corporation in 1991 [2]. A typical Li-ion battery has three main domains: negative electrode, positive electrode, and separator. The most commonly-used material for the negative electrode is graphite, whereas the positive electrode is typically composed of a metal oxide such as Lithium Cobalt Oxide (LiCoO_2), Lithium Iron Phosphate (LiFePO_4), Lithium Manganese Oxide (LiMn_2O_4) or Lithium Nickel Manganese Cobalt Oxide ($\text{LiNiMnCoO}_2/\text{NMC}$), depending on the application. Furthermore, filler and binder materials are also added to both electrodes for structural integrity. The separator between the electrodes acts as an electron insulator. The electrodes and separator assembly are immersed inside an electrolyte, which is usually a lithium salt in an organic solvent. During discharge, in an intercalation process, lithium ions in the active material of the negative electrode diffuse to the surface where they transfer from the solid-phase to electrolyte-phase. They then travel via the mechanism of diffusion and migration to the positive electrode where they react with the active material and insert inside it. During this process, electrons released in the negative electrode travel through the external circuit to generate a flow of current. The processes occurring in the positive and negative electrodes are reversed during charging.

Li-ion batteries were first employed in portable consumer electronics; however, in recent years, they have become the mainstream energy storage solution in a majority of battery-powered applications. Specially, they are being extensively adopted in electrified transportation and stationary energy storage systems. Furthermore, they play an important

role in the integration of various renewable energy sources to existing power infrastructures. Li-ion batteries can also significantly improve the reliability and efficiency of the utility industry and reduce its operational and capital costs [3].

To ensure the safe and efficient performance of Li-ion batteries, they must be equipped with advanced management strategies. Typical functionalities of any Battery Management System (BMS) include measurement and monitoring, cell balancing, thermal and electrical protection, and state estimation. Paper I in this dissertation describes the development of an experimental Li-ion BMS research testbed. This testbed is intended to facilitate in-depth research on BMS design and implementation. In addition to a thorough literature review about Li-ion batteries and BMSs, various BMS subsystems are described and important practical considerations that need to be taken into account while designing an advanced BMS are introduced. Some of the capabilities of the research testbed are illustrated through experimental investigations. This paper not only provides a theoretical and practical review regarding Li-ion batteries and BMSs, it also sheds light on some of the current research problems in this field and proposes possible directions to overcome these challenges.

Paper II, on the other hand, focuses on one of the most important functionalities of BMSs, i.e. to predict the operating scope of the battery, usually expressed in terms of State of Charge (SOC). Accurate information about battery SOC is crucial in other BMS functionalities such as state of health estimation, cell balancing, and battery energy management, and can potentially result in improved utilization. The main challenge in determining a battery's SOC is the fact that SOC is not directly measurable, necessitating an estimation routine. In Paper II, an electrochemical model-based SOC estimation

methodology is proposed. More specifically, a modified reduced-order model based on the Single Particle (SP) approximation of the electrochemical model, suitable for the real-time implementation of SOC estimation, is employed in this work. This model, while maintaining some of the physical insight about the battery operation, provides a basis for an output-injection observer design to estimate the SOC. Output model uncertainties, originating primarily from the electrolyte-phase potential difference approximation and encountered mainly at higher discharge rates, are handled by incorporating an adaptation algorithm in the observer. Therefore, the proposed method, while being suitable for online implementation, provides an electrochemical model-based solution for battery SOC estimation over a wide range of operation. System stability and the robustness of the estimates given measurement noise are proved analytically using Lyapunov stability. Finally, accurate performance of the proposed SOC estimation technique is illustrated using simulation data obtained from a full-order electrochemical model of a Lithium Manganese Oxide (LMO) battery.

1.2. OPEN-CATHODE PEM FUEL CELLS

Fuel cells are devices that convert their fuel's chemical energy into electrical energy through electrochemical reactions. The produced electrical energy can be used to power different applications such as vehicles, electronic devices, household applications, and backup power sources in electric grids. Fuel cells have clean by-products (e.g., water); thus, they are nearly zero-emission energy devices. Also, due to the lack of moving parts, fuel cells are quiet energy sources and they produce higher energy density and efficiency, around 40% electric efficiency, than traditional engine/generator sets. As different types of fuel cells employ various conventional and alternative fuels such as hydrogen, ethanol, methanol, and natural gas, which can be generated from renewable

energy sources, the dependence on oil for mechanical and electrical energy production is further reduced. Finally, easy scalability and low maintenance costs make fuel cells very desirable energy sources.

Among different fuel cell types [4], PEM Fuel Cells (PEMFCs) have higher efficiency and power density, longer cell and stack life, lower electrolyte corrosion, and lower noise levels. The main advantage of PEMFCs is their low operating temperature, making them a great power source for portable applications such as consumer electronics and hybrid electric vehicles. PEMFCs use a solid polymer electrolyte which is usually made from a fluorinated sulfonic acid polymer. This Teflon-like electrolyte is a proton conductor and an electron insulator. At the anode, with the help of a platinum-based catalyst and during an oxidation reaction, hydrogen molecules are broken into electrons and hydrogen protons. The hydrogen protons travel across the membrane to the cathode surface where they react with oxygen molecules and electrons passing from the anode to the cathode through the external load in a reduction reaction and produce water. In order to achieve typical power requirements, multiple PEMFCs need to be stacked together. In addition to the PEMFC stack, auxiliary components are also required for the PEMFC operation. A complete PEMFC system consists of a cathode subsystem for air/oxygen supply and an anode subsystem for hydrogen supply.

Open-cathode PEMFCs differ from typical PEMFCs in that they have cathode channels exposed to atmosphere, whereas typical PEMFCs are usually operated with a closed-cathode structure. In closed-cathode PEMFCs, the air is supplied by a compressor at pressures from near ambient to approximately 6 atm. On the other hand, open-cathode PEMFCs are usually operated near atmospheric pressure with the air being supplied

either by convection or low-power fans. Higher pressures in closed-cathode PEMFCs require cathode pressure regulation in order to match the anode pressure [5]. However, in open-cathode PEMFC systems, due to near-atmospheric operating pressures, pressure regulation is not required. It should also be noted that although operating at higher pressures results in better performance and higher voltages, it induces considerable parasitic loads and cost (e.g., compressor, cooling system, humidification system). On the other hand, open-cathode fuel cells do not require humidification and are usually supplied with dry reactants. Their design and structure guarantee rapid humidification and ensure that enough water is kept in the membrane [6]. Therefore, open-cathode PEMFCs have proved popular due to their portability and reduced number of required Balance-Of-Plant (BOP) components; no compressors, supply or return manifolds, no cooling system components, such as pumps and radiators, and no humidifiers.

Despite the increasing popularity of open-cathode PEMFCs in low to medium power applications, they have not received much attention in the fuel cell systems literature. Furthermore, due to the low-cost nature of open-cathode fuel cell applications, they are usually equipped with simple open-loop controllers that, in turn, result in reduced overall system efficiency. However, by implementing advanced control algorithms, increased durability, safe operation, and optimal performance can be achieved. Therefore, Paper III in this dissertation provides a framework for the system-level understanding of performance and practical implementation of open-cathode fuel cells. More specifically, the performance characterization and modeling required for control design are studied in this paper. The effects of various phenomena including temperature, humidity, and hydrogen and air supply systems are analyzed by combining

past research with experimental investigations. Then, a set of nonlinear control-oriented models are developed for the entire open-cathode fuel cell system. The models are taken such that they capture important dynamics of individual system components, as well as their interactions. Furthermore, applicability to practical control design and ease of identification are other factors considered in the model development. All of the developed models are identified and validated experimentally.

Paper IV in the dissertation is built upon the foundation provided in Paper III. In this paper, temperature and voltage control, two of the important control problems in open-cathode fuel cells, are investigated. Temperature has an important effect on fuel cell performance. Higher operating temperatures result in an increased fuel cell output voltage, larger voltage variations during purging, and even cathode catalyst layer drying in the case of extreme temperatures [7]. Therefore, a controller capable of dynamically maintaining the desired temperature, while considering model and process uncertainties, is required in order to ensure the fuel cell's desired performance. Temperature control in open-cathode fuel cells is typically handled in an open-loop fashion by running the fans continuously at a constant speed [8], which induces undesirable auxiliary power consumption. At lower current demands where increased temperature is actually desirable, the fans can operate at lower speeds, thereby minimizing power consumption. However, a non-zero minimum fan speed is essential in order to guarantee the minimum air flow required to prevent oxygen starvation. In spite of the aforementioned advantages of operating open-cathode fuel cells at constant temperatures, a gradual voltage decrease over time is observed during this mode of operation. This phenomenon, along with the strong dependence of the fuel cell voltage on operating conditions, causes large voltage

uncertainties for any given current draw; thereby increasing the complexity and cost of the required power electronics circuitry. In this paper, a novel observer is augmented to a feedback temperature controller. The observer is capable of simultaneously estimating both the internal fuel cell temperature and the output voltage uncertainties. The observer stability is proved using Lyapunov stability and its effectiveness, as part of the control scheme, is shown experimentally. The proposed observer/controller set is robust against model uncertainties and ensures a fixed and predictable output fuel cell voltage as the operating conditions change. This feature can greatly simplify the design of open-cathode fuel cell systems and the power electronics to which they interface.

REFERENCES

- [1] M.S. Whittingham, “Electrical energy storage and intercalation chemistry,” *Science*, vol. 192, pp. 1126–1127, 1976.
- [2] K. Oates, *Lithium-ion batteries: commercialization history and current history*; Foresight Science & Technology: Providence, RI, USA, 2010.
- [3] J.B. Goodenough and K.-S. Park, “The Li-ion rechargeable battery: A perspective,” *Journal of the American Chemical Society*, vol. 135, pp. 1167–1176, 2013.
- [4] L. Tang, N. Lotfi, J. Ishaku, and R.G. Landers, Dynamic modeling and control of PEM fuel cell systems, in: S.E. Grasman, *Hydrogen energy and vehicle systems*, CRC Press, 2012, pp. 79–122.
- [5] E. Leksono, J. Pradipta, and T.A. Tamba, “Modeling and identification of oxygen excess ratio of self-humidified PEM fuel cell system,” *Mechatronics, Electrical Power, and Vehicular Technology*, vol. 03, pp. 39–48, 2012.
- [6] S. Strahl, A. Husar, and J. Riera, “Experimental study of hydrogen purge effects on performance and efficiency of an open-cathode proton exchange membrane fuel cell system,” *Journal of Power Sources*, vol. 248, pp. 474–482, 2014.
- [7] S. Strahl, A. Husar, and A.A. Franco, “Electrode structure effects on the performance of open-cathode proton exchange membrane fuel cells: A multiscale modeling approach,” *International Journal of Hydrogen Energy*, vol. 39, pp. 9752–9767, 2014.
- [8] M. Matian, A. Marquis, and N. Brandon, “Model based design and test of cooling plates for an air-cooled polymer electrolyte fuel cell stack,” *International Journal of Hydrogen Energy*, vol. 36, pp. 6051–6066, 2011.

PAPER

I. DEVELOPMENT OF AN EXPERIMENTAL TESTBED FOR RESEARCH IN LITHIUM-ION BATTERY MANAGEMENT SYSTEMS

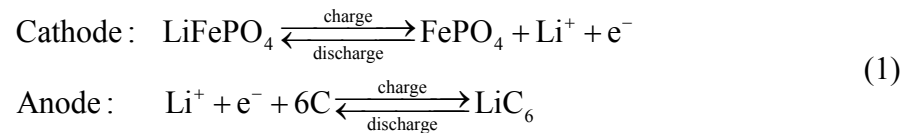
ABSTRACT

Advanced electrochemical batteries are becoming an integral part of a wide range of applications from household and commercial to smart grid, transportation, and aerospace applications. Among different battery technologies, lithium-ion (Li-ion) batteries are growing more and more popular due to their high energy density, high galvanic potential, low self-discharge, low weight, and the fact that they have almost no memory effect. However, one of the main obstacles facing the widespread commercialization of Li-ion batteries is the design of reliable battery management systems (BMSs). An efficient BMS ensures electrical safety during operation, while increasing battery lifetime, capacity and thermal stability. Despite the need for extensive research in this field, the majority of research conducted on Li-ion battery packs and BMS are proprietary works conducted by manufacturers. The available literature, however, provides either general descriptions or detailed analysis of individual components of the battery system, and ignores addressing details of the overall system development. This paper addresses the development of an experimental research testbed for studying Li-ion batteries and their BMS design. The testbed can be configured in a variety of cell and pack architectures, allowing for a wide range of BMS monitoring, diagnostics, and control technologies to be tested and analyzed. General considerations that should be taken into account while designing Li-ion battery systems are reviewed

and different technologies and challenges commonly encountered in Li-ion battery systems are investigated. This testbed facilitates future development of more practical and improved BMS technologies with the aim of increasing the safety, reliability, and efficiency of existing Li-ion battery systems. Experimental results of initial tests performed on the system are used to demonstrate some of the capabilities of the developed research testbed. To the authors' knowledge, this is the first work that addresses, at the same time, the practical battery system development issues along with the theoretical and technological challenges from cell to pack level.

1. INTRODUCTION

A battery is an energy storage device that can convert the chemical energy of its material into electrical energy. Lithium-ion (Li-ion) batteries were first introduced in 1976 [1], and subsequently commercialized in cell phones and laptops by the Sony Corporation in 1991 [2]. Li-ion batteries are usually composed of a carbon-made anode, a lithium ion conducting material electrolyte, and a cathode. There are a wide range of commercial cathode materials including LiCoO_2 and LiFePO_4 , each of which has its own advantages and disadvantages. The chemical reactions occurring in a LiFePO_4 battery during charge and discharge are



Li-ion batteries were first employed in consumer electronics; however, at the onset of 21st century, due to their advantages such as high energy density, low weight, low self-discharge and long life, they began to dominate energy storage in other fields as well. Other recent applications of Li-ion batteries include electric and hybrid electric vehicles, alternative energy systems such as wind and solar energy, and stationary energy storage. According to a recent study by [3], Li-ion batteries have been the dominant battery technology in electric and hybrid electric vehicles for over thirty years. They are projected to continue this dominance in transportation and other sectors. Figure 1.1 shows the distribution of different energy storage technologies in electric and hybrid electric vehicles.

In order to gain an insight about battery characteristics and investigate its performance, different tests need to be performed. These tests can be categorized as characterization, lifetime, reliability, and abuse tolerance tests [4]. Galvanostatic intermittent titration technique (GITT) [5], potentiostatic intermittent titration technique (PITT) [5], cyclic voltammetry (CV) [6], and impedance spectroscopy [6] are some of the commonly used characterization tests. Although these tests provide very useful detailed information about batteries, they typically address individual battery cell characteristics and require advanced and expensive test apparatuses. In order to overcome these issues, a number of tests have been devised to characterize battery cells and packs for transportation applications. A summary of the main international battery test standards is given in [4,7]. Although these tests are mainly designed for transportation applications, a majority of them, such as capacity and hybrid pulse power characterization (HPPC) tests [8], can be used for other Li-ion battery applications as well.

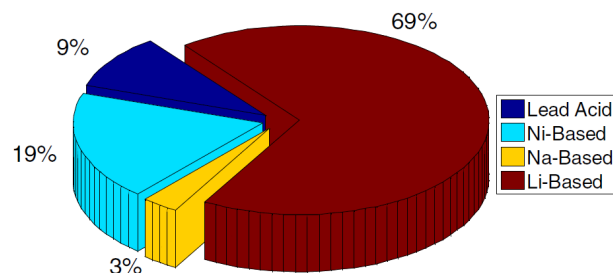


Figure 1.1. Distribution of different battery technologies in the transportation sector during the last 30 years [3].

Mathematical modeling is used for battery performance analysis and prediction, design optimization, and management system design. There are numerous works in the

literature on modeling Li-ion batteries. Doyle et al. [9] pioneered electrochemical battery modeling. These models predict the battery performance under different operating conditions and also provide insight into internal battery phenomena. Since Doyle et al.'s seminal work [9], different research groups have worked on model order reduction for these electrochemical models with the goal of easing the computational effort [10,11]. Although successful, the time-consuming parameter identification process is still a major drawback for these models. On the other hand, equivalent-circuit models, in spite of their limited prediction capability, have been employed extensively due to their efficient online implementation and low computational burden. One of the most commonly-used equivalent-circuit models is the improved Thevenin circuit model proposed by [12]. Furthermore, Hu et al. [13] introduced and compared 12 common battery models for online implementation. In addition to capturing battery dynamics sufficiently for different operating conditions, it is also very easy to identify equivalent-circuit model parameters. There are different methods to identify model parameters. Some of the aforementioned characterization tests such as HPPC can be used for this purpose.

One of the crucial components of a Li-ion battery is its battery management system (BMS). The most trivial task of a BMS is gathering and monitoring information about the battery operating conditions, namely, voltage, current, and temperature. For high voltage and current applications, multiple battery cells need to be connected together, in series and/or parallel, in order to meet the application requirements. In multiple battery configurations, balancing the battery cells is another responsibility of the BMS. More importantly, the BMS should be able to maintain a safe and reliable operation for the battery by controlling its operating voltage, current, and temperature.

Finally, based on the battery measurable signals, and typically a battery model, the BMS needs to be able to estimate unmeasurable battery states such as state of charge (SOC) and state of health (SOH). In summary, BMS functionalities include measurement and monitoring, cell balancing, thermal and electrical protection, and state estimation. These functionalities are discussed in more detail below.

Measurement is undoubtedly one of the most important responsibilities of a BMS. Accurate voltage, current and temperature measurements are needed from battery characterization tests to BMS design. There are strict requirements for the accuracy and resolution of voltage and current sensors for Li-ion BMSs. Lu et al. [14] reviewed some of voltage measurement methods currently implemented in BMSs.

Battery packs comprised of numerous cells require special attention from BMSs. Due to manufacturing variances, even matching battery cells have different internal characteristics. These differences cause the cells to charge and discharge at unequal rates. For that reason, the voltage across an entire series string of cells does not necessarily have a proportional voltage across each individual cell in that string. For example, a battery charger that only monitors the pack voltage will not fully charge certain cells and will subject other cells to overcharging. These issues can decrease the pack cycle life, cause a large loss in pack capacity over time, and result in safety hazards. To counteract these issues, a technique called cell balancing or charge equalization can be employed. This technique is implemented in a variety of ways; however, the concept for each method is similar. A balancing circuit maintains a uniform charge level among different cells by either dissipating excess energy from fully charged cells or by moving that excess energy to cells that are not fully charged.

Li-ion batteries have a typical operating temperature range of $-20\text{ }^{\circ}\text{C}$ to $55\text{ }^{\circ}\text{C}$ for discharge and $0\text{ }^{\circ}\text{C}$ to $45\text{ }^{\circ}\text{C}$ for charging [15]. Temperature distribution across a battery pack is affected by numerous factors such as environmental variations, the physical structure of the battery pack, and charge and discharge cycles. The physical structure of the battery pack can be optimized in the design stage to guarantee proper heat dissipation. At the design stage, high fidelity three-dimensional (3D) models [16] are usually employed to develop an optimal structure. On the other hand, the environment and the battery current profile act as disturbances to the temperature distribution inside the pack. Despite these factors, the temperature inside the battery pack, as well as individual cell temperatures, should be maintained in prescribed ranges in order to ensure safe and efficient battery operation. It is graphically demonstrated in [15] that temperatures that are too low and too high can result in safety hazards and/or battery performance degradation. Therefore, a proper thermal management system is of great importance. As mentioned earlier, the BMS is responsible for thermal management in Li-ion batteries to guarantee their safety, efficiency and prolonged life.

One of the most important BMS functionalities for Li-ion batteries is protection against operating beyond safe voltage and current limits. Battery manufacturers specify low and high voltage and current limits for each battery chemistry. As described in [17], violating these limits can have a wide range of undesirable effects from minor damage to the complete destruction of a battery to fire and explosion. Therefore, in order to increase the battery lifetime and ensure a safe and reliable operation, individual voltage and current values should be monitored constantly during its operation. As soon as any battery limit is approached, the BMS should take a corrective action in order to protect

the battery. The BMS reaction to any of these phenomena can be in the form of interrupting the current or limiting it to a safe value. Recently, researchers are trying to develop more advanced BMSs that are capable of determining less conservative current and voltage thresholds [11]. These works focus on electrochemical battery models in order to develop algorithms to extract maximum energy while ensuring a safe operation.

State estimation mainly involves SOC and SOH estimation. The estimation is needed because these states are not usually measurable. The definition of SOC is the ratio of available battery capacity to its fully charged capacity. State of Charge is an indication of how much longer the battery will be able to power the device. State of Health, on the other hand, does not have an agreed upon definition. It can be defined based on change of battery capacity, internal resistance, alternating current (AC) impedance, self-discharge rate, or power density [14]. However, SOH is mainly used to analyze battery status compared to a new battery. There is a vast body of literature on battery state estimation, especially SOC estimation. Lu et al. [14] provide a comprehensive overview of different SOC estimation algorithms including their advantages and disadvantages, application, and corresponding estimation error. It should, however, be noted that the majority of these methods are designed for a single battery cell rather than a pack, and issues regarding battery pack SOC and SOH estimation have not received much attention in the literature. The developed testbed will be employed to investigate different practical SOC and SOH estimation methods with a special focus on battery packs.

In this paper, the development of an experimental Li-ion research testbed is described. This testbed is intended to facilitate in-depth research on BMS design and implementation. Important considerations that need to be taken into account while

designing an advanced BMS are introduced; furthermore, various BMS subsystems are described. The experimental testbed provides three separate research platforms to test and study BMS technologies. The first platform focuses on cell level characterization, modeling, and protection system design. The second platform is specifically intended to address cell balancing by comparing currently available algorithms and developing optimal cell balancing strategies. The last research platform will address battery pack challenges and issues such as thermal management, individual and pack SOC estimation, and finally, protection system design for the entire battery pack. The test results will enable the development and improvement of novel BMS technologies with the goal of achieving safe, reliable, and efficient Li-ion battery systems. Some of the capabilities of the research testbed are illustrated through experimental results. The main contribution of this work is its focus on studying the technologies and challenges of entire Li-ion battery systems. These challenges are introduced during the description of the experimental testbed development. This paper not only addresses technical problems regarding Li-ion batteries and BMSs, it also sheds light on practical considerations in battery system development. To the authors' knowledge, this paper is the first work that addresses practical system development in parallel with theoretical and technological challenges in this field from cell to pack level.

2. EXPERIMENTAL LI-ION BATTERY RESEARCH TESTBED

In this section, some of the general design considerations during battery system development are discussed. These considerations include the requirements for protection circuitry, sensors, processing and data acquisition system, and BMS complexity. Furthermore, individual system components that are chosen based on these considerations are introduced and discussed.

Protection circuitry includes all the circuits and devices that are used to protect the battery from undesirable scenarios such as over/under voltage, current, and temperature. A typical response to such a scenario is current interruption. Current interruption is usually achieved by using fuses and relays or contactors. Fuses are used to autonomously interrupt the current once it maintains a certain level for a certain amount of time. The most important parameters in choosing a fuse for a specific battery application are the voltage rating, current rating and opening time. The relationship between the opening time and current is usually provided by the manufacturer in the form of a graph. Relays or contactors are other means of interrupting the current by an external command. Contact voltage and current ratings and coil voltage and current ratings are among the important parameters to consider when selecting a relay. The majority of high power relays and contactors require a drive or an amplifier in order to open/close using digital output signals. Another form of protection can be achieved by limiting the battery current to a set value. Current limiting is usually performed by commanding the battery load controller to facilitate drawing a lower current.

Accurate, reliable, and cost-effective sensing is undoubtedly one of the most important requirements of any battery system. In addition to being used in signal

monitoring, voltage, current, and temperature measurements in batteries are used in battery protection, cell balancing, and state estimation. In addition to the sensor's sensitivity and accuracy, its robustness to changes in the ambient conditions is also very important. Considering the great importance of voltage measurement in different BMS functionalities, a voltage measurement technique with a precision of approximately a few millivolts is desirable for most applications [14]. Furthermore, in bigger battery packs, a large number of battery cells necessitate the use of numerous voltage sensors, which in turn induces noise susceptibility and common mode rejection issues. Li [18] summarized different voltage measurement technologies. Current measurement, on the other hand, is mainly performed in three ways, namely, shunts with and without galvanic isolation, open-loop Hall effect sensors, and closed-loop Hall effect sensors. In addition to the aforementioned factors, there are many application-specific factors such as linearity, hysteresis, current range, output signal range, gain stability with respect to temperature variations, etc., which affect the choice of current sensors [19]. As the number of current sensors required in a typical battery system is considerably smaller than the number of voltage sensors, there are less strict cost limitations on selecting current sensors. There are not many studies on the choice of temperature sensors for Li-ion battery systems. Temperature measurements are typically used for monitoring and protection of individual cells and/or the entire pack. Therefore, sensor sensitivity and range are among the most important factors when selecting a temperature sensor for battery systems. It is worth mentioning that there is not a best choice in selecting the sensors for Li-ion battery systems. Sensor selection should be done based on BMS requirements, system scale, and

cost considerations. In summary, sensitivity, output type and level, and robustness are the most important criteria when selecting sensors for Li-ion batteries.

In large scale Li-ion battery systems, electronic control units (ECUs) or microcontrollers may be used for data acquisition, processing, storage, and communication with sensors and also outside systems. Restrictions on data acquisition and processing include sampling rate and resolution, clock frequency and processing power. The data storage capacity depends primarily on the BMS architecture and system requirements. For example, advanced BMS technologies that use electrochemical models for battery management require an extensive amount of storage memory. As mentioned earlier, the BMS needs to communicate with lower-level sensors to acquire the measurements and also coordinate with higher-level outside systems. The main communication protocol used in Li-ion BMSs is controller area network (CAN). This protocol, which was originally introduced in 1986 by Bosch for the automotive industry [20], has recently gained widespread acceptance in a large number of applications.

While the specific methods may be different for different battery chemistries [21], some of the BMS functionalities such as protection, cell balancing, and state estimation are common to different Li-ion battery systems. However, as mentioned earlier, one of the main obstacles facing Li-ion batteries is their cost. Depending on the cost limitations and system requirements, some other tasks might be required from BMSs, or some of the aforementioned functionalities might be performed using more advanced techniques. Active cell balancing and thermal management versus passive methods and advanced SOC and SOH estimation algorithms versus traditional algorithms are some of the BMS responsibilities that are usually more costly. These methods require large processing

power and storage capabilities. They might also need more expensive equipment during implementation.

The battery cells chosen for the experimental testbed presented in this paper are 20 Ah, LiMnPO₄ prismatic cells manufactured by GBS (Zhejiang, China). These prismatic cells offer high energy density, safety, and improved cycle life. They are also easier to assemble in battery packs compared to pouch cells. Some of the important specifications of the LiMnPO₄ battery cells, provided by the manufacturer, are summarized in Table 2.1.

Table 2.1. LiMnPO₄ battery cell specification [22].

Specification	Value	Unit
Nominal capacity	20	Ah
Single cell charging voltage limit	3.8	V
Single cell discharging voltage limit	2.5	V
Maximum continuous discharge current	3C	A
Maximum impulse discharge current	10C	A
Maximum charging current	3C	A
Standard charging current	0.3C–0.8C	A
Best charging current	0.5C	A
Single cell cycle life at 80% depth of discharge (DOD)	≥1500	times
Charging temperature	>0	°C
Discharging temperature	–20 to 65	°C
Self-discharge rate	≤3	%
Energy density	85–100	Wh/kg
Power density	>800	W/kg

Two types of controllers (processors) are implemented in the experimental system. The first unit is a PXI chassis from National Instruments (Austin, TX, USA). An NI-PXI-6229 multifunction card with 32 analog input channels with 16 bit resolution and

a 250 kS/s sampling rate, four analog output channels with 16 bit resolution and a 833 kS/s update rate, and 48 digital I/O channels is utilized inside the PXI chassis. National Instrument's LabVIEW is used as the computer interface. The reason for the inclusion of this controller is its reliability, high resolution for accurate measurements, high processing power for computationally challenging algorithms and data storage capacity for lengthy Li-ion characterization tests. In addition to the PXI chassis, an Arduino Mega microcontroller (SmartProjects, Strambiro, Italy), which is a board based on the ATmega1280, is also utilized. The Arduino has 16 analog inputs with 10 bit resolution that can be sampled at 10 kS/s and 54 digital I/O (14 of which can be used as PWM outputs). Despite the lower computational and storage capabilities of the Arduino Mega microcontroller, as compared to the NI system, it is very suitable for on-board and real-time applications due to its low cost. Considering BMS cost requirements, microcontrollers would be the ideal choice for most of the cases. Therefore, the Arduino microcontroller is included in the experimental system to facilitate research on the real world computational, storage, and communication issues facing BMS applications. It should be noted that PXI Chassis and Arduino microcontroller will be used individually, in order to handle BMS implementation from research and real-world points of view, respectively.

The voltage sensor used for individual cell and pack voltage measurements is a Phidgets precision voltage sensor (Phidgets Inc., Calgary, AB, Canada). It provides voltage measurements in the range of -30 V to 30 V with $\pm 0.7\%$ typical measurement error. The sensor output is a voltage between 0 V and 5 V . Two types of current sensors are used in the experimental testbed. The first type, which is based on an ACS714 Hall

effect-based linear current sensor from Allegro (Allegro MicroSystems, LLC, Worcester, MA, USA), is able to measure bidirectional DC currents up to 30 A with a sensitivity of 66 mV/A. It will be used to monitor current flows in cell balancing circuitry. The other current sensor which is used for the pack current measurements is based on Allegro's ACS758 Hall effect-based current sensor IC. It is capable of measuring bidirectional currents up to 100 A with a sensitivity of 20 mV/A. Finally, temperature measurements across the battery cells and pack are acquired using LM35 precision centigrade temperature sensors from Texas Instruments (Dallas, TX, USA). They have a linear scale factor of 10 mV/°C and are rated for -55 °C to 150 °C.

The desired maximum current for the overall system is 100 A. Therefore, the protection circuitry which comprises of a fuse and a contactor is chosen accordingly. The selected fuse is a 40 A bolt-down fuse from Littelfuse (Chicago, IL, USA) which is rated for 32 VDC and interrupting current of 2000 A at 32 VDC. Figure 2.1 shows the opening time versus current value for a family of this fuse. As can be seen from this figure, it takes about 5 s at a current value of 100 A for the fuse to open.

The protection unit has a 600 VDC, 100 A hermetically sealed DC contactor. Its coil is rated for 9–32 VDC and a maximum pickup current of 1–5 A at 20 °C. A MOSFET amplifier is designed in order to drive the contactor with the digital output from the controller.

Finally, a programmable power supply and electronic DC load pair from BK Precision (Yorba Linda, CA, USA) is used in order to charge and discharge the battery. The programmable power supply (model number XILN6024) is capable of delivering 1.44 kW power in constant current and voltage modes. The model 8514 programmable

DC load can absorb a maximum power of 1.2 kW in constant current, voltage, resistor, and power modes. Communication with the DC load and power supply is established through serial ports using NI LabVIEW.

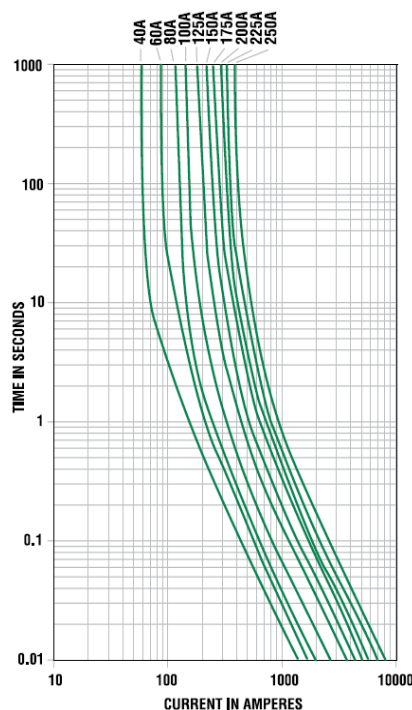


Figure 2.1. Characteristic curve for a 32 V rated Mega fuses from Littlefuse.

The experimental Li-ion research testbed is designed to operate in three configurations in order to cover a wide variety of research areas in Li-ion battery systems. The first configuration is a single cell research platform. The focus of this platform, which is shown in Figure 2.2, is to perform different tests on individual battery cells. These tests target electrical and thermal characterization and modeling of the individual cells and the analysis of discrepancies between seemingly identical cells. Efficient thermal and electrical protection unit architectures can also be studied. Finally,

high power performance and modeling analysis for battery cells can be addressed using this platform.

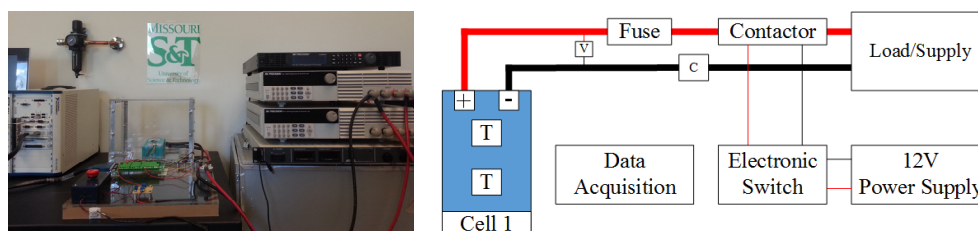


Figure 2.2. Single cell research platform with its schematic diagram.

The second platform addresses cell balancing during battery operation. Cell balancing is undoubtedly the most significant during charging as any imbalance among cells can result in overvoltage and, therefore, safety hazards. In order to study this important functionality, the second platform consists of three battery cells in series with each other. In addition to individual voltage sensors for cells, they are also equipped with individual current sensors to facilitate examining their current and, therefore, capacity evolution during different cell balancing strategies. This configuration is depicted in Figure 2.3.

The last platform is a complete eight cell battery pack with voltage and temperature sensors for each cell and a pack current and voltage sensor. This platform is devised to address issues encountered in battery packs such as battery pack modeling and state estimation, temperature distribution and thermal management, a cell balancing strategy addressing both charging and discharging, and efficient electrical protection of the battery packs. Figure 2.4 shows the battery pack setup with its corresponding schematic diagram.

In the following sections, different BMS functionalities are discussed in more detail. Considerations that should be taken into account in designing each subsystem and future improvements that can be integrated in BMS technologies are introduced. Some initial characterization test results are also reported.

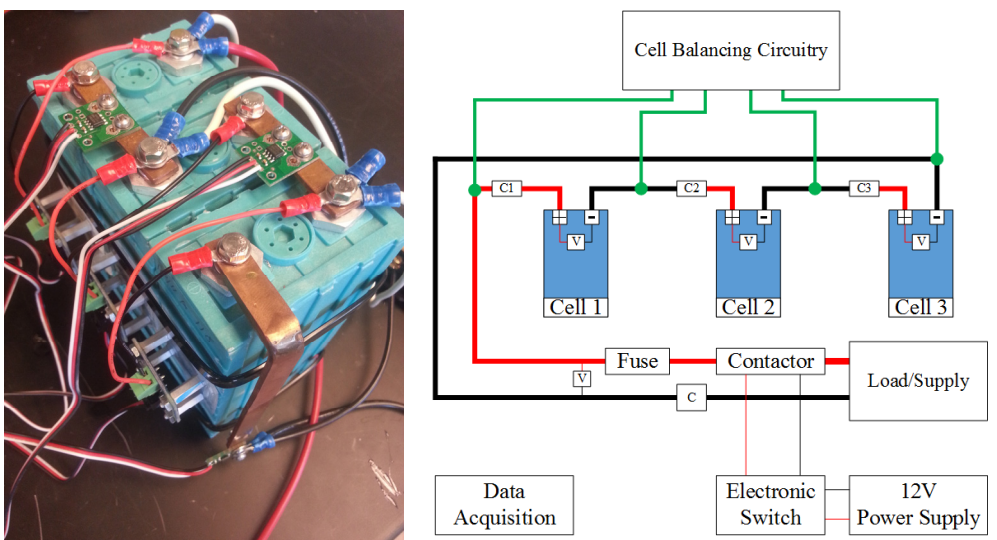


Figure 2.3. Cell balancing research platform with its schematic diagram.

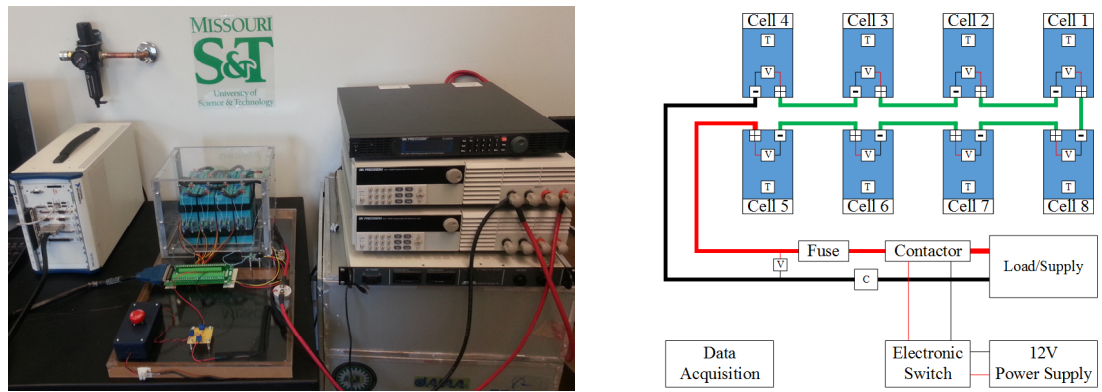


Figure 2.4. Battery pack research platform with its schematic diagram.

3. EXPERIMENTAL BATTERY CHARACTERIZATION AND MODELING

Battery characterization, for both cells and packs, is the initial stage in any battery system development. It aims to validate the battery parameters given in the manufacturer datasheet and identify those not provided by the manufacturer. Furthermore, it provides additional information that might be required by the BMS. This additional information includes electrochemical battery parameters, charge and discharge capabilities, temperature distribution, etc. Some of the battery characterization procedures such as GITT, PITT, impedance spectroscopy, and CV provide internal information about battery performance and structure. These tests require advanced testing equipment and are usually conducted by electrochemists. On the other hand, characterization tests such as the ones proposed by the Partnership for a New Generation of Vehicles or FreedomCAR [8] mainly deal with external battery performance. These tests typically make use of voltage, current, and temperature sensor measurements. Both types of characterization tests can provide the means of identifying different battery model parameters. An overview of different battery models and their applications will follow the characterization subsection. Temperature distribution along the cells and the pack and also the temperature effect on battery performance is not included in this paper and will be studied in the future work.

3.1. CHARACTERIZATION

The characterization tests that will be run on individual battery cells are chosen among the enhanced tests proposed in [4]. It should, however, be noted that charge and discharge current magnitudes for these tests are modified due to limitations on the power supply and electronic load ratings. These tests cover the majority of general

characterization experiments required for battery system development. The characterization tests are initialized with a charge/discharge cycle of 0.5C, which corresponds to 10 A. Figures 3.1 and 3.2 show the evolution of battery signals during this charge/discharge, respectively.

Battery charging is performed in constant current constant voltage (CCCV) regime. This is a common battery charging scenario in which a constant current is applied to the battery until its voltage reaches a specified upper limit (in this case 3.8 V). At this voltage limit, the battery will be kept at a constant voltage until its current decays to zero. Charge and discharge profiles are terminated according to upper/lower voltage limits prescribed by the manufacturer. As can be seen in Figures 3.1 and 3.2, despite the fact that the cells have a 20 Ah capacity, this nominal capacity cannot be achieved during charge/discharge. The reason for this can be attributed to either inaccurate upper/lower voltage limits in the protection subsystem or incorrect battery nominal capacity. These results magnify the need for characterization tests before any battery system development. Determination of exact battery capacity will be studied in the next subsection. On the other hand, choosing appropriate protection limits for the battery is discussed in the protection system subsection. The rest of the characterization tests are described below.

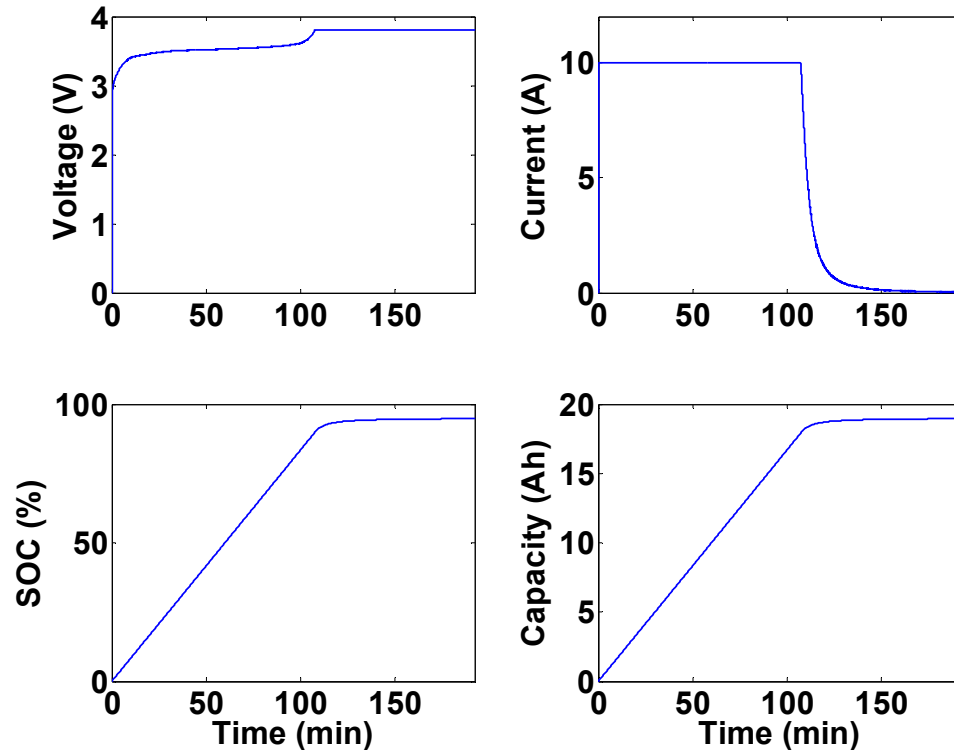


Figure 3.1. Battery charge profile.

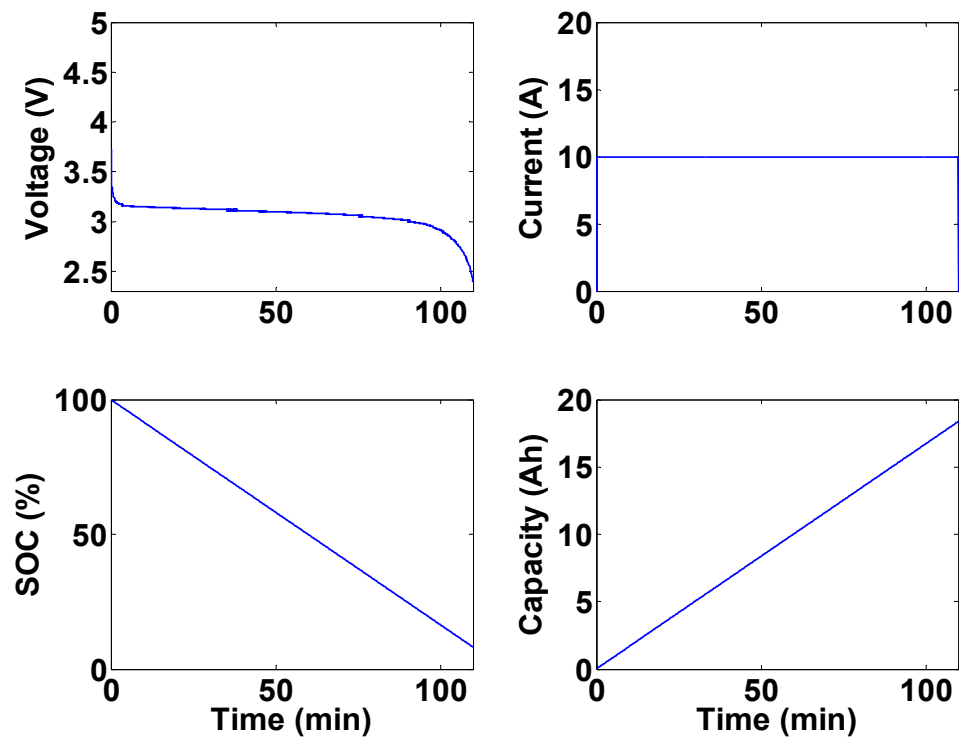


Figure 3.2. Battery discharge profile.

3.1.1. Static Capacity Test. The static capacity test is performed at three discharge rates of 0.5C, 1C, and 2C. Charging, on the other hand, is performed at rates of 0.5C, 1C, and 1C. Charging rate is always kept below or equal to 1C in order to ensure safe charging. After each (dis)charge, the cell is allowed to rest for approximately half an hour. Figures 3.3 and 3.4 illustrate battery voltage, current, SOC, and capacity evolution during these three discharge tests.

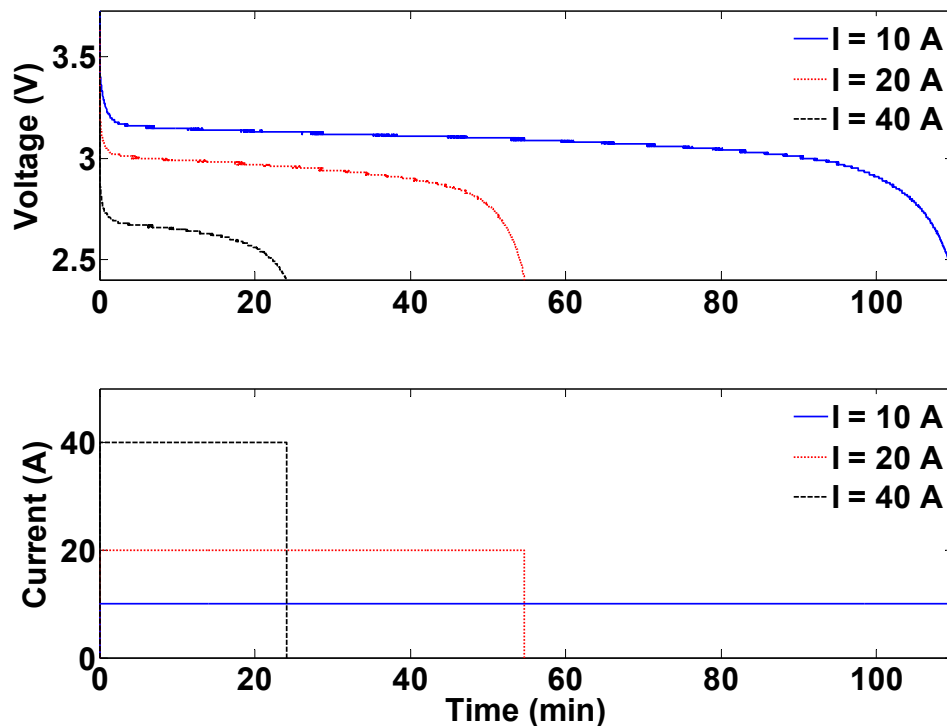


Figure 3.3. Voltage and current evolution during discharge tests for static capacity determination.

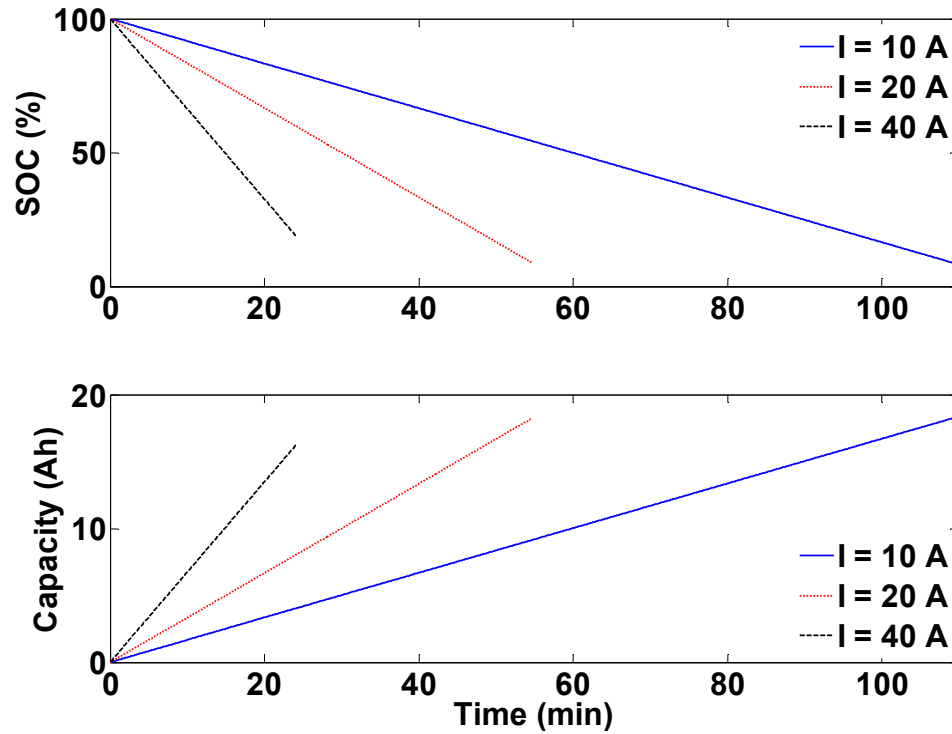


Figure 3.4. State of charge (SOC) and capacity evolution during discharge tests for static capacity determination.

It can be seen from Figures 3.3 and 3.4 that battery capacity is dependent on discharge current rate. The same holds true for charging current. Table 3.1 includes battery capacity values for different charge and discharge current rates.

Table 3.1. Battery capacity values.

Current (A)	Battery capacity (Ah)	
	Discharge	Charge
10	18.35	18.67
20	18.23	18.95
40	16.21	-

Battery capacity tests are not performed with 40 A charging current and that is the reason, the corresponding capacity is not reported in Table 3.1. Battery capacity change due to its current rate is usually characterized by Peukert's Law, which is an empirical relationship [23]

$$\Delta C = (I_t)^\gamma t \quad (2)$$

where ΔC is the battery capacity change (Ah); I_t is battery terminal current (A); γ is the Peukert constant, which is usually between 1.05 and 1.3; and t is the corresponding charge/discharge time (h). Battery capacity change due to its current rate is usually ignored in BMS design which might introduce errors. This effect will be considered in the BMS design for the experimental testbed.

3.1.2. HPPC Test. The HPPC test is a commonly used test profile, comprising charge and discharge pulses, that is used to determine the battery's dynamic power capabilities during its operation. Its main objective is to determine, according to some pre-defined requirements, the maximum and minimum battery voltage levels, as a function of depth of discharge (DOD), after charge and discharge pulses, respectively. These requirements are usually based on goals established for the FreedomCAR energy storage development program by the Idaho National Engineering and Environmental Laboratory (INEEL, Idaho Falls, ID, USA) [8]. The HPPC test can also be used to derive battery equivalent-circuit model parameters. These parameters are used in simulating battery behavior as well as determining battery status in its life cycle tests. The HPPC test profile is shown in Figure 3.5.

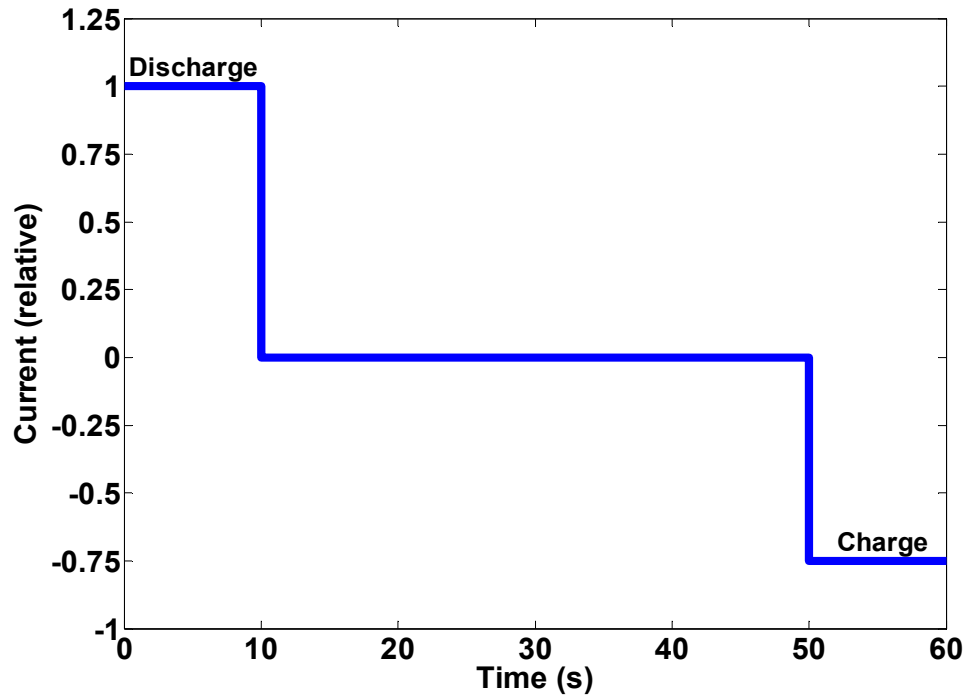


Figure 3.5. Hybrid pulse power characterization (HPPC) test profile [8].

The current values shown in Figure 3.5 are relative and their actual values are determined based on the rated maximum current scaled to two different values: in the low current HPPC test, the pulse discharge current is 25% of the absolute maximum pulse discharge current specified by the manufacturer for 10 s. However, if the manufacturer does not specify the maximum pulse current, the maximum pulse current will be taken as the 5C rate. In the high current HPPC test, the pulse discharge current is taken as 75% of the maximum pulse current. As mentioned earlier, due to power supply and electronic load constraints in the experimental system, the current values for the HPPC experiments are taken as: 20 A continuous discharge current, 40 A pulse discharge current, 16 A continuous charge current, and 20 A pulse charge current.

Overall, the HPPC procedure is comprised of nine repetitions of the profile shown in Figure 3.5, separated by a 10% DOD constant current discharges at a 1C rate. The

constant current discharge is followed by an hour rest period. The rest period is intended to let the battery reach thermal and electrochemical equilibrium. This procedure is continued until 90% DOD is achieved, after which another 1C rate discharge is performed until the battery reaches 100% DOD. Figure 3.6 shows a complete HPPC test sequence.

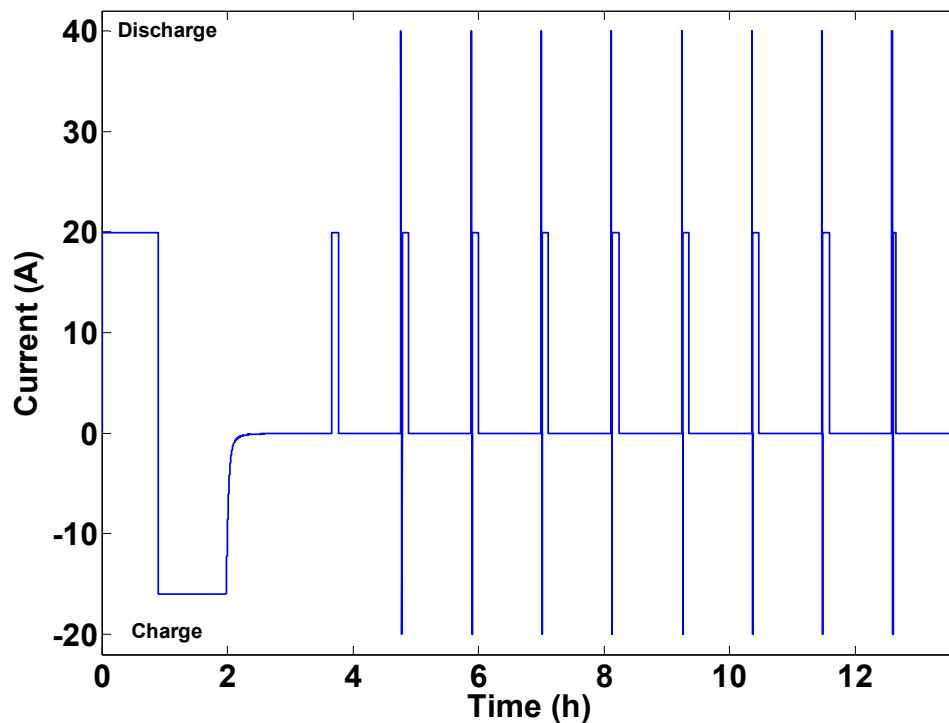


Figure 3.6. Complete HPPC test sequence.

The time evolution of battery voltage and SOC during the HPPC profile is shown in Figure 3.7.

The HPPC test on the experimental testbed is interrupted at 90% DOD in order to ensure battery safety. Analysis details of HPPC test results can be found in Section 4 of FreedomCAR Battery Test Manual for Power-Assist Hybrid Electric Vehicles [8].

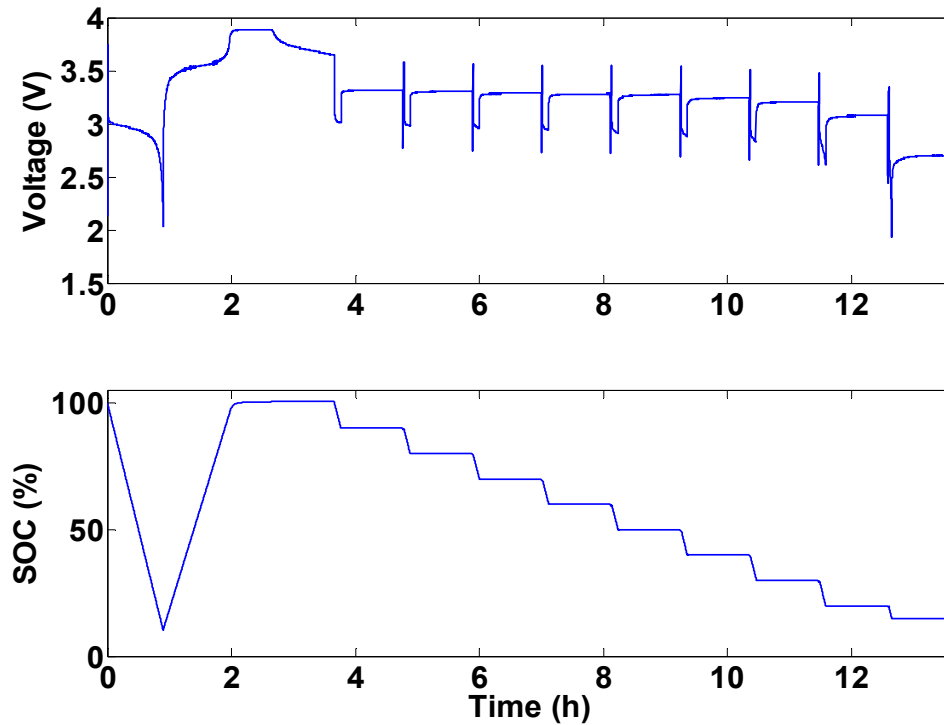


Figure 3.7. Battery voltage and SOC evolution during HPPC profile.

3.1.3. Open-Circuit Voltage Test. Open-circuit voltage tests are comprised of nine repetitions of constant current, fixed discharge intervals. As an example, starting with a fully charged battery, it is discharged with a current of $0.5C$ until it reaches 90% SOC. After a rest period of about half an hour, the battery is discharged again with the same current until it reaches 80% SOC. A similar rest period is then included. These discharge-rest sequences are repeated until the battery SOC reaches 10%. Figure 3.8 shows the first open-circuit voltage test that starts from SOC = 100%.

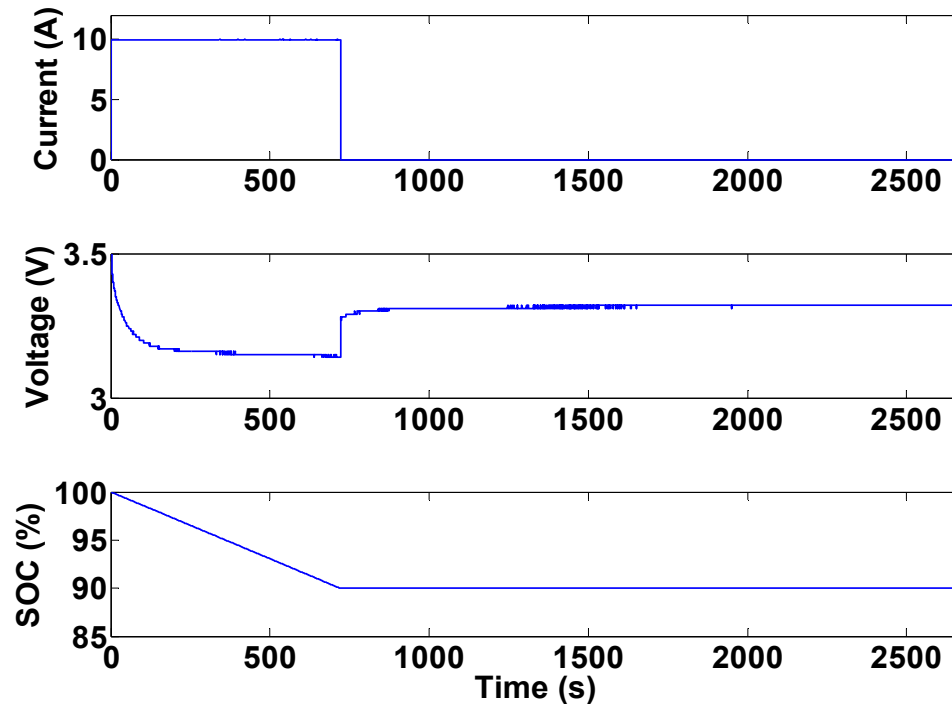


Figure 3.8. First step in open-circuit voltage tests.

Open-circuit voltage tests are mainly used to determine the exact relationship between battery SOC and open-circuit voltage. The rest periods in these tests are included in order to allow the battery terminal voltage to reach its equilibrium point so that it can be considered as the battery open-circuit voltage.

The test results can also be used to identify model parameters such as internal resistance and resistor-capacitor (RC) networks values [24]. Figure 3.9 demonstrates battery open-circuit voltage and internal resistance as a function SOC based on the results of open-circuit tests. The open-circuit voltage values are obtained from the steady-state battery voltage measurements. Battery internal resistance, on the other hand, can be calculated by dividing the voltage difference right before and after current interruption by

the current. In other words, if the voltage increase in Figure 3.8 at the instance of current interruption is ΔV , the internal resistance at SOC = 90% would be $\Delta V/10$.

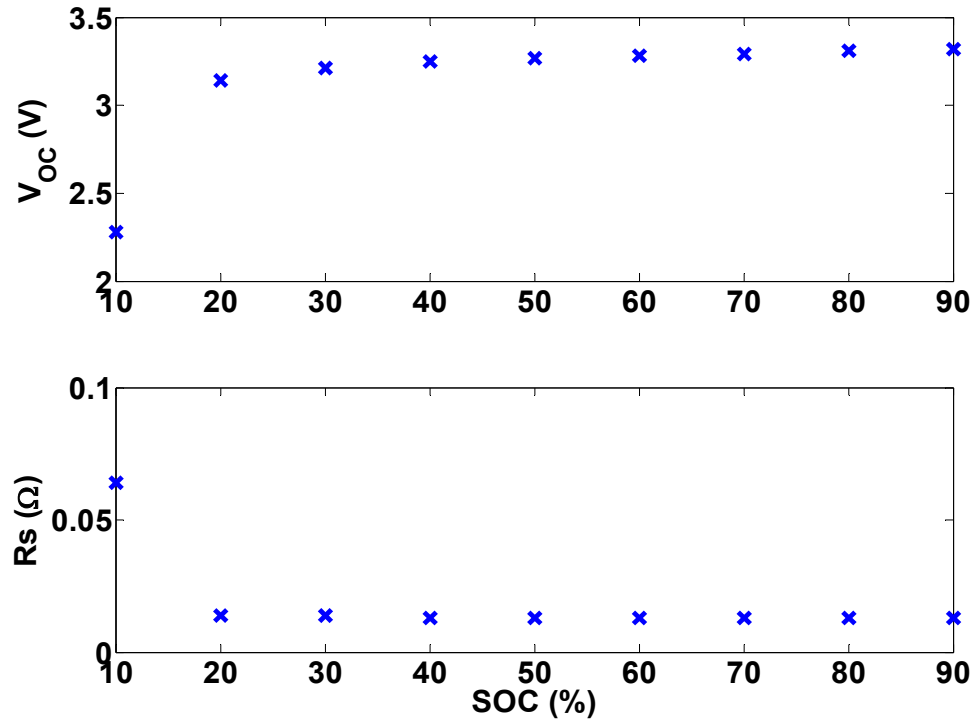


Figure 3.9. Battery open-circuit voltage and internal resistance versus SOC.

3.2. MODELING

There are numerous works in the literature on Li-ion battery modeling. The complexity and structure of the battery model greatly depend on the application requirements. High fidelity electrochemical models describing the performance of Li-ion batteries were first introduced by Doyle et al. [9]. These models have been used extensively for battery design and performance analysis. On the other hand, for real-time applications such as BMSs in which there are strict limitations on cost and processing power, equivalent-circuit models have been proposed. In these types of models, electrical circuit elements are used to describe the behavior of the Li-ion battery. Although these

models do not have a high prediction capability, they require very low computational power. Hence, they are widely used in model-based BMS applications. Hu et al. [13] presented an overview of twelve commonly used equivalent-circuit battery models. According to model complexity, accuracy and robustness, these twelve models have been evaluated. The authors concluded that first-order RC model with one-state hysteresis, proposed by [25], provides the best voltage prediction. The schematic of this model is shown in Figure 3.10.

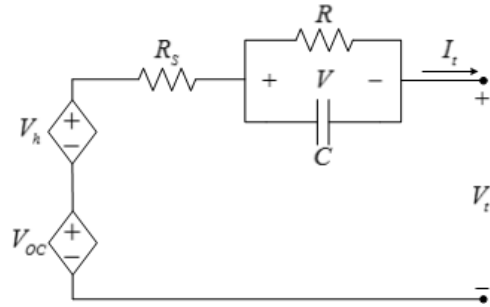


Figure 3.10. First-order resistor-capacitor (RC) model with one-state hysteresis [25].

Differential equations describing the dynamics of the model illustrated in Figure 3.10 are

$$\begin{cases} \frac{dz(t)}{dt} = -\frac{1}{3600C_{nom}} I_t(t) \\ \frac{dV(t)}{dt} = -\frac{1}{RC} V(t) + \frac{1}{C} I_t(t) \\ \frac{dV_h(t)}{dt} = -\beta(\eta_{I_t} - \varepsilon S_D) [V_{h,max} + \text{sign}(I_t) V_h] \end{cases} \quad (3)$$

where C_{nom} is the nominal battery capacity (F); and $z(t)$ is the SOC (%). The first equation in Eq. (3) is obtained from the definition of SOC, the second equation is from Kirchhoff's current law, and the last equation is proposed in [25] to take battery's hysteresis effects into consideration. In the last equation, the term SD denotes the battery self-discharge rate which is considered to be a function of temperature and battery SOC

$$S_D(t) = k_0 \exp\left(-\frac{E_{A,S}}{R_g T}\right) z(t) \quad (4)$$

where T is battery temperature (K); and the parameters β , η_{It} , ε , $V_{h,max}$, k_0 , $E_{A,S}$, and R_g are constants to be identified. The battery output voltage can also be written as

$$V_t = V_{OC}(t) - V_h(t) - R_s I_t(t) \quad (5)$$

One other commonly-used battery model is the equivalent-circuit model introduced in [12]. Figure 3.11 shows a schematic of this model. This model has been extensively used in various BMS subsystem designs including the SOC estimation subsystem [24,26].

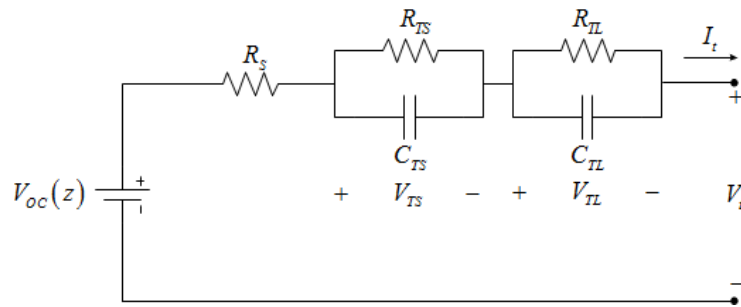


Figure 3.11. Equivalent circuit battery model [12].

Using the SOC definition and Kirchhoff's current law for the model in Figure 3.11, the set of first-order differential equations describing the battery dynamics is

$$\begin{cases} \frac{dz(t)}{dt} = -\frac{1}{3600C_{nom}} I_t(t) \\ \frac{dV_{TS}(t)}{dt} = -\frac{1}{R_{TS}C_{TS}} V_{TS}(t) + \frac{1}{C_{TS}} I_t(t) \\ \frac{dV_{TL}(t)}{dt} = -\frac{1}{R_{TL}C_{TL}} V_{TL}(t) + \frac{1}{C_{TL}} I_t(t) \end{cases} \quad (6)$$

Furthermore, using Kirchhoff's voltage law, the output battery voltage is

$$V_t = V_{OC}(z(t)) - V_{TS}(t) - V_{TL}(t) - R_s I_t(t) \quad (7)$$

These two models will be used in the BMS design for the experimental research testbed. Different algorithms have been proposed to identify the model parameters of the above models. A majority of the identification procedures employ HPPC data in order to identify the model parameters. Details of model identification process can be found in [13,24,27].

It is also worth mentioning that despite the high computational cost of electrochemical models, a number of research groups have focused their attention on employing these models in BMS design, due to the models' high accuracy and prediction capability. One of the first efforts in this area was described in Santhanagopalan *et al.* [28]. They introduced the single particle approximation of the full order electrochemical models and used it for SOC estimation. Domenico *et al.* [29] and Moura *et al.* [30] used this single particle model for SOC estimation. Smith *et al.* [10] and Chaturvedi *et al.* [11]

employed model order reduction techniques to facilitate on-line implementation of electrochemical models in BMSs.

4. CELL BALANCING

Cell balancing is a technique used to establish uniformity among cells in a battery pack. Internal differences among battery cells, despite similar specifications and type, are inevitable. The imbalance among battery cells can arise from differences in voltage, SOC, capacity, internal resistance, self-discharge and their change rate [14]. An efficient balancing algorithm can be employed by the BMS to make use of the available battery pack capacity. Lack of proper cell balancing might result in under/over voltage of some battery cells in the pack which, in turn, can have undesirable effects ranging from battery life degradation to safety hazards. Cell balancing can be performed based on the voltage and remaining capacity (SOC). Due to the immaturity of SOC estimation techniques for individual battery cells and battery packs, cell balancing based on voltage uniformity is more feasible and common.

Cell balancing techniques can be divided into passive and active. In passive cell balancing, the existing excess energy or capacity among cells is wasted in a passive circuit element such as a resistor. Passive cell balancing is easy to implement and does not introduce large costs. Active cell balancing, on the other hand, employs active circuit elements such as capacitors and switches to shuttle charge between the unbalanced cells. Although active cell balancing is more efficient, it introduces complexity, unreliability, and difficulty in implementation. Current active cell balancing techniques include switched capacitor, double-tiered switched capacitor, single-switched capacitor, step up/boost converter module, and multi-winding transformers [31–34]. Some of the most common cell balancing techniques with their corresponding advantages and drawbacks are summarized below.

4.1. RESISTIVE SHUNTING

This method of cell balancing, shown in Figure 4.1, is simple and effective. It is a passive method because it dissipates excess energy into heat. The system works by monitoring each cell's voltage and comparing them to one another. If a cell's voltage becomes higher than the voltages of other cells, a shunt resistor is connected across that cell using a transistor or a relay. The resistor turns the excess energy from that cell into heat until a balanced voltage is achieved among different cells.

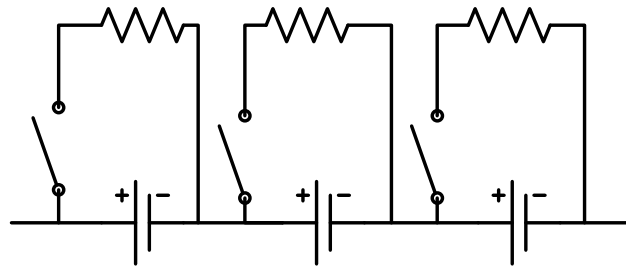


Figure 4.1. Resistive shunting configuration.

Resistive shunting is usually performed in two methods. In the first method, cell balancing is performed during the whole battery operation. As soon as a cell voltage deviates from other cells' voltage, the corresponding switch closes and transfers the excess charge to the resistors. The amount of energy wasted in resistors is very low due to small variances in cell voltages. However, this scenario introduces larger switching losses due to frequent switching. The second method initiates cell balancing at the end of charge cycle. In this case, once a cell reaches its maximum voltage, its corresponding switch closes and transfers the battery current to the resistor. High power resistors are

usually required for this method, as large current values can pass through the resistors. The second method is not applicable for cell balancing during discharge cycles.

4.2. SWITCHED CAPACITOR

Switched capacitor cell balancing works by shuttling charge from higher voltage cells to lower voltage cells. The circuit for a switched capacitor configuration is shown in Figure 4.2. The capacitors each switch between two cells. When connected to the higher voltage cell in the pair, the capacitor will be charged. On the other hand, when the capacitor switches to the lower voltage cell, it will discharge. This approach requires no intelligent control, only a clock cycle is needed to trigger the switching between cells.

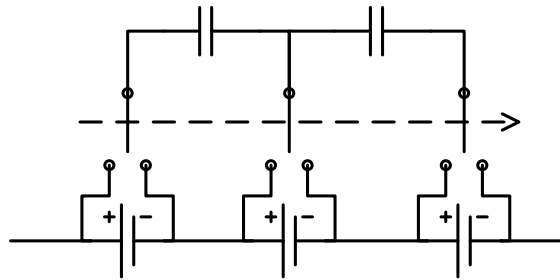


Figure 4.2. Switched capacitor configuration.

4.3. DOUBLE-TIERED SWITCHED CAPACITOR

This method is implemented in the same way as the switched capacitor method, but with an additional tier of capacitors as shown in Figure 4.3. The second tier of capacitors switches between two series pairs of cells. This greatly reduces the balancing time for the pack, especially if cells with different charge levels are located far apart from one another in the pack.

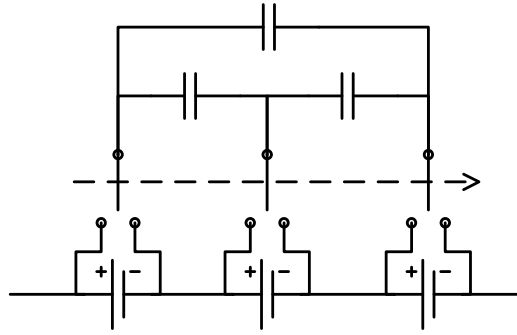


Figure 4.3. Double-tiered switched capacitor configuration.

4.4. SINGLE-SWITCHED CAPACITOR

The single switched capacitor configuration uses one capacitor and an array of switches, as illustrated in Figure 4.4. The cell voltages are monitored and used to intelligently control the connections to the capacitor. Rather than cycling through individual cells, the system chooses to cycle between two cells in the pack with the greatest voltage difference.

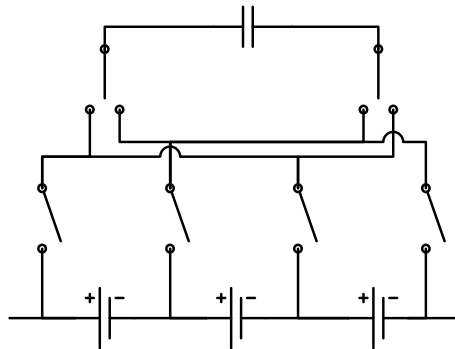


Figure 4.4. Single-switched capacitor configuration.

4.5. STEP-UP/BOOST CONVERTER

The step-up/boost converter balancing circuit is shown in Figure 4.5. The circuit is comprised of isolated converters for each cell in the series string. The inputs of the

converters are connected across each cell and the outputs from the converters are paralleled across the pack. The system monitors each cell's voltage and intelligently controls the converters to remove energy from higher voltage cells and redistribute it to the rest of the cells in the pack.

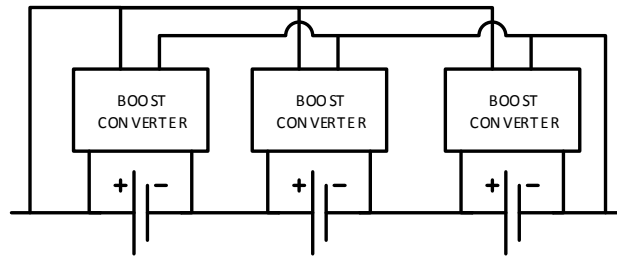


Figure 4.5. Boost converter configuration.

Comprehensive and in-depth comparisons between different balancing methods, discussed in this paper, are conducted in [35–37]. These studies consider cost and number of circuit components in their comparisons. There is not a single cell balancing method that is the best across all categories. Depending on the application requirements, any of these methods may be the appropriate choice. A tradeoff should be made between system cost and efficiency while designing cell balancing circuitry. An optimal switching schedule, considering system losses in order to increase the overall system efficiency, is one of the future studies to be conducted on this experimental Li-ion research testbed.

5. PROTECTION

The protection subsystem in the BMS is intended to guarantee the battery operates in its safe region. Battery voltage, current, and temperature are factors determining the safe operating region. Some of the harmful effects of running the battery outside of this region were briefly reviewed in the Introduction based on information from [15]. Two important aspects should be taken into account when designing a battery protection subsystem: when to react to a detected range violation and how to handle such a condition. In this section, these aspects will be studied for voltage, current, and temperature protection. Furthermore, the protection subsystem architecture devised for the experimental battery testbed is discussed.

The operating voltage of Li-ion batteries is dictated by their chemistry. More specifically, the material used in the cathode structure determines the battery voltage limits. For the battery chemistry used in the experimental testbed, which is described in Table 2.1, the operating voltage should be between 2.5 V and 3.8 V. Therefore, the BMS should ensure the individual cell voltages remain in this range at all times. It should be noted that it is more efficient to impose voltage limits on the battery open-circuit voltage rather than the battery terminal voltage. However, battery open-circuit voltage is not measurable during battery operation and an estimation algorithm should be implemented to obtain battery open-circuit voltage from its measurable signals, *i.e.*, voltage, current, and temperature. The easiest method to estimate battery open-circuit voltage is to use the equivalent-circuit model shown in Figure 5.1.

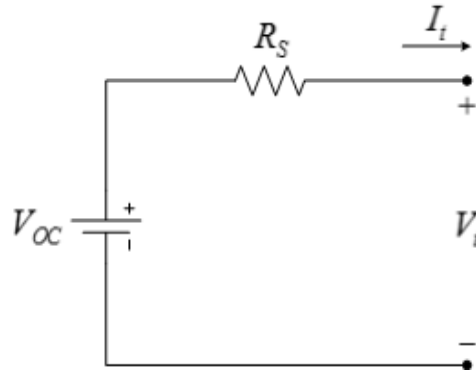


Figure 5.1. Equivalent-circuit battery model.

Applying Kirchhoff's voltage law to the circuit in Figure 5.1, the battery open-circuit voltage is

$$V_{OC} = V_t + R_S I_t \quad (8)$$

where R_S is calculated from open-circuit voltage tests, as described in Section 3.1.3. In order to estimate battery open-circuit voltage using Eq. (8), the average value of R_S , which is 0.0189Ω , is used.

Another method to obtain battery open-circuit voltage, assuming an accurate SOC estimate is available, is to use the open-circuit voltage-SOC relationship. This relationship can be obtained from fitting the following model to the experimental data in Section 3.1.3

$$V_{OC}(SOC) = 3.186 \cdot \exp(0.00047114 \cdot SOC) - 10.88 \cdot \exp(-0.2469 \cdot SOC) \quad (9)$$

Figure 5.2 shows the fitted model in Eq. (9) and the experimental results. It is proposed in [17] that the time average of the battery terminal voltage should be used as the protection criteria instead of the terminal voltage.

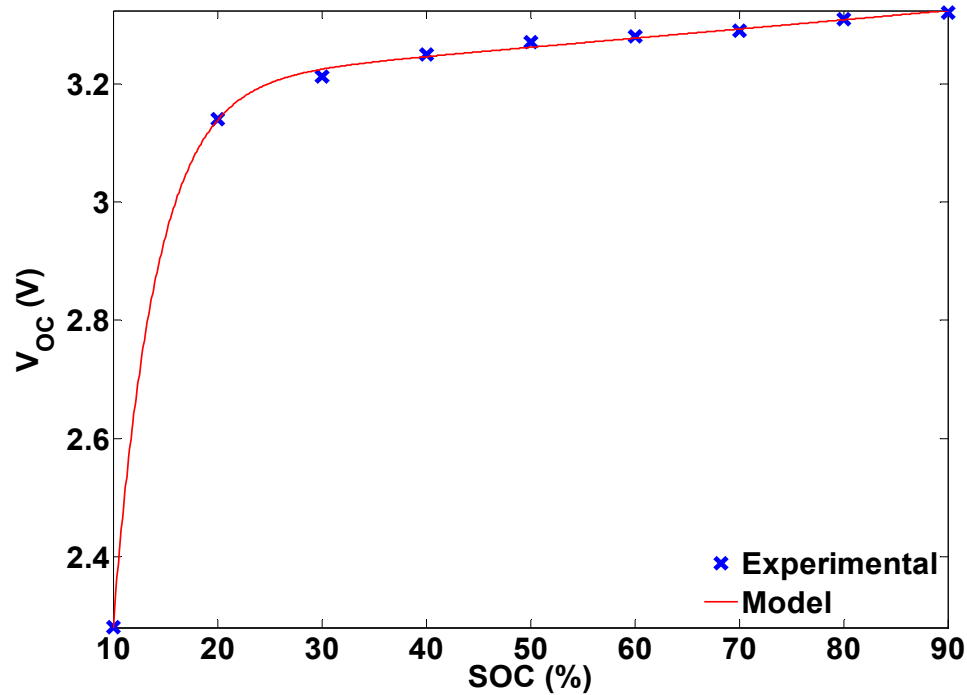


Figure 5.2. Experimental and modeled battery open-circuit voltage.

Figure 5.3 shows the evolution of terminal voltage, open-circuit voltage obtained using the above two methods, and the time average of terminal voltage during a complete battery discharge.

As can be seen from Figure 5.3, more energy can be extracted from the battery, before the manufacturer's low cut-off voltage is approached, if the open-circuit voltage obtained from Eq. (8) is used in the protection system. It should however, be noted that Eq. (8) is just an approximation of the open-circuit battery voltage. Substantial research is

still needed in designing less conservative and more efficient Li-ion battery protection systems. The results presented in Figure 5.3 are obtained from a constant-current discharge profile. Investigating the performance of protection system during dynamic current profiles is also an important research topic in BMS development.

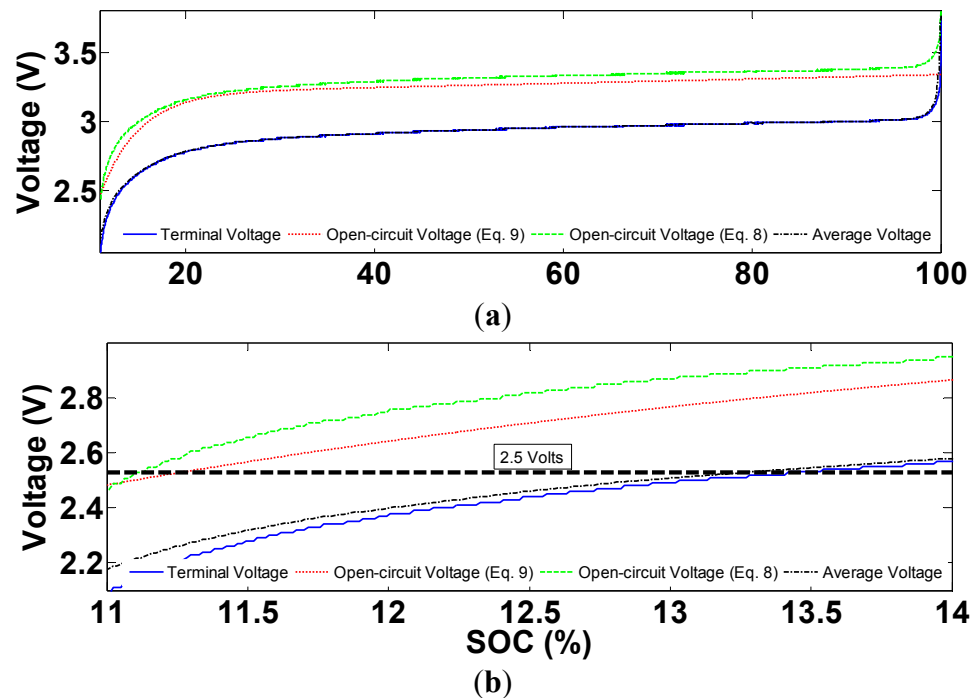


Figure 5.3. Comparison of different voltage levels during a discharge profile: (a) the whole profile; and (b) end of discharge.

Finally, there are some recent studies which focus on observing internal battery parameters such as lithium concentration in the negative electrode instead of battery voltage as the protection criteria [11,38]. The authors claim that by considering such protection criteria for batteries more energy can be extracted while maintaining safe battery operation. More research still needs to be conducted to facilitate on-line implementation of such algorithms.

Once a voltage limit is being approached, the battery's protection system will react to it in one of the following three ways: interrupt the current, ask an external system component to interrupt the current, or communicate with the load and command it to limit the current it is drawing from the battery.

The protection units, which will interrupt the current autonomously, are called protectors [17] but are not studied here. The other two reactions of the protection unit, however, are implemented in the experimental testbed. The choice of which reaction to choose depends on the application. Specifically, current limiting is usually preferred in applications where continuous current supply is vital.

The safe operating range for the battery current is usually determined by its physical structure and manufacturing specifications. As can be seen in Table 2.1, four current limits are specified for batteries in the datasheet: continuous charging, peak charging, continuous discharge, and peak discharge. As soon as the continuous battery charge/discharge current is exceeded, the protection unit needs to monitor the excess current duration and calculate the SOC variation in this period. It then only has to take action if the SOC reaches 0% or 100%. In this way, peak charge/discharge currents will also be tolerated for specific time periods. The protection unit reaction can be any of the scenarios described for voltage range violation. It should also be noted that in order to achieve the protection for both charge and discharge, the BMS needs to be able to differentiate between charge and discharge by assigning a current sign convention, e.g., positive for discharge and negative for charge.

The operating temperature range for Li-ion batteries which is usually between $-20\text{ }^{\circ}\text{C}$ and $55\text{ }^{\circ}\text{C}$ is very likely to be violated in applications such as transportation. In

order to circumvent the undesirable effects of temperature range violation, an efficient thermal management subsystem is required. The thermal management subsystem monitors cells and/or pack temperatures and maintains their temperatures within desired ranges. Depending on the BMS complexity and ambient battery temperature, the thermal management system might incorporate passive cooling, active air or liquid cooling, or refrigeration. Another important issue regarding the temperature of Li-ion batteries is a phenomenon called “thermal runaway.” Thermal runaway can occur due to ambient conditions, structural defects, or battery abuse. In any case, thermal runaway is usually not detectable by temperature sensor measurements as the internal temperature of li-ion battery cells is significantly higher than their casing temperature. This issue may be prevented by implementing an estimation algorithm capable of monitoring internal cell temperature. Thermal management system design and internal battery temperature estimation are among two future studies that will be conducted on the experimental testbed.

6. INDICATION OF BATTERY STATES

Li-ion battery states include the battery's operational conditions that affect the performance of the battery and also the systems connected to it. These states include SOC and SOH. SOC shows the amount of charge remaining in the battery compared to a full battery. In other words, it is an indication of the operation scope of the battery-powered device. From an electrochemical point of view, SOC is the ratio of the lithium ion concentration to the maximum lithium ion concentration in the negative electrode (limiting electrode). It is mathematically defined by

$$SOC(t) = \frac{SOC(t_0) \times Q_{nom} - \int_{t_0}^t I_t(\tau) d\tau}{Q_{nom}} \quad (10)$$

where Q_{nom} is the nominal capacity (Ah); $I_t(t)$ is the battery terminal current; t_0 is the initial time (s); and t is the elapsed time (s). Equation (10) cannot be used in practice to obtain SOC due to issues arising from measurement noise in I_t and also the unavailability of $SOC(t_0)$ in different applications. Therefore, since SOC is not measurable, an estimation algorithm is usually required to estimate the SOC using the battery's measurements, *i.e.*, current, voltage, and temperature. Although the majority of SOC estimation algorithms rely on a battery model to acquire SOC, some non-model based methods have also been proposed. Among these types of methods, a combination of battery current integration, using Eq. (10), and the voltage translation method is the most common one. The voltage translation method is based on the battery voltage versus SOC relationship and is typically used to calibrate the current integration method. Model-based

methods, on the other hand, employ either an electrochemical model or an equivalent-circuit model. As mentioned earlier, [10,11,28–30] are some of the works recently conducted on SOC estimation based on full-order or reduced-order electrochemical models. However, due to the aforementioned implementation simplicity of equivalent-circuit models, there is a large body of literature using equivalent-circuit models to estimate battery SOC. In these works, different battery models are used along with an estimation algorithm such as Extended Kalman Filter [26,39], sliding-mode observers [24,40], adaptive observers [41], and linear parameter varying (LPV) observers [42].

Battery SOH is an indication of battery status compared to a fresh battery. In other words, it captures battery cycle life and aging effects. There is not a universal definition for SOH and different battery parameters are considered as indications of SOH. Among these parameters, battery capacity and internal resistance are the most popular ones. Due to the arbitrary definition of SOH, different authors [40–43] have used different methods and criteria to obtain SOH. The majority of SOH estimation algorithms employ a parameter identification method such as Kalman filtering [44] or adaptive estimators [45] in order to obtain some battery parameters. In these studies, the changes in parameters such as internal resistance or battery capacity are considered to be the SOH.

At the initial stages of the experimental testbed development, battery state of charge is obtained using the combination of current integration and voltage translational methods, as explained earlier. Although this combination is one of the most-commonly used SOC indication algorithms, the sliding-mode observer introduced in [24] will be

used in the future due to this method's intrinsic robustness against model uncertainties. As mentioned earlier, the main focus of this testbed in the future will be to design SOC and SOH algorithms for battery packs. This research area is of utmost importance in real world applications; however, it has not received much attention in the literature.

7. SUMMARY AND CONCLUSIONS

In this paper, the development of an experimental Li-ion battery research testbed was presented. The main purpose of this testbed is to investigate current BMS technologies, determine their weaknesses and strengths, and identify future research paths to improve existing BMS methodologies. After a detailed description of design considerations and system development, battery characterization and modeling were studied, and some of the essential functionalities of BMSs were reviewed. These functionalities include: electrical and thermal protection, cell balancing, and battery state indication. The most commonly-used algorithms for each of these subsystems, along with their advantages and disadvantages, were introduced and open research areas in BMS design were reviewed. The need for further research is significant in areas such as thermal modeling, protection, optimal cell balancing, and SOC estimation. Specifically, battery packs require special attention as it is not very trivial to extend cell-level algorithms such as SOC estimation and protection system, to battery packs. In order to address these issues and challenges, the experimental testbed can be configured in three platforms, namely; single cell, cell balancing, and battery pack research platforms. Some initial experimental test results were presented to illustrate the capabilities of the testbed. Future work involves further tests on battery characterization and modeling and developing novel algorithms based on optimal control theory that can address cell balancing issues. Finally, as the main focus of future work, challenges in battery packs including protection and individual cell and pack SOC indication will be addressed. The ultimate goal of the testbed is to provide a platform to facilitate the improvement of

existing BMS technologies in order to have more efficient and reliable Li-ion battery systems.

REFERENCES

- [1] M.S. Whittingham, “Electrical energy storage and intercalation chemistry,” *Science*, vol. 192, pp. 1126–1127, 1976.
- [2] K. Oates, *Lithium-ion batteries: commercialization history and current history*; Foresight Science & Technology: Providence, RI, USA, 2010.
- [3] A.M. Bazzi, “Electric machines and energy storage technologies in EVs and HEVs for over a century,” *IEEE International Electric Machines and Drive Conference*, May 12–15, 2013, Chicago, IL, USA.
- [4] G. Mulder, N. Omar, S. Pauwels, F. Leemans, B. Verbrugge, W.D. Nijs, P.V.D. Bossche, D. Six, and J.V. Mierlo, “Enhanced test methods to characterize automotive battery cells,” *Journal of Power Sources*, vol. 196, pp. 10079–10087, 2011.
- [5] M. Jiang, B. Key, Y.S. Meng, and C.P. Grey, “Electrochemical and structural study of the layered, “Li-excess” lithium-ion battery electrode material $\text{Li}[\text{Li}_{1/9}\text{Ni}_{1/3}\text{Mn}_{5/9}]\text{O}_2$,” *Chemistry of Materials*, vol. 21, pp. 2733–2745, 2009.
- [6] R.P. O’Hayre, S.W. Cha, W. Colella, and F.B. Prinz, *Fuel Cell Fundamentals*, 1st ed.; John Wiley and Sons, Inc.: New York, NY, USA, 2009.
- [7] N. Omar, M. Daowd, O. Hegazy, G. Mulder, J.-M Timmermans, T. Coosemans, P.V.D Bossche, and J.V. Mierlo, “Standardization work for BEV and HEV applications: Critical appraisal of recent traction battery documents,” *Energies*, vol. 5, pp. 138–156, 2012.
- [8] U.S. Department of Energy Vehicle Technologies Program: Battery Test Manual for Power-Assist Hybrid Electric Vehicles; Idaho National Laboratory: Idaho Falls, ID, USA, 2008.
- [9] M. Doyle, T.F. Fuller, and J. Newman, “Modeling of galvanostatic charge and discharge of the lithium/polymer/insertion cell,” *Journal of the Electrochemical Society*, vol. 140, pp. 1526–1533, 1993.
- [10] K. Smith, and C.-Y. Wang, “Power and thermal characterization of a lithium-ion battery pack for hybrid-electric vehicles,” *Journal of Power Sources*, vol. 160, pp. 662–673, 2006.
- [11] N.A. Chaturvedi, R. Klein, J. Christensen, J. Ahmed, and A. Kojic, “Algorithms for advanced battery-management systems,” *IEEE Control Systems Magazine*, vol. 30, pp. 49–68, 2010.

- [12] M. Chen and G.A. Rincón-Mora, "Accurate electrical battery model capable of predicting runtime and I–V performance," *IEEE Transactions on Energy Conversion*, vol. 21, pp. 504–511, 2006.
- [13] X. Hu, S. Li, and H. Peng, "A comparative study of equivalent circuit models for Li-ion batteries," *Journal of Power Sources*, vol. 198, pp. 359–367, 2012.
- [14] L. Lu, X. Han, J. Li, J. Hua, and M. Ouyang, "A review on the key issues for lithium-ion battery management in electric vehicles," *Journal of Power Sources*, vol. 226, pp. 272–288, 2013.
- [15] Lithium Battery Failures. Available online: http://www.mpoweruk.com/lithium_failures.htm (accessed on 30 July 2013).
- [16] K. Yeow, H. Teng, M. Thelliez, and E. Tan, "Comparative study on thermal behavior of lithium-ion battery systems with indirect air cooling and indirect liquid cooling," *ASME/ISCIE International Symposium on Flexible Automation*, June 18–20, 2012, St. Louis, MO, USA.
- [17] D. Andrea, *Battery management systems for large lithium-ion batteries*, 1st ed.; Artech House: Boston, MA, USA, 2010.
- [18] L. Li, *Battery management system of lithium ion battery in pure EV*, Master's Thesis, Beijing Jiaotong University, Beijing, China, June 2009.
- [19] Raztec Sensors: Hall Effect Current Sensors and Current Transducers that Make Ideal Current Shunt and Current Transformer Replacements. Available online: <http://www.raztec.co.nz/> (accessed on 30 July 2013).
- [20] CAN in Automation (CiA): CAN History. Available online: <http://www.can-cia.de/index.php?id=161> (accessed on 30 July 2013).
- [21] N. Omar, M. Daowd, P.V.D. Bossche, O. Hegazy, J. Smekens, T. Coosemans, and J.V. Mierlo, "Rechargeable energy storage systems for plug-in hybrid electric vehicles—Assessment of electrical characteristics," *Energies*, vol. 5, pp. 2952–2988, 2012.
- [22] Electric Motorsport EV Parts. Available online: http://www.electricmotorsport.com/store/ems_ev_parts_batteries_lpf_gbs_20ah.php (accessed on 30 July 2013).
- [23] D. Doerffel and S.A. Sharkh, "A critical review of using the Peukert equation for determining the remaining capacity of lead-acid and lithium-ion batteries," *Journal of Power Sources*, vol. 155, pp. 395–400, 2006.

- [24] N. Lotfi and R.G. Landers, "Robust nonlinear observer for state of charge estimation of Li-ion batteries," *Dynamic Systems and Control Conference*, October 17–19, 2012, Ft. Lauderdale, FL, USA.
- [25] M. Verbrugge and E. Tate, "Adaptive state of charge algorithm for nickel metal hydride batteries including hysteresis phenomena," *Journal of Power Sources*, vol. 126, pp. 236–249, 2004.
- [26] H. He, R. Xiong, X. Zhang, F. Sun, and J. Fan, "State-of-charge estimation of the lithium-ion battery using an adaptive extended Kalman filter based on an improved Thevenin model," *IEEE Transactions on Vehicular Technology*, vol. 60, pp. 1461–1469, 2011.
- [27] M. Daowd, N. Omar, J.V. Mierlo, and P.V.D. Bossche, "An extended PNGV battery model for electric and hybrid vehicles," *International Review of Electrical Engineering*, vol. 6, pp. 1692–1706, 2011.
- [28] S. Santhanagopalan and R.E. White, "Online estimation of the state of the charge of a lithium ion cell," *Journal of Power Sources*, vol. 161, pp. 1346–1355, 2006.
- [29] D.D. Domenico, G. Fiengo, and A. Stefanopoulou, "Lithium-ion battery state of charge estimation with a Kalman Filter based on an electrochemical model," *IEEE International Conference on Control Applications*, September 3–5, 2008, San Antonio, TX, USA.
- [30] S. J. Moura, N.A. Chatruvedi, and M. Krstic, "Adaptive PDE observer for battery SOC/SOH estimation," *Dynamic Systems and Control Conference*, October 17–19, 2012, Ft. Lauderdale, FL, USA.
- [31] J. Cao, N. Schofield, and A. Emadi, "Battery balancing methods: A comprehensive review," *IEEE Vehicle Power and Propulsion Conference*, September 3–5, 2008, Harbin, China.
- [32] M. Daowd, N. Omar, P.V.D. Bossche, and J.V. Mierlo, "Passive and active battery balancing comparison based on MATLAB simulation," *IEEE Vehicle Power and Propulsion Conference*, September 6–9 2011, Chicago, IL, USA.
- [33] K.Z. Guo, Z.C. Bo, L.R. Gui, and C.S. Kang, "Comparison and evaluation of charge equalization technique for series connected batteries," *IEEE Power Electronics Specialists Conference*, June 18–22, 2006, Jeju, Korea.
- [34] M. Uno, "Single- and double-switch cell voltage equalizers for series-connected lithium-ion cells and supercapacitors," *Energy Storage—Technologies and Applications; InTech*, chapter 7, pp. 149–176, 2013.

- [35] M. Uno and K. Tanaka, "Single-switch cell voltage equalizer using multistacked buck-boost converters operating in discontinuous conduction mode for series-connected energy storage cells," *IEEE Transactions on Vehicular Technology*, vol. 60, pp. 3635–3645, 2011.
- [36] M. Uno and K. Tanaka, "Single-switch multioutput charger using voltage multiplier for series-connected lithium-ion battery/supercapacitor equalization," *IEEE Transactions on Industrial Electronics*, vol. 60, pp. 3227–3239, 2013.
- [37] A.M. Imtiaz and F.H. Khan, "Time shared flyback converter based regenerative cell balancing technique for series connected Li-ion battery strings," *IEEE Transactions on Power Electronics*, vol. 28, pp. 5960–5975, 2013.
- [38] S.J. Moura, N.A. Chatruvedi, and M. Krstic, "Constraint management in li-ion batteries: A modified reference governor approach," *American Control Conference*, June 17–19, 2013, Washington, DC, USA.
- [39] G.L. Plett, "Sigma-point Kalman filtering for battery management systems of LiPB-based HEV battery packs: Part 1: Introduction and state estimation," *Journal of Power Sources*, vol. 161, pp. 1356–1368, 2006.
- [40] I.-S. Kim, "A technique for estimating the state of health of lithium batteries through a dual-sliding-mode observer," *IEEE Transactions on Power Electronics*, vol. 25, pp. 1013–1022, 2010.
- [41] M. McIntyre, T. Burg, D. Dawson, and B. Xian, "Adaptive state of charge (SOC) estimator for a battery," *American Control Conference*, June 14–16, 2006, Minneapolis, MN, USA.
- [42] Y. Hu and S. Yurkovich, "Battery state of charge estimation in automotive applications using LPV techniques," *American Control Conference*, June 30–July 2, 2010, Baltimore, MD, USA.
- [43] J. Remmliner, M. Buchholz, M. Meiler, P. Bernreuter, and K. Dietmayer, "State-of-health monitoring of lithium-ion batteries in electric vehicles by on-board internal resistance estimation," *Journal of Power Sources*, vol. 196, pp. 5357–5363, 2011.
- [44] G.L. Plett, "Extended Kalman filtering for battery management systems of LiPB-based HEV battery packs: Part 3. State and parameter estimation," *Journal of Power Sources*, vol. 134, pp. 277–292, 2004.
- [45] M. Verbrugge, "Adaptive, multi-parameter battery state estimator with optimized time-weighting factors," *Journal of Applied Electrochemistry*, vol. 37, pp. 605–616, 2007.

II. REDUCED-ORDER ELECTROCHEMICAL MODEL-BASED SOC OBSERVER WITH OUTPUT MODEL UNCERTAINTY ESTIMATION

ABSTRACT

As an integral part of energy storage systems, Li-ion batteries require extensive management to guarantee their safe and efficient operation. Estimation of the remaining energy capability of the battery, usually expressed in terms of State of Charge (SOC), plays an important role in any battery-powered application. Electrochemical model-based estimation techniques have proven very attractive for this purpose due to the additional information they provide regarding the internal battery operating conditions. A modified reduced-order model based on the Single Particle (SP) approximation of the electrochemical model, suitable for the real-time implementation of SOC estimation, is employed in this work. This model, while maintaining some of the physical insight about the battery operation, provides a basis for an output-injection observer design to estimate the SOC. Output model uncertainties, originating primarily from the electrolyte-phase potential difference approximation and encountered mainly at higher discharge rates, are handled by incorporating an adaptation algorithm in the observer. Therefore, the proposed method, while being suitable for online implementation, provides an electrochemical model-based solution for battery SOC estimation over a wide range of operation. System stability and the robustness of the estimates given measurement noise are proved analytically using Lyapunov stability. Finally, accurate performance of the proposed SOC estimation technique is illustrated using simulation data obtained from a full-order electrochemical model of a Lithium Manganese Oxide (LMO) battery.

1. INTRODUCTION

Recently Li-ion batteries have become the mainstream energy storage solution in a majority of battery-powered applications. They are already well-established as energy sources in portable consumer electronics and are being extensively adopted in electrified transportation and stationary energy storage systems. Lithium-ion batteries play an important role in the integration of various renewable energy sources to existing power infrastructures. Furthermore, they can significantly improve the reliability and efficiency of the utility industry and reduce its operational and capital costs [1].

A typical Li-ion battery has three main domains: negative electrode, positive electrode, and separator. The most commonly-used material for the negative electrode is graphite, whereas the positive electrode is typically composed of a metal oxide such as Lithium Cobalt Oxide (LiCoO_2), Lithium Iron Phosphate (LiFePO_4), Lithium Manganese Oxide (LiMn_2O_4) or Lithium Nickel Manganese Cobalt Oxide ($\text{LiNiMnCoO}_2/\text{NMC}$), depending on the application. Furthermore, filler and binder materials are also added to both electrodes for structural integrity. The separator between the electrodes acts as an electron insulator. The electrodes and separator assembly are immersed inside an electrolyte, which is usually a lithium salt in an organic solvent. During discharge, in an intercalation process, lithium ions in the active material of the negative electrode diffuse to the surface where they transfer from the solid-phase to electrolyte-phase. They then travel via the mechanism of diffusion and migration to the positive electrode where they react with the active material and insert inside it. During this process, electrons released in the negative electrode travel through the external circuit to generate a flow of current.

The processes occurring in the positive and negative electrodes are reversed during charging.

To ensure the safe and efficient performance of Li-ion batteries, they must be equipped with advanced management strategies. One of the most important functionalities of any Battery Management System (BMS) is to predict the operating scope of the battery, which is usually expressed in terms of State of Charge (SOC). Furthermore, accurate information about battery SOC is crucial in other BMS functionalities such as state of health estimation, cell balancing, and battery energy management, and can potentially result in improved utilization [2]. The main challenge in determining a battery's SOC is the fact that SOC is not directly measurable, necessitating an estimation routine. Model-based estimation algorithms are the most commonly-used techniques in order to obtain battery SOC. In these methods, SOC is considered as a state of a battery model and an estimator, combined with current, voltage, and temperature measurements, is used to estimate SOC.

Equivalent-circuit models, in which the battery internal characteristics are emulated through circuit elements, are widely used in the SOC estimation literature due to their low complexity and ease of online implementation. They, however, have low fidelity and limited prediction capability; therefore, higher accuracies can only be attained by considering time-variant model parameters which, in turn, dramatically increase the estimator's complexity. The SOC estimation methods based on equivalent circuit models include different model variations along with various control and estimation methods. Some of these works include stochastic filters such as Extended [3-

8] and Unscented [9] Kalman filters and deterministic approaches such as sliding-mode [10-13], adaptive [14-16], linear parameter-varying [17] observers, and H_∞ filters [18].

Electrochemical models, on the other hand, can facilitate a more accurate insight about the performance of a Li-ion battery cell, based on porous electrode and concentrated solution theories. The Pseudo Two-Dimensional (P2D) electrochemical model proposed by Fuller et al. [19] is among the first such models. This P2D model describes the performance of a Li-ion battery through the time evolution of its solid-phase Li-ion concentration and potential, electrolyte-phase concentration and potential, and reaction current density and overpotential, using a set of coupled Partial Differential Equations (PDEs).

Although electrochemical P2D models can provide accurate predictions of the cell behavior over a wide range of operating conditions, they have high computational complexity and, therefore, are not suitable for online implementation. To overcome this issue, various model reduction techniques have been proposed [20-22]. The Single Particle (SP) model, originally proposed by Santhanagopalan et al. [20], which assumes a uniform current density distribution across each electrode and, therefore, approximates each electrode with a single spherical intercalation particle, is the most common reduced-order model. Further model simplification is achieved by ignoring the electrolyte-phase potential and assuming a constant electrolyte-phase concentration [20]. Such assumptions are valid only for low C-rates and the cells with small electrode thicknesses or high electrode conductivities [23]. Despite its simplicity, radial-domain PDEs in the SP model still need to be solved in order to obtain the solid-phase Li-ion concentration. Therefore, further approximations are required to simplify these equations. Subramanian et al. [24]

proposed a polynomial approximation in which the polynomial coefficients correspond to average and surface lithium concentrations and fluxes and can be solved using a set of Ordinary Differential Equations (ODEs). Other approximations include finite difference methods which transform the original problem into a set of ODEs whose dimension is dependent on the discretization length [25, 26] and the eigenfunction expansion method [27]. Most of the reduced-order electrochemical models lack accuracy at high C rates as higher model fidelity can only be achieved by incorporating high-dimension approximations that, in turn, will increase the model complexity.

In the past few years, a great deal of attention has been given to the use of electrochemical models, especially SP models, for SOC estimation. The estimation techniques that utilize these models include steady-state Kalman filter [28], Unscented Kalman filter [29], Extended Kalman filter [25], Particle filter [30], and Iterated Extended Kalman filter [31]. Despite their promising implementation results, issues such as time-consuming estimator parameter tuning, high computational cost, and lack of analytical stability analysis limit the applicability of these methods. The SP model was used with a finite difference approximation of the solid-phase lithium concentration in Dey et al. [26] to design a sliding-mode observer for SOC estimation. The proposed observer is augmented with update laws to adapt some of the model parameters online and is shown to have acceptable state estimation both in simulations and practice. The authors in Wang et al. [32] used a second-order polynomial approximation of the solid-phase lithium concentration to obtain an SP model composed of a single ODE along with the output voltage equation. They then used state transformations in order to transform the system dynamics into a form suitable for observer design and, using geometric

approaches, proposed an observer to adaptively estimate the SOC as one of the output equation model parameters. Moura et al. [23] proposed an adaptive backstepping observer for SOC estimation based on the SP model with the original radial-domain PDE for solid-phase concentration. The stability analysis and the identification procedure for some of the model parameters were discussed in this work. Finally, a Luenberger observer based on an almost full-order P2D electrochemical model of a Li-ion cell composed of various active materials was proposed in [33]. A fourth-order polynomial approximation of the solid-phase lithium concentration is the only model simplification which was considered in this paper. Simulation and experimental results were presented that demonstrate good performance of the proposed observer. Despite promising results of the existing electrochemical model-based SOC estimation algorithms, there is still need for a single solution having analytical stability analysis, high accuracy, and low computational cost, especially in resource-constrained applications.

In this paper, an output-injection observer for SOC estimation based on the SP model and a fourth-order polynomial approximation of the solid-phase concentration is proposed. An empirical current-dependent approximation for the output equation uncertainty is augmented to the model in order to increase the model fidelity. Furthermore, an adaptation algorithm based on least squares is incorporated within the observer to estimate the coefficients of the output equation uncertainty approximation online. This adaptation algorithm enables accurate SOC estimation even at high C rates. In addition to simulation studies validating the performance of the proposed estimation method, the convergence of the state estimates to their true values and the boundedness of the estimation errors in the presence of voltage and current measurement noises are

proved using Lyapunov stability. Therefore, the proposed electrochemical model-based observer can facilitate an accurate online SOC estimation methodology without imposing any constraints on the battery input current.

2. MODELING

Inside the active material of each electrode, the Li-ion concentration in spherical coordinates can be described by Fick's law

$$\frac{\partial c_{s,j}(r,t)}{\partial t} = \frac{D_{s,j}}{r^2} \frac{\partial}{\partial r} \left(r^2 \frac{\partial c_{s,j}(r,t)}{\partial r} \right) \quad (1)$$

where $c_{s,j}$ is the solid-phase Li-ion concentration (mol/m³), t is time (s), r is the radial coordinate (m), $D_{s,j}$ is the solid-phase diffusion coefficient (m²/s), and the subscript $j = p/n$ denotes the positive/negative electrode. The PDE in Eq. (1) is subject to the following boundary conditions

$$\left(D_{s,j} \frac{\partial c_{s,j}}{\partial r} \right)_{r=0} = 0 \quad \left(D_{s,j} \frac{\partial c_{s,j}}{\partial r} \right)_{r=R_j} = -J_j(t) \quad (2)$$

where R_j is the particle radius (m) and J_j is the Li-ion molar flux density on the active material surface (mol/(m²/s))

$$J_j(t) = \pm \frac{R_j i_{t,j}(t)}{3 \varepsilon_{1,j} l_j F} \quad (3)$$

where $i_{t,j}$ is the cell current density (A/m²), $\varepsilon_{s,j}$ is the solid-phase volume fraction, l_j is the electrode length (m), and F is Faraday's number (C/mol). The sign in Eq. (3) is positive for the negative electrode and negative for the positive electrode.

In this work, the radial dependence of the solid-phase concentration in each electrode is approximated by a fourth-order polynomial [24]

$$c_{s,j}(r,t) = a(t) + b(t)\left(\frac{r^2}{R_j^2}\right) + c(t)\left(\frac{r^4}{R_j^4}\right) \quad (4)$$

By substituting the polynomial approximation in Eq. (4) into Eq. (1), the coefficients $a(t)$, $b(t)$, and $c(t)$, respectively, are

$$\begin{aligned} a(t) &= \frac{39}{4}c_{s,j,\text{surf}}(t) - 3R_jq_{s,j,\text{avg}}(t) - \frac{35}{4}c_{s,j,\text{avg}}(t) \\ b(t) &= -35c_{s,j,\text{surf}}(t) + 10R_jq_{s,j,\text{avg}}(t) + 35c_{s,j,\text{avg}}(t) \\ c(t) &= \frac{105}{4}c_{s,j,\text{surf}}(t) - 7R_jq_{s,j,\text{avg}}(t) - \frac{105}{4}c_{s,j,\text{avg}}(t) \end{aligned} \quad (5)$$

where $c_{s,j,\text{surf}}$ is the particle surface concentration (mol/m³), $c_{s,j,\text{avg}}$ is the average solid-phase concentration (mol/m³), and $q_{s,j,\text{avg}}$ is the average solid-phase flux (mol). By using the boundary conditions in Eq. (2) after substituting the polynomial approximation in Eq. (4) into Eq. (1), the following ODEs are obtained to describe the average solid-phase concentration and average solid-phase flux, respectively

$$\frac{dc_{s,j,\text{avg}}(t)}{dt} = -3\frac{J_j(t)}{R_j} \quad (6)$$

$$\frac{dq_{s,j,\text{avg}}(t)}{dt} = -30\frac{D_{s,j}}{R_j^2}q_{s,j,\text{avg}}(t) - \frac{45}{2R_j^2}J_j(t) \quad (7)$$

Furthermore, the normalized particle surface concentration is

$$x_{s,j,surf}(t) = \frac{c_{s,j,surf}(t)}{c_{s,j,max}} = \frac{\left(c_{s,j,avg}(t) + \frac{8R_j}{35} q_{s,j,avg}(t) - \frac{R_j}{35D_{s,j}} J_j(t) \right)}{c_{s,j,max}} \quad (8)$$

The Li-ion molar flux density, J_j , is an indication of the electrochemical reaction rate for the Li-ion intercalation/deintercalation at the solid/solution interface. It is related to the individual electrodes overpotential through the Butler-Volmer kinetics

$$J_j(t) = k_j c_{s,j,max} c_e^{0.5} (1 - x_{s,j,surf}(t))^{0.5} x_{s,j,surf}(t)^{0.5} \left\{ \exp\left(\frac{0.5F}{RT} \eta_j(t)\right) - \exp\left(-\frac{0.5F}{RT} \eta_j(t)\right) \right\} \quad (9)$$

where k_j is the reaction rate constant ($\text{m}^{2.5}\text{mol}^{-0.5}\text{s}^{-1}$), c_e is the electrolyte concentration (mol/m^3), which is assumed to be constant, R is the universal gas constant ($\text{J}/\text{mol}\cdot\text{K}$), T is the ambient temperature (K), and η_j is the reaction overpotential (V) defined as $\eta_j = \Phi_{s,j} - \Phi_{e,j} - U_j$, where $\Phi_{s,j}$ is the solid-phase potential, $\Phi_{e,j}$ is the electrolyte-phase potential, and U_j is the Open Circuit Potential (OCP), which, in general, is a function of $x_{s,j,surf}$ and temperature. By solving Eq. (9) for the overpotential η_j [27]

$$\eta_j(t) = \frac{2RT}{F} \ln\left(m_j(t) + \sqrt{m_j^2(t) + 1}\right) \quad (10)$$

where

$$m_j(t) = \frac{J_j(t)}{2k_j c_{s,j,\max} c_e^{0.5} (1 - x_{s,j,\text{surf}}(t))^{0.5} x_{s,j,\text{surf}}^{0.5}(t)} \quad (11)$$

Finally, the Li-ion battery terminal voltage is

$$\begin{aligned} V_t(t) &= \Phi_{s,p}(t) - \Phi_{s,n}(t) \\ &= (U_p(x_{s,p,\text{surf}}(t)) - U_n(x_{s,n,\text{surf}}(t))) \\ &\quad + \frac{2RT}{F} \ln(m_p(t) + \sqrt{m_p^2(t) + 1}) \\ &\quad - \frac{2RT}{F} \ln(m_n(t) + \sqrt{m_n^2(t) + 1}) + (\Phi_{e,p}(t) - \Phi_{e,n}(t)) \end{aligned} \quad (12)$$

As compared to the P2D model, other terms are required to be incorporated into this equation to account for the inaccuracies resulting from the model simplifications and battery degradation mechanisms. These terms, along with the electrolyte-phase potential difference, will be referred to as output model uncertainties. There are not explicit equations to completely describe the output model uncertainties; however, they are typically modeled as an ohmic voltage drop, $R_{cell}I_t(t)$, where $I_t(t)$ is the terminal current (A). The resistance value R_{cell} depends on various mass and charge transfer phenomena [19]. In [27] it is approximated as an empirical function of the ambient temperature and the battery terminal current. The authors in [25] approximate R_{cell} as a function of the electrode's ionic conductivities and thicknesses. In general, the ohmic voltage drop approximation of the output model uncertainties is shown to improve the model accuracy. In this work, the output model uncertainties are approximated as a second-order polynomial of the input current. The second-order polynomial approximation is based on the common assumption in the literature which describes the resistance R_{cell} to be a linear

function of the terminal current [27]. Therefore, the ohmic voltage drop, which is the product of the resistance R_{cell} and the terminal current, is expressed as a quadratic function of the current in this work. As will be discussed later, updating the polynomial coefficients online can greatly improve model accuracy, which is needed for reliable SOC estimation.

The total number of lithium ions in a single particle Li-ion battery model is

$$n_{Li} = \frac{\varepsilon_{s,p} l_p A_{cell}}{\frac{4}{3} \pi R_p^3} \int_0^{R_p} 4\pi r^2 c_{s,p}(r,t) dr + \frac{\varepsilon_{s,n} l_n A_{cell}}{\frac{4}{3} \pi R_n^3} \int_0^{R_n} 4\pi r^2 c_{s,n}(r,t) dr \quad (13)$$

where A_{cell} is the electrode surface area (m²). By substituting the solid-phase concentration approximation in Eq. (4) into Eq. (13) and replacing the corresponding coefficients from Eq. (5)

$$n_{Li} = \varepsilon_{s,p} l_p A_{cell} c_{s,p,avg}(t) + \varepsilon_{s,n} l_n A_{cell} c_{s,n,avg}(t) \quad (14)$$

By taking the derivative of Eq. (14) with respect to time and replacing the corresponding ODEs in Eq. (6), it can be observed that the change in the total number of lithium ions is zero. This observation coincides with conservation of mass. Furthermore, by rearranging Eq. (14)

$$c_{s,p,avg}(t) = \nu + \omega c_{s,n,avg}(t) \quad (15)$$

where the parameters ν and ω , respectively, are

$$v = \frac{1}{\varepsilon_{s,p} l_p A_{cell}} n_{Li} \quad \omega = -\frac{\varepsilon_{s,n} l_n}{\varepsilon_{s,p} l_p} \quad (16)$$

Considering the relationship between the average electrode concentrations in Eq. (15) and defining the state vector as $\mathbf{z}(t) = [z_1(t), z_2(t), z_3(t)]^T = [c_{s,n,avg}(t), q_{s,p,avg}(t), q_{s,n,avg}(t)]^T$, the input as $u(t) = I(t)$, and the output as $y(t) = V(t)$, the system dynamics can be expressed by the following set of state equations

$$\begin{aligned} \frac{dz_1(t)}{dt} &= -\frac{u(t)}{A_{cell} \varepsilon_{s,n} l_n F} \\ \frac{dz_2(t)}{dt} &= -30 \frac{D_{s,p}}{R_p^2} z_2(t) + \frac{15u(t)}{2R_p A_{cell} \varepsilon_{s,p} l_p F} \\ \frac{dz_3(t)}{dt} &= -30 \frac{D_{s,n}}{R_n^2} z_3(t) - \frac{15u(t)}{2R_n A_{cell} \varepsilon_{s,n} l_n F} \end{aligned} \quad (17)$$

and the output equation

$$\begin{aligned} y(t) &= \left(U_p(x_{s,p,surf}(t)) - U_n(x_{s,n,surf}(t)) \right) \\ &+ \frac{2RT}{F} \ln \left(m_p(t) + \sqrt{m_p^2(t) + 1} \right) \\ &- \frac{2RT}{F} \ln \left(m_n(t) + \sqrt{m_n^2(t) + 1} \right) + \boldsymbol{\eta}^T \boldsymbol{\phi}(u(t)) \end{aligned} \quad (18)$$

where $\boldsymbol{\phi} = [1, u, u^2]^T$, $\boldsymbol{\eta} = [\eta_1 \ \eta_2 \ \eta_3]^T$, and the normalized particle surface concentrations $x_{s,n,surf}$ and $x_{s,p,surf}$, respectively, are

$$\begin{aligned}
x_{s,p,\text{surf}}(t) &= \frac{1}{c_{s,p,\text{max}}} \left[(v + \omega z_1(t)) + \frac{8R_p}{35} z_2(t) + \frac{R_p^2 u(t)}{105 D_{s,p} A_{\text{cell}} \epsilon_{s,p} l_p F} \right] \\
x_{s,n,\text{surf}}(t) &= \frac{1}{c_{s,n,\text{max}}} \left[z_1(t) + \frac{8R_n}{35} z_3(t) - \frac{R_n^2 u(t)}{105 D_{s,n} A_{\text{cell}} \epsilon_{s,n} l_n F} \right]
\end{aligned} \tag{19}$$

For the simulation studies conducted in this paper, the P2D model is simulated by the finite element method in COMSOL Multiphysics[®] using the parameters of an LMO Li-ion battery [34, 35] and the modified SP model, presented in Eqs. (17)-(19), is simulated in Matlab. The parameters used for the SP model simulations are summarized in Table 2.1. Furthermore, the coefficients of the polynomial approximation of the output model uncertainties in Eq. (18), denoted by $\boldsymbol{\eta}$, are obtained offline. More specifically, the current and voltage values obtained from the P2D model simulations for 0.2C and 1C constant discharge tests are used to fit these parameters

$$\eta_1 = 0 \quad \eta_2 = -2.646 \quad \eta_3 = -7.1850 \times 10^{-2} \tag{20}$$

Finally, the OCPs of the individual electrodes as functions of their corresponding normalized surface concentrations are shown in Figure 2.1 [34, 35].

Table 2.1. Reduced-order model parameters.

Parameter	Description	Value
$i_{i,1C}$	1C discharge current density (A/m ²)	17.5
$D_{s,n}$	solid-phase Li diffusivity, negative electrode (m ² /s)	3.9×10^{-14}
$D_{s,p}$	solid-phase Li diffusivity, positive electrode (m ² /s)	1×10^{-13}
R_n	particle radius, negative electrode (m)	12.5×10^{-6}
R_p	particle radius, positive electrode (m)	8×10^{-6}
R	universal gas constant (J/mol.K)	8.314
T	ambient temperature (K)	298.15
F	Faraday's constant (C/mol)	96487
$\varepsilon_{s,p}$	solid-phase volume fraction, positive electrode	$1 - \varepsilon_{e,p} - 0.259$
$\varepsilon_{e,p}$	electrolyte-phase volume fraction, positive electrode	0.444
$\varepsilon_{s,n}$	solid-phase volume fraction, negative electrode	$1 - \varepsilon_{e,n} - 0.172$
$\varepsilon_{e,n}$	electrolyte-phase volume fraction, negative electrode	0.357
$c_{s,n,max}$	max solid-phase concentration, negative electrode (mol/m ³)	26390
$c_{s,p,max}$	max solid-phase concentration, positive electrode (mol/m ³)	22860
$c_{s,n,0}$	initial solid-phase concentration, negative electrode (mol/m ³)	14870
$c_{s,p,0}$	initial solid-phase concentration, positive electrode (mol/m ³)	3900
k_n	reaction rate coefficient, negative electrode (m ^{2.5} mol ^{-0.5} s ⁻¹)	2×10^{-6}
k_p	reaction rate coefficient, positive electrode (m ^{2.5} mol ^{-0.5} s ⁻¹)	2×10^{-6}
l_n	negative electrode length (m)	100×10^{-6}
l_p	positive electrode length (m)	183×10^{-6}
c_e	initial electrolyte concentration (mol/m ³)	2000

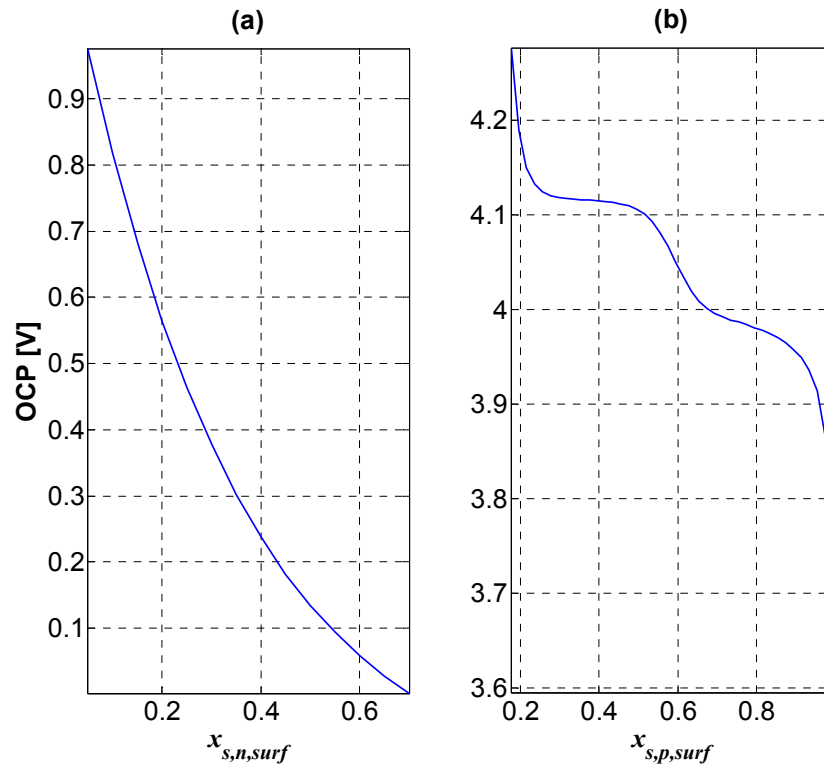


Figure 2.1. OCP of (a) negative electrode and (b) positive electrode as a function of normalized surface concentrations [34, 35].

Figure 2.2 shows a comparison between the reduced order model and the P2D electrochemical model outputs simulated in Matlab and COMSOL Multiphysics[®], respectively, during (a) 0.2C, (b) 1C, (c) 3C, and (d) 5C constant discharges. Each simulation is halted when the battery voltage reaches 3.05 V, as this is the minimum voltage for which LMO batteries can be safely operated. The Mean Average Percentage Error (MAPE) values between the two models for these tests are $3.920 \times 10^{-2}\%$, 0.2076%, 1.015%, 1.829%, respectively. For current rates above 1C, the states' spatial dependencies become increasingly significant and, therefore, a fixed-coefficient polynomial approximation increases model uncertainty.

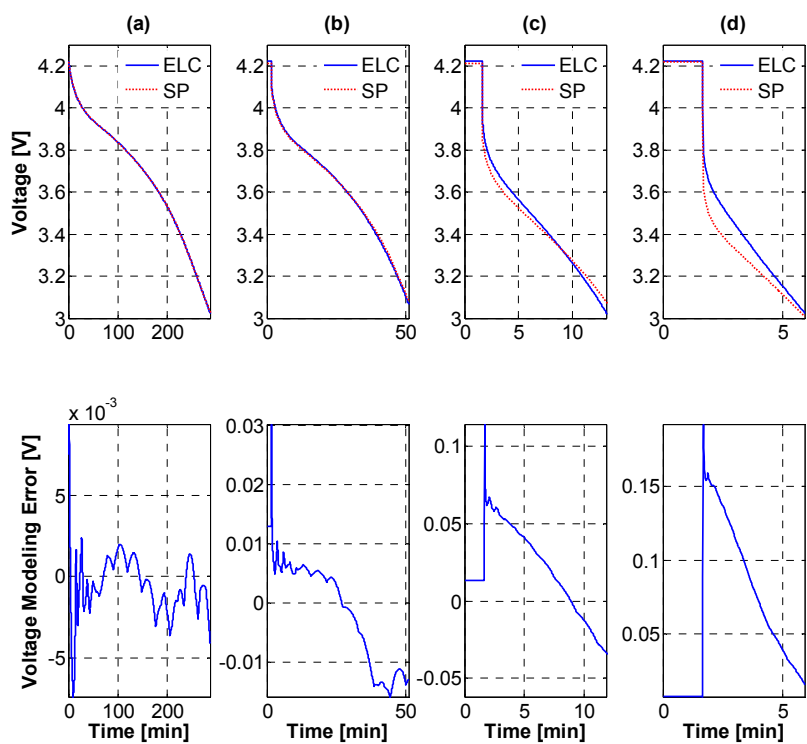


Figure 2.2. Voltages for P2D and reduced-order electrochemical models during (a) 0.2C, (b) 1C, (c) 3C, and (d) 5C constant current discharge tests.

3. SOC OBSERVER DESIGN

The change in the average lithium concentration of the negative electrode in the reduced-order model can be related to the change in the battery SOC as

$$\Delta \text{SOC} = \frac{\varepsilon_{s,n} l_n A_{\text{cell}} F \Delta c_{s,n,\text{avg}}}{3600 Q_{\text{nom}}} \quad (21)$$

where Q_{nom} is the nominal battery capacity (Ah). Equation (21) is based on the assumption that the overall cell capacity is limited by the negative electrode [36]. Therefore, the estimation of the reduced-order model states will be addressed in this section with the goal of estimating the battery SOC.

3.1. OBSERVER FORMULATION

In this section, a Luenberger-like output-injection observer, similar to [33], is proposed for the estimation of the SP model states. The modified SP model in Eqs. (17)-(19) can be written in a more compact form as

$$\begin{aligned} \frac{dz_1(t)}{dt} &= b_{c_1} u(t) \\ \frac{dz_2(t)}{dt} &= -a_{c_2} z_2(t) + b_{c_2} u(t) \\ \frac{dz_3(t)}{dt} &= -a_{c_3} z_3(t) + b_{c_3} u(t) \\ y(t) &= f_c(z_1(t), z_2(t), z_3(t), u(t)) + \boldsymbol{\eta}^T \boldsymbol{\phi}(u(t)) \end{aligned} \quad (22)$$

where

$$\begin{aligned}
a_{c_2} &= 30 \frac{D_{s,p}}{R_p^2} & b_{c_1} &= \frac{-1}{A_{cell} \epsilon_{s,n} l_n F} \\
a_{c_3} &= 30 \frac{D_{s,n}}{R_n^2} & b_{c_2} &= \frac{15}{2R_p A_{cell} \epsilon_{s,p} l_p F} \\
& & b_{c_3} &= -\frac{15}{2R_n A_{cell} \epsilon_{s,n} l_n F}
\end{aligned} \tag{23}$$

and the nonlinear function f_c is

$$\begin{aligned}
f_c &= \left(U_p(x_{s,p,surf}(t)) - U_n(x_{s,n,surf}(t)) \right) \\
&+ \frac{2RT}{F} \ln \left(m_p(x_{s,p,surf}(t)) + \sqrt{m_p^2(x_{s,p,surf}(t)) + 1} \right) \\
&- \frac{2RT}{F} \ln \left(m_n(x_{s,p,surf}(t)) + \sqrt{m_n^2(x_{s,p,surf}(t)) + 1} \right)
\end{aligned} \tag{24}$$

In order to facilitate online implementation, the continuous-time state-space representation in Eq. (22) is transformed into the discrete-time domain using a Zero-Order Hold

$$\begin{aligned}
z_1[k+1] &= z_1[k] + b_{d_1} u[k] \\
z_2[k+1] &= a_{d_2} z_2[k] + b_{d_2} u[k] \\
z_3[k+1] &= a_{d_3} z_3[k] + b_{d_3} u[k] \\
y[k] &= f_d(z_1[k], z_2[k], z_3[k], u[k]) + \boldsymbol{\eta}^T \boldsymbol{\phi}(u[k])
\end{aligned} \tag{25}$$

where

$$\begin{aligned}
a_{d_2} &= e^{-a_{c_2} t_s} & b_{d_1} &= t_s b_{c_1} \\
a_{d_3} &= e^{-a_{c_3} t_s} & b_{d_2} &= \frac{b_{c_2}}{a_{c_2}} (1 - e^{-a_{c_2} t_s}) \\
& & b_{d_3} &= \frac{b_{c_3}}{a_{c_3}} (1 - e^{-a_{c_3} t_s})
\end{aligned} \tag{26}$$

and t_s is the sampling time (s). The discrete-time state-space representation of the SP model in Eq. (25) is used as a basis to design the following observer

$$\begin{aligned}
\hat{z}_1[k+1] &= \hat{z}_1[k] + b_{d_1} u[k] + \kappa \tilde{y}[k] \\
\hat{z}_2[k+1] &= a_{d_2} \hat{z}_2[k] + b_{d_2} u[k] \\
\hat{z}_3[k+1] &= a_{d_3} \hat{z}_3[k] + b_{d_3} u[k] \\
\hat{y}[k] &= f_d(\hat{z}_1[k], \hat{z}_2[k], \hat{z}_3[k], u[k]) + \boldsymbol{\eta}^T \boldsymbol{\phi}(u[k])
\end{aligned} \tag{27}$$

where the output error term is defined as $\tilde{y}[k] = y[k] - \hat{y}[k]$. As seen in Eq. (27), the output error injection is only added to the \hat{z}_1 dynamics. The states z_2 and z_3 are weakly observable from the output voltage measurements due to their numerical conditioning; therefore, considering their intrinsic stable dynamics, they are estimated in open-loop. Therefore, the error system dynamics are

$$\begin{aligned}
\tilde{z}_1[k+1] &= \tilde{z}_1[k] - \kappa \tilde{y}[k] \\
\tilde{z}_2[k+1] &= a_{d_2} \tilde{z}_2[k] \\
\tilde{z}_3[k+1] &= a_{d_3} \tilde{z}_3[k]
\end{aligned} \tag{28}$$

where $\tilde{z}_1[k] = z_1[k] - \hat{z}_1[k]$, $\tilde{z}_2[k] = z_2[k] - \hat{z}_2[k]$, and $\tilde{z}_3[k] = z_3[k] - \hat{z}_3[k]$. In order to analyze the stability of the error system dynamics in Eq. (28), the following candidate Lyapunov function is proposed

$$V[k] = \tilde{\mathbf{z}}^T[k] \mathbf{\Gamma} \tilde{\mathbf{z}}[k] \quad (29)$$

where $\tilde{\mathbf{z}}[k] = \mathbf{z}[k] - \hat{\mathbf{z}}[k]$ and

$$\mathbf{\Gamma} = \begin{bmatrix} \gamma_1 & 0 & 0 \\ 0 & \gamma_2 & 0 \\ 0 & 0 & \gamma_3 \end{bmatrix} \quad (30)$$

for positive constants γ_1 , γ_2 , and γ_3 . Therefore, the change in the Lyapunov function is

$$\begin{aligned} V[k+1] - V[k] &= (\gamma_1 \tilde{z}_1^2[k+1] + \gamma_2 \tilde{z}_2^2[k+1] + \gamma_3 \tilde{z}_3^2[k+1]) \\ &\quad - (\gamma_1 \tilde{z}_1^2[k] + \gamma_2 \tilde{z}_2^2[k] + \gamma_3 \tilde{z}_3^2[k]) \end{aligned} \quad (31)$$

By substituting the error system dynamics, Eq. (31) can be written as

$$\begin{aligned} V[k+1] - V[k] &= -2\kappa\gamma_1 \tilde{z}_1[k] \tilde{y}[k] + \kappa^2 \gamma_1 \tilde{y}^2[k] \\ &\quad + \gamma_2 (a_{d_2}^2 - 1) \tilde{z}_2^2[k] + \gamma_3 (a_{d_3}^2 - 1) \tilde{z}_3^2[k] \end{aligned} \quad (32)$$

Using Eqs. (25) and (27), the output error term is

$$\tilde{y}[k] = f_d(\mathbf{z}[k], u[k]) - f_d(\hat{\mathbf{z}}[k], u[k]) = \tilde{f}_d[k] \quad (33)$$

Therefore, Eq. (32) can be written as

$$V[k+1]-V[k] = -2\kappa\gamma_1\tilde{z}_1[k]\tilde{f}_d[k] + \kappa^2\gamma_1\tilde{f}_d^2[k] + \gamma_2(a_{d_2}^2-1)\tilde{z}_2^2[k] + \gamma_3(a_{d_3}^2-1)\tilde{z}_3^2[k] \quad (34)$$

The term $\tilde{f}_d[k]$ can be rewritten as

$$\tilde{f}_d[k] = \frac{\tilde{f}_d[k]}{z_1[k] - \hat{z}_1[k]} (z_1[k] - \hat{z}_1[k]) \quad (35)$$

The first term on the Right Hand Side (RHS) of Eq. (35) can be thought of the slope of the function f_d w.r.t. z_1 . Analytically, this slope is

$$\frac{\partial f_d}{\partial z_1} = \frac{\partial f_d}{\partial x_{s,p,surf}} \frac{\partial x_{s,p,surf}}{\partial z_1} + \frac{\partial f_d}{\partial x_{s,n,surf}} \frac{\partial x_{s,n,surf}}{\partial z_1} \quad (36)$$

By investigating Eq. (19), it can be observed that

$$\frac{\partial x_{s,n,surf}}{\partial z_1} = \frac{1}{c_{s,n,\max}} > 0 \quad \frac{\partial x_{s,p,surf}}{\partial z_1} = \frac{\omega}{c_{s,p,\max}} < 0 \quad (37)$$

For any given input current, it can be seen from simulations that the function f_d is a monotonically decreasing function w.r.t. $x_{s,p,surf}$ and a monotonically increasing function w.r.t. $x_{s,n,surf}$. This conclusion is also reported in literature [23, 33]. Therefore, the derivative term $\partial f_d / \partial z_1$ has a positive value

$$0 < \delta_{\min} \leq \frac{\partial f_d}{\partial z_1} \leq \delta_{\max} \quad (38)$$

The maximum bound on the derivative is due to the continuity of the f_d function.

Therefore, Eq. (34) can be expressed in the form of the following inequality

$$\begin{aligned} V[k+1] - V[k] &\leq -2\kappa\gamma_1\delta_{\min}\tilde{z}_1^2[k] + \kappa^2\gamma_1\delta_{\max}^2\tilde{z}_1^2[k] \\ &\quad + \gamma_2(a_{d_2}^2 - 1)\tilde{z}_2^2[k] + \gamma_3(a_{d_3}^2 - 1)\tilde{z}_3^2[k] \\ &= (\kappa^2\gamma_1\delta_{\max}^2 - 2\kappa\gamma_1\delta_{\min})\tilde{z}_1^2[k] \\ &\quad + \gamma_2(a_{d_2}^2 - 1)\tilde{z}_2^2[k] + \gamma_3(a_{d_3}^2 - 1)\tilde{z}_3^2[k] \end{aligned} \quad (39)$$

Due to the fact that the coefficients a_{c_2} and a_{c_3} in Eq. (22) are positive,

$$\begin{aligned} a_{c_2} > 0 &\Rightarrow a_{d_2} = e^{-a_{c_2}t_s} < 1 \\ a_{c_3} > 0 &\Rightarrow a_{d_3} = e^{-a_{c_3}t_s} < 1 \end{aligned} \quad (40)$$

Therefore,

$$\begin{aligned} \gamma_2(a_{d_2}^2 - 1)\tilde{z}_2^2[k] &\leq 0 \\ \gamma_3(a_{d_3}^2 - 1)\tilde{z}_3^2[k] &\leq 0 \end{aligned} \quad (41)$$

Furthermore, the first term on the RHS of the inequality (39) is negative as long as

$$\kappa^2\gamma_1\delta_{\max}^2 - 2\kappa\gamma_1\delta_{\min} < 0 \Rightarrow \kappa < \frac{2\delta_{\min}}{\delta_{\max}^2} \quad (42)$$

which, according to the Lyapunov Stability theorem, is an indication of the asymptotic stability of the states' estimation errors.

3.2. EFFECT OF MEASUREMENT NOISE ON THE STATE ESTIMATION

In practice, the current and voltage measurements needed for the SOC observer are contaminated with noise. In this section, the measurement noise effect on the stability properties of the proposed observer is investigated. The sensor outputs u_s and y_s are assumed to have the forms $u_s[k] = u[k] + n_u[k]$ and $y_s[k] = y[k] + n_y[k]$, respectively, where n_u and n_y are the corresponding measurement noises with $\|n_u(t)\| \leq c_u$ and $\|n_y(t)\| \leq c_y$, where the upper bounds on the measurement noises are assumed to be known. Therefore, by using the sensor outputs in Eq. (27), the observer dynamics will be

$$\begin{aligned}
 \hat{z}_1[k+1] &= \hat{z}_1[k] + b_{d_1}u[k] + \kappa\tilde{y}[k] + b_{d_1}n_u[k] + \kappa n_y[k] + h(n_u[k]) \\
 \hat{z}_2[k+1] &= a_{d_2}\hat{z}_2[k] + b_{d_2}u[k] + b_{d_2}n_u[k] \\
 \hat{z}_3[k+1] &= a_{d_3}\hat{z}_3[k] + b_{d_3}u[k] + b_{d_3}n_u[k]
 \end{aligned} \tag{43}$$

where the term $h(n_u[k])$ is a nonlinear function of the current measurement noise induced in Eq. (43) from the nonlinear dependency of $\hat{x}_{s,n,\text{surf}}$, $\hat{x}_{s,p,\text{surf}}$, and therefore, \hat{y} , on the input current. By defining the measurement noise vector as $\mathbf{n}[k] = [n_u[k], n_y[k]]^T$, Eq. (43) can be written as

$$\begin{aligned}
\hat{z}_1[k+1] &= \hat{z}_1[k] + b_{d_1}u[k] + \kappa\tilde{y}[k] + \underbrace{\begin{bmatrix} b_{d_1} & \kappa \end{bmatrix} \mathbf{n}[k] + h(n_u[k])}_{g_1(\mathbf{n}[k])} \\
\hat{z}_2[k+1] &= a_{d_2}\hat{z}_2[k] + b_{d_2}u[k] + \underbrace{\begin{bmatrix} b_{d_2} & 0 \end{bmatrix} \mathbf{n}[k]}_{g_2(\mathbf{n}[k])} \\
\hat{z}_3[k+1] &= a_{d_3}\hat{z}_3[k] + b_{d_3}u[k] + \underbrace{\begin{bmatrix} b_{d_3} & 0 \end{bmatrix} \mathbf{n}[k]}_{g_3(\mathbf{n}[k])}
\end{aligned} \tag{44}$$

Therefore, the error system dynamics are

$$\begin{aligned}
\tilde{z}_1[k+1] &= \tilde{z}_1[k] - \kappa\tilde{y}[k] - g_1(\mathbf{n}[k]) \\
\tilde{z}_2[k+1] &= a_{d_2}\tilde{z}_2[k] - g_2(\mathbf{n}[k]) \\
\tilde{z}_3[k+1] &= a_{d_3}\tilde{z}_3[k] - g_3(\mathbf{n}[k])
\end{aligned} \tag{45}$$

Using the assumption in Eq. (38) and rearranging, the change in the Lyapunov function candidate in Eq. (29) along the trajectories of the error system dynamics in Eq. (45) can be expressed as

$$\begin{aligned}
V[k+1] - V[k] &\leq (\gamma_1\kappa^2\delta_{\max}^2 - 2\kappa\gamma_1\delta_{\min})\tilde{z}_1^2[k] + \gamma_1g_1^2(\mathbf{n}[k]) \\
&\quad - 2\gamma_1\tilde{z}_1[k]g_1(\mathbf{n}[k]) + 2\gamma_1\kappa\delta_{\max}g_1(\mathbf{n}[k])\tilde{z}_1[k] \\
&\quad + \gamma_2(a_{d_2}^2 - 1)\tilde{z}_2^2[k] + \gamma_3(a_{d_3}^2 - 1)\tilde{z}_3^2[k] \\
&\quad - 2\gamma_2a_{d_2}\tilde{z}_2[k]g_2(\mathbf{n}[k]) - 2\gamma_3a_{d_3}\tilde{z}_3[k]g_3(\mathbf{n}[k]) \\
&\quad + \gamma_2g_2^2(\mathbf{n}[k]) + \gamma_3g_3^2(\mathbf{n}[k])
\end{aligned} \tag{46}$$

which can be written as

$$\begin{aligned}
V[k+1] - V[k] \leq & \\
& -\tilde{\mathbf{z}}^T[k] \underbrace{\begin{bmatrix} -(\gamma_1 \kappa^2 \delta_{\max}^2 - 2\kappa\gamma_1 \delta_{\min}) & 0 & 0 \\ 0 & -\gamma_2 (a_{d_2}^2 - 1) & 0 \\ 0 & 0 & -\gamma_3 (a_{d_3}^2 - 1) \end{bmatrix}}_{\Psi_1} \tilde{\mathbf{z}}[k] \\
& + \underbrace{\begin{bmatrix} 2\gamma_1 g_1(\mathbf{n}[k])(\kappa\delta_{\max} - 1) & -2\gamma_2 a_{d_2} g_2(\mathbf{n}[k]) & -2\gamma_3 a_{d_3} g_3(\mathbf{n}[k]) \end{bmatrix}}_{\Psi_2} \tilde{\mathbf{z}}[k] \\
& + \underbrace{\begin{bmatrix} \gamma_1 g_1^2(\mathbf{n}[k]) + \gamma_2 g_2^2(\mathbf{n}[k]) + \gamma_3 g_3^2(\mathbf{n}[k]) \end{bmatrix}}_{\Psi_3}
\end{aligned} \tag{47}$$

The inequality in Eq. (47) can be written as

$$V[k+1] - V[k] \leq -\psi_1 \|\tilde{\mathbf{z}}[k]\|^2 + \psi_2 \|\tilde{\mathbf{z}}[k]\| + \psi_3 \tag{48}$$

where $\psi_1 = \lambda_{\min}(\Psi_1)$, $\psi_2 = \|\Psi_2\|$, and $\psi_3 = \|\Psi_3\|$. From the inequality in Eq. (48), it can be concluded that there always exist a lower bound for $\|\tilde{\mathbf{z}}\|$ such that if $\|\tilde{\mathbf{z}}\| \geq \zeta$, then $V[k+1] - V[k] \leq 0$. The bound ζ is the solution of equation $-\psi_1 \|\tilde{\mathbf{z}}[k]\|^2 + \psi_2 \|\tilde{\mathbf{z}}[k]\| + \psi_3 = 0$ and is given by

$$\zeta = \frac{\psi_2 + \sqrt{\psi_2^2 + 4\psi_1\psi_3}}{2\psi_1} \tag{49}$$

Therefore, it can be inferred that $\tilde{\mathbf{z}}[k]$ is ultimately bounded. This ultimate bound is calculated as follows: The Lyapunov function in Eq. (29) can be written as

$$\lambda_{\min}(\mathbf{\Gamma})\|\tilde{\mathbf{z}}[k]\|^2 \leq V[k] \leq \lambda_{\max}(\mathbf{\Gamma})\|\tilde{\mathbf{z}}[k]\|^2 \quad (50)$$

From the RHS of the inequality in Eq. (50), it can be seen that for $\|\tilde{\mathbf{z}}\| \leq \zeta$, $V(\tilde{\mathbf{z}}) \leq \lambda_{\max}(\mathbf{\Gamma})\zeta^2$. On the other hand, it was previously shown that for $\|\tilde{\mathbf{z}}\| > \zeta$, $V[k+1] - V[k] \leq 0$. Therefore, the maximum value of the Lyapunov function is $\lambda_{\max}(\mathbf{\Gamma})\zeta^2$ and the inequality in Eq. (50) is

$$\lambda_{\min}(\mathbf{\Gamma})\|\tilde{\mathbf{z}}[k]\|^2 \leq \lambda_{\max}(\mathbf{\Gamma})\zeta^2 \Rightarrow \|\tilde{\mathbf{z}}[k]\|^2 \leq \frac{\lambda_{\max}(\mathbf{\Gamma})}{\lambda_{\min}(\mathbf{\Gamma})}\zeta^2 \quad (51)$$

From the inequality in Eq. (51), it can be observed that a decrease in the value of ζ will decrease the ultimate bound on the estimation errors. By investigating Eqs. (47) and (49), it can be concluded that the value of the ultimate bound can be decreased by decreasing the maximum noise magnitude and also decreasing the observer gain.

3.3. IMPLEMENTATION RESULTS

In order to validate the performance of the proposed observer in Eq. (27), the observer is implemented on the simulation data obtained from the P2D electrochemical model and shown in Figure 2.2. In each simulation, the initial SOC is assumed to be 60% of the actual initial value in order to demonstrate the observer's insensitivity to initial conditions. Furthermore, the observer is implemented only during the loaded operation of the battery. During rest, the battery SOC can easily be obtained using the open-circuit voltage measurements whereas it is challenging to do so while the battery is being charged/discharged as the open-circuit voltage measurement is not practically possible.

Finally, as mentioned earlier, the tests are stopped as soon as the battery terminal voltage reaches about 3.05 V.

For the LMO battery chemistry considered in this work, the maximum and minimum values of the derivative in Eq. (38) and the maximum bound on the observer gain, according to Eq. (42), for different constant-current discharge tests are summarized in Table 3.1. The observer gain is chosen as $\kappa = 1000$ so that the observer can provide a fast convergence while maintaining a stability margin from the maximum bounds shown in Table 3.1.

Table 3.1. Maximum and minimum slopes in Eq. (38) and maximum bound for observer gain

	0.2C	1C	3C	5C
δ_{min}	3.975×10^{-5}	4.407×10^{-5}	4.938×10^{-5}	4.938×10^{-5}
δ_{max}	1.950×10^{-4}	1.950×10^{-4}	1.950×10^{-4}	1.950×10^{-4}
κ_{max}	2090	2317	2596	2596

Figures 3.1 and 3.2 show the estimated versus the actual voltage and SOC, respectively, for four constant discharge tests, 0.2C, 1C, 3C, and 5C. As seen in Figure 3.2, the observer is capable of estimating the actual SOC with MAPE values of 0.3211%, 1.655%, 5.005%, and 9.862% for simulations with 0.2C, 1C, 3C and 5C discharge rates, respectively. The errors for these tests are due to the discrepancy between the voltage measurements obtained from the full-order electrochemical model simulations and the reduced-order model used in the observer structure. The observer achieves SOC estimation errors of less than 0.02 for low C rates, i.e., 0.2C and 1C, in 0.6356 and 0.6806

min, respectively; however, its performance clearly deteriorates for increased discharge rates (see Figure 3.2). Therefore, the proposed model-based observer is not capable of handling the increased output model uncertainties at higher discharge rates by simple output-injection. To overcome this drawback, the observer is augmented with an adaptation algorithm in the next section in order to identify the output model uncertainties online and to facilitate a more accurate voltage model for SOC estimation.

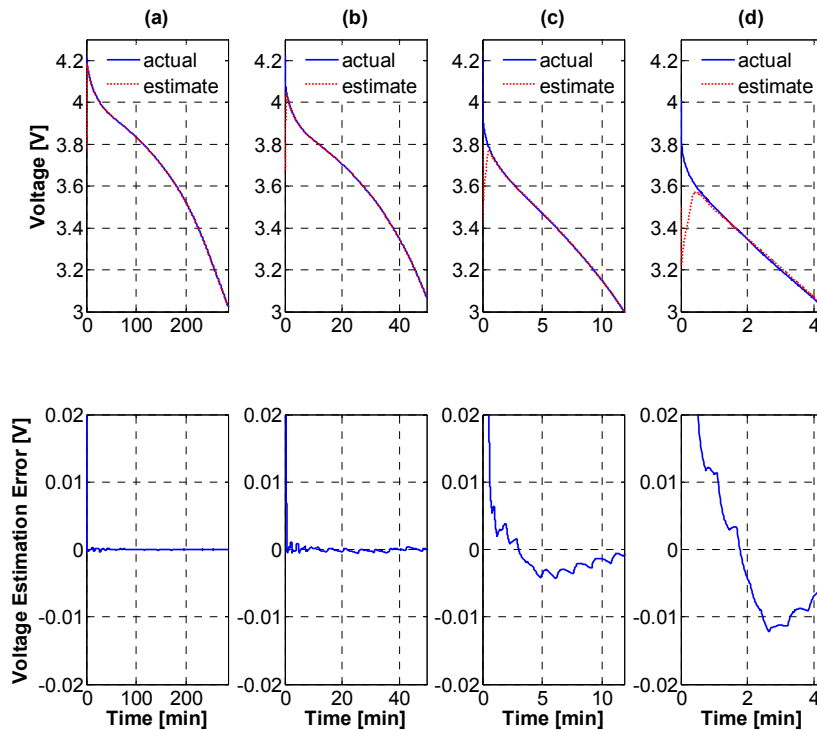


Figure 3.1. Actual versus estimated output voltage for (a) 0.2C, (b) 1C, (c) 3C, and (d) 5C constant discharge tests with the output injection observer.

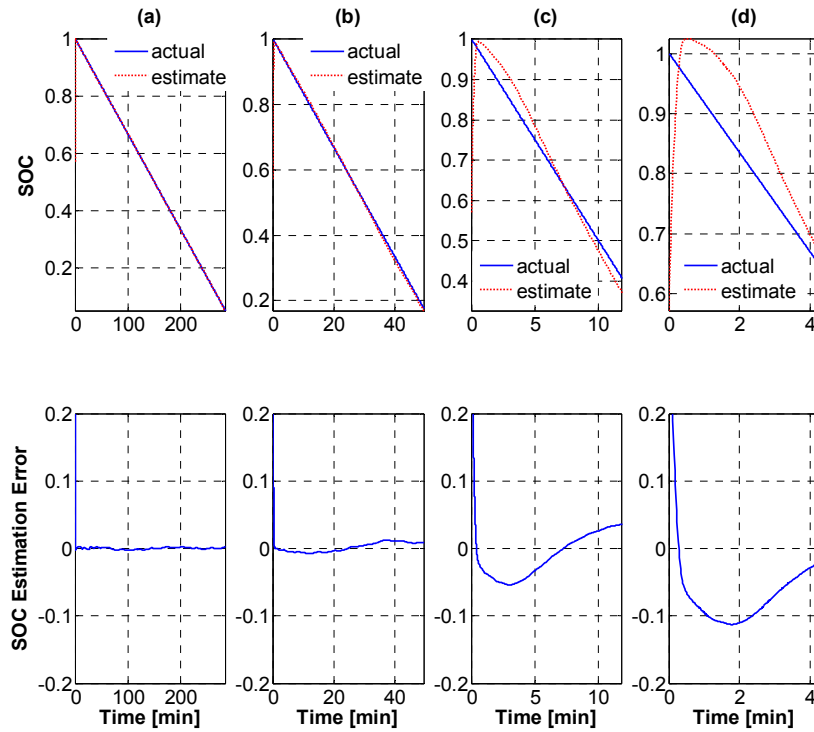


Figure 3.2. Actual versus estimated SOC for (a) 0.2C, (b) 1C, (c) 3C, and (d) 5C constant discharge tests with the output injection observer.

In order to investigate the effect of current and voltage measurement noises in simulation, it is assumed that the current measurements, used in the observer structure, have a bias of $C/16$ and are contaminated with a white noise with a variance of $C/120$. The voltage measurements are also assumed to be contaminated with a white noise with 10 mV variance. These noise magnitudes are typical for Li-ion batteries as previously reported in the literature [33]. Subplot (a) in Figure 3.3 shows the observer performance in estimating SOC with $\kappa = 1000$ for a 1C constant discharge test while exposed to the aforementioned measurement noises, which results in a MAPE of 1.902%. Subplots (b) and (c) in Figure 3.3 show the observer performance when the observer gain is multiplied by 1/5 and 5, respectively. The MAPE values for subplots 3.3(b) and 3.3(c), respectively,

are 1.566% and 2.880%. Furthermore, the observer estimates reach their true values in subplots 3.3(a), 3.3(b), and 3.3(c) in 0.5083, 3.412, and 0.1000 min, respectively. Therefore, increasing the observer gain has a positive effect on convergence speed. In order to have a consistent comparison, the MAPE values for all the subplots in Figure 3.3 are calculated after the SOC estimates reach the steady state. The increase in the MAPE values by increasing the observer gain is consistent with the analysis presented in the previous section. Based on the results presented in Figure 3.3, a trade-off should be made between the convergence speed and noise sensitivity when selecting the observer gain.

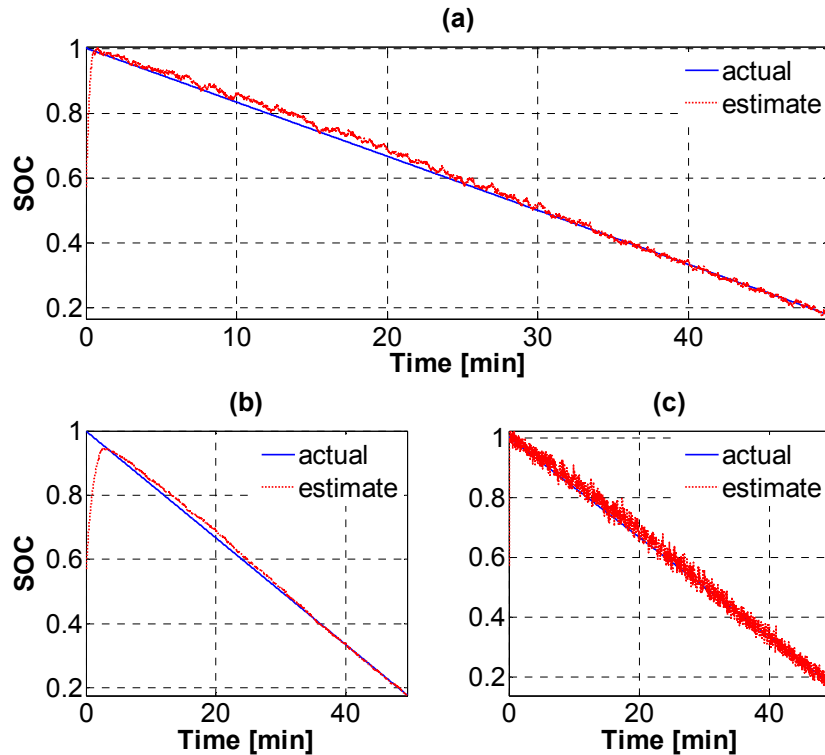


Figure 3.3. Actual versus estimated SOC when subject to current and voltage measurement noise with (a) $\kappa = 1000$, (b) $\kappa = 200$, and (c) $\kappa = 5000$, with the output injection observer.

The effect of increasing noise magnitudes on the SOC estimation MAPE values of a 1C constant discharge test is shown in Figure 3.4. In this figure, the three noise levels introduced earlier, namely current measurement noise with variance of $C/120$, current bias of $C/16$, and voltage measurement noise with variance of 10 mV, are taken as the baseline and MAPE values corresponding to increase in each of these noise levels are shown. As seen in Figure 3.4, the estimation bounds increase by increasing the noise levels which coincides with the analytical results obtained in the previous section.

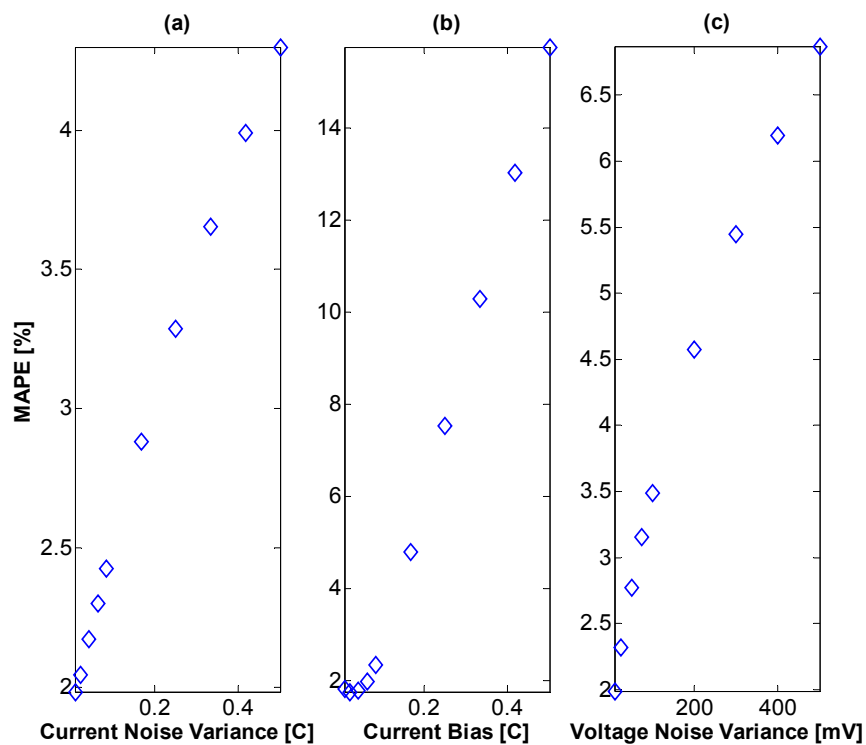


Figure 3.4. SOC estimation MAPE values with increasing (a) current noise variance, (b) current bias, and (c) voltage noise variance with the output injection observer.

4. IMPROVED SOC OBSERVER BASED ON OUTPUT MODEL UNCERTAINTY ESTIMATION

4.1. FORMULATION AND STABILITY ANALYSIS

As mentioned previously, despite the asymptotic convergence proof of the observer estimates to their true values, the observer performance deteriorates at high C rates (i.e., above 1C). At such current values, neglecting concertation and potential gradients over the spatial domain is no longer valid and, therefore, a constant-coefficient polynomial approximation of the output model uncertainties is not sufficient, resulting in large model uncertainties when using the reduced-order model. In order to overcome this issue, a Recursive Least Squares (RLS) algorithm with exponential forgetting is employed to identify the polynomial coefficients of the output model uncertainties in Eq. (22) in order to improve the SOC estimation accuracy. The following observer output equation is proposed

$$\hat{y}[k] = f_d(\hat{z}[k], u[k]) + \hat{\boldsymbol{\eta}}^T[k-1]\boldsymbol{\phi}[k] \quad (52)$$

where $\hat{\boldsymbol{\eta}}$ is an estimate of the coefficient vector $\boldsymbol{\eta}$ in Eq. (25). Therefore, the output estimation error is

$$\tilde{y}[k] = y[k] - \hat{y}[k] = \tilde{f}_d[k] + \tilde{\boldsymbol{\eta}}^T[k-1]\boldsymbol{\phi}[k] \quad (53)$$

where $\tilde{\boldsymbol{\eta}}[k] = \boldsymbol{\eta} - \hat{\boldsymbol{\eta}}[k]$. In order to identify the vector $\hat{\boldsymbol{\eta}}$ online, the following RLS algorithm is used

$$\begin{aligned}\hat{\mathbf{n}}[k] &= \hat{\mathbf{n}}[k-1] + \frac{\mathbf{P}[k-1]\boldsymbol{\phi}[k]}{\alpha + \boldsymbol{\phi}^T[k]\mathbf{P}[k-1]\boldsymbol{\phi}[k]} \tilde{y}[k] \\ \mathbf{P}[k] &= \frac{1}{\alpha} \left(\mathbf{I}_n - \frac{\mathbf{P}[k-1]\boldsymbol{\phi}[k]\boldsymbol{\phi}^T[k]}{\alpha + \boldsymbol{\phi}^T[k]\mathbf{P}[k-1]\boldsymbol{\phi}[k]} \right) \mathbf{P}[k-1]\end{aligned}\quad (54)$$

where α is the forgetting factor and \mathbf{P} is the covariance matrix. In order to investigate the stability of the overall system, the following quadratic Lyapunov function candidate is considered

$$V[k] = \tilde{\mathbf{z}}^T[k] \boldsymbol{\Gamma} \tilde{\mathbf{z}}[k] + \alpha^{-(k-1)} \tilde{\boldsymbol{\eta}}^T[k-1] \mathbf{P}^{-1}[k-1] \tilde{\boldsymbol{\eta}}[k-1] \quad (55)$$

where $\boldsymbol{\Gamma}$ is defined in Eq. (30). The change in the Lyapunov function candidate is

$$\begin{aligned}V[k+1] - V[k] &= -2\kappa\gamma_1 \tilde{z}_1[k] \tilde{y}[k] + \kappa^2 \gamma_1 \tilde{y}^2[k] \\ &\quad + \gamma_2 (a_{d_2}^2 - 1) \tilde{z}_2^2[k] + \gamma_3 (a_{d_3}^2 - 1) \tilde{z}_3^2[k] \\ &\quad + \alpha^{-(k)} \tilde{\boldsymbol{\eta}}^T[k] \mathbf{P}^{-1}[k] \tilde{\boldsymbol{\eta}}[k] \\ &\quad - \alpha^{-(k-1)} \tilde{\boldsymbol{\eta}}^T[k-1] \mathbf{P}^{-1}[k-1] \tilde{\boldsymbol{\eta}}[k-1]\end{aligned}\quad (56)$$

Using the RLS formulation in Eq. (54), it can be concluded that

$$\tilde{\boldsymbol{\eta}}[k] = \alpha \mathbf{P}[k] \mathbf{P}^{-1}[k-1] \tilde{\boldsymbol{\eta}}[k-1] - \frac{\mathbf{P}[k-1]\boldsymbol{\phi}[k]}{\alpha + \boldsymbol{\phi}^T[k]\mathbf{P}[k-1]\boldsymbol{\phi}[k]} \tilde{f}_d[k] \quad (57)$$

where the matrix $\mathbf{P}^{-1}[k-1]$ can be calculated by applying the Matrix Inversion Lemma to the covariance matrix definition in Eq. (54)

$$\mathbf{P}^{-1}[k-1] = \alpha^{-1} \mathbf{P}^{-1}[k] - \alpha^{-1} \boldsymbol{\phi}[k] \boldsymbol{\phi}^T[k] \quad (58)$$

Using Eqs. (57) and (58), and algebraically manipulating the last two terms in Eq. (56), the change in the Lyapunov function candidate is

$$\begin{aligned}
V[k+1]-V[k] &= -2\kappa\gamma_1\tilde{z}_1[k]\tilde{y}[k] + \kappa^2\gamma_1\tilde{y}^2[k] \\
&+ \gamma_2(a_{d_2}^2-1)\tilde{z}_2^2[k] + \gamma_3(a_{d_3}^2-1)\tilde{z}_3^2[k] \\
&- \alpha^{-(k-1)}\tilde{\boldsymbol{\eta}}^T[k-1]\frac{\boldsymbol{\Phi}[k]\boldsymbol{\Phi}^T[k]}{\alpha + \boldsymbol{\Phi}^T[k]\mathbf{P}[k-1]\boldsymbol{\Phi}[k]}\tilde{\boldsymbol{\eta}}[k-1] \\
&- 2\alpha^{-(k-1)}\frac{\tilde{\boldsymbol{\eta}}^T[k-1]\boldsymbol{\Phi}[k]}{\alpha + \boldsymbol{\Phi}^T[k]\mathbf{P}[k-1]\boldsymbol{\Phi}[k]}\tilde{f}_d[k] \\
&+ \alpha^{-(k)}\frac{\boldsymbol{\Phi}^T[k]\mathbf{P}[k-1]\boldsymbol{\Phi}[k]}{\alpha + \boldsymbol{\Phi}^T[k]\mathbf{P}[k-1]\boldsymbol{\Phi}[k]}\tilde{f}_d^2[k]
\end{aligned} \tag{59}$$

Furthermore, by substituting for $\tilde{y}[k]$ from Eq. (53) and grouping the like terms together, the change in the Lyapunov function candidate can be written as

$$\begin{aligned}
V[k+1]-V[k] &= \gamma_2(a_{d_2}^2-1)\tilde{z}_2^2[k] + \gamma_3(a_{d_3}^2-1)\tilde{z}_3^2[k] \\
&+ \tilde{\boldsymbol{\eta}}^T[k-1]\boldsymbol{\Phi}[k]\left(\frac{-\alpha^{-(k-1)}}{\alpha + \boldsymbol{\Phi}^T[k]\mathbf{P}[k-1]\boldsymbol{\Phi}[k]} + \kappa^2\gamma_1\right)\boldsymbol{\Phi}^T[k]\tilde{\boldsymbol{\eta}}[k-1] \\
&+ \left(2\kappa^2\gamma_1 - 2\alpha^{-(k-1)}\frac{1}{\alpha + \boldsymbol{\Phi}^T[k]\mathbf{P}[k-1]\boldsymbol{\Phi}[k]}\right)\tilde{f}_d[k]\boldsymbol{\Phi}^T[k]\tilde{\boldsymbol{\eta}}[k-1] \\
&- 2\kappa\gamma_1\tilde{z}_1[k]\boldsymbol{\Phi}^T[k]\tilde{\boldsymbol{\eta}}[k-1] \\
&+ \left(\alpha^{-(k)}\frac{\boldsymbol{\Phi}^T[k]\mathbf{P}[k-1]\boldsymbol{\Phi}[k]}{\alpha + \boldsymbol{\Phi}^T[k]\mathbf{P}[k-1]\boldsymbol{\Phi}[k]} + \kappa^2\gamma_1\right)\tilde{f}_d^2[k] - 2\kappa\gamma_1\tilde{z}_1[k]\tilde{f}_d[k]
\end{aligned} \tag{60}$$

By defining

$$q = \frac{\alpha^{-(k-1)}}{\alpha + \boldsymbol{\Phi}^T[k]\mathbf{P}[k-1]\boldsymbol{\Phi}[k]} - \kappa^2\gamma_1 \tag{61}$$

for any positive q , Eq. (60) can be written as

$$\begin{aligned}
V[k+1]-V[k] &= \gamma_2 (a_{d_2}^2 - 1) \tilde{z}_2^2[k] + \gamma_3 (a_{d_3}^2 - 1) \tilde{z}_3^2[k] \\
&\quad - q \tilde{\mathbf{\eta}}^T[k-1] \boldsymbol{\Phi}[k] \boldsymbol{\Phi}^T[k] \tilde{\mathbf{\eta}}[k-1] \\
&\quad - 2q \tilde{f}_d[k] \boldsymbol{\Phi}^T[k] \tilde{\mathbf{\eta}}[k-1] - 2\kappa\gamma_1 \tilde{z}_1[k] \boldsymbol{\Phi}^T[k] \tilde{\mathbf{\eta}}[k-1] \\
&\quad + (\alpha^{-(k)} - q) \tilde{f}_d^2[k] - 2\kappa\gamma_1 \tilde{z}_1[k] \tilde{f}_d[k]
\end{aligned} \tag{62}$$

Furthermore, based on the assumption in Eq. (38), Eq. (62) can be expressed by the following inequality

$$\begin{aligned}
V[k+1]-V[k] &\leq +\gamma_2 (a_{d_2}^2 - 1) \tilde{z}_2^2[k] + \gamma_3 (a_{d_3}^2 - 1) \tilde{z}_3^2[k] \\
&\quad - q \tilde{\mathbf{\eta}}^T[k-1] \boldsymbol{\Phi}[k] \boldsymbol{\Phi}^T[k] \tilde{\mathbf{\eta}}[k-1] \\
&\quad + (-2q\delta_{\min} - 2\kappa\gamma_1) \boldsymbol{\Phi}^T[k] \tilde{z}_1[k] \tilde{\mathbf{\eta}}[k-1] \\
&\quad + \left((\alpha^{-(k)} - q) \delta_{\max}^2 - 2\kappa\gamma_1 \delta_{\min} \right) \tilde{z}_1^2[k]
\end{aligned} \tag{63}$$

The inequality in Eq. (63) can be written in a more compact form as

$$\begin{aligned}
V[k+1]-V[k] &\leq \begin{bmatrix} \tilde{\mathbf{z}}[k] \\ \tilde{\boldsymbol{\eta}}^T[k-1] \end{bmatrix}^T \\
&\begin{bmatrix} \overbrace{\left((\alpha^{-(k)} - q) \delta_{\max}^2 - 2\kappa\gamma_1 \delta_{\min} \right)}^{\mathbf{A}_{11}} & 0 & 0 & \overbrace{-(q\delta_{\min} + \kappa\gamma_1) \boldsymbol{\Phi}^T[k]}^{\mathbf{A}_{12}} \\ 0 & \gamma_2 (a_{d_2}^2 - 1) & 0 & 0_{1 \times 3} \\ 0 & 0 & \gamma_3 (a_{d_3}^2 - 1) & 0_{1 \times 3} \\ \underbrace{-(q\delta_{\min} + \kappa\gamma_1) \boldsymbol{\Phi}[k]}_{\mathbf{A}_{21}} & 0_{3 \times 1} & 0_{3 \times 1} & \underbrace{-q\boldsymbol{\Phi}[k] \boldsymbol{\Phi}^T[k]}_{\mathbf{A}_{22}} \end{bmatrix} \quad (64) \\
&\underbrace{\hspace{10em}}_{\mathbf{A}} \\
&\begin{bmatrix} \tilde{\mathbf{z}}[k] \\ \tilde{\boldsymbol{\eta}}^T[k-1] \end{bmatrix}
\end{aligned}$$

In order for the matrix \mathbf{A} to be negative definite, its first leading minor principle should be negative; furthermore, its determinant should be positive. The determinant of \mathbf{A} is

$$\det(\mathbf{A}) = \det(\mathbf{A}_{11}) \times \det(\mathbf{A}_{22} - \mathbf{A}_{21} \mathbf{A}_{11}^{-1} \mathbf{A}_{12}) \quad (65)$$

The first leading principle minor of \mathbf{A} , which is \mathbf{A}_{11} , is negative-definite if

$$(\alpha^{-(k)} - q) \delta_{\max}^2 - 2\kappa\gamma_1 \delta_{\min} < 0 \quad (66)$$

The other two diagonal entries of \mathbf{A}_{11} are negative according to Eq. (40). Therefore, since the determinant of \mathbf{A}_{11} is negative, in order for \mathbf{A} to be negative-definite, the second determinant on the right-hand side of Eq. (65)

$$\det(\mathbf{A}_{22} - \mathbf{A}_{21}\mathbf{A}_{11}^{-1}\mathbf{A}_{12}) = \det\left(\left(-q - \frac{(q\delta_{\min} + \kappa\gamma_1)^2}{\left((\alpha^{-(k)} - q)\delta_{\max}^2 - 2\kappa\gamma_1\delta_{\min}\right)}\right)\boldsymbol{\Phi}[k]\boldsymbol{\Phi}^T[k]\right) \quad (67)$$

should be negative. Considering the properties of matrix determinants and the dimension of the matrix $\boldsymbol{\Phi}[k]\boldsymbol{\Phi}^T[k]$, the determinant in Eq. (67) is negative if

$$-q - \frac{(q\delta_{\min} + \kappa\gamma_1)^2}{\left((\alpha^{-(k)} - q)\delta_{\max}^2 - 2\kappa\gamma_1\delta_{\min}\right)} < 0 \quad (68)$$

By performing a few algebraic manipulations, the inequality in Eq. (68) can be written as

$$q > \frac{\kappa\gamma_1}{\sqrt{(\delta_{\max}^2 - \delta_{\min}^2)}} \quad (69)$$

Satisfying the condition in Eq. (69) will automatically satisfy the positive constraint on q . Furthermore, by substituting for q from Eq. (61), the inequalities in Eqs. (66) and (69) will be expressed as the following quadratic inequalities in terms of the observer gain κ

$$\kappa^2\gamma_1 + \frac{\kappa\gamma_1}{\sqrt{(\delta_{\max}^2 - \delta_{\min}^2)}} - \frac{\alpha^{-(k-1)}}{\alpha + \boldsymbol{\Phi}^T[k]\mathbf{P}[k-1]\boldsymbol{\Phi}[k]} < 0 \quad (70)$$

$$\begin{aligned} & \kappa^2\gamma_1\delta_{\max}^2 \left(\alpha + \boldsymbol{\Phi}^T[k]\mathbf{P}[k-1]\boldsymbol{\Phi}[k]\right) - \\ & 2\kappa\gamma_1\delta_{\min} \left(\alpha + \boldsymbol{\Phi}^T[k]\mathbf{P}[k-1]\boldsymbol{\Phi}[k]\right) + \\ & \alpha^{-(k)}\delta_{\max}^2 \boldsymbol{\Phi}^T[k]\mathbf{P}[k-1]\boldsymbol{\Phi}[k] < 0 \end{aligned} \quad (71)$$

In order to find the range of the acceptable observer gain κ from the above inequalities, the polynomials on the left-hand side of Eqs. (70) and (71) must have real roots. It can be shown that the polynomial in Eq. (70) always has real roots; however, for the polynomial in Eq. (71), the following condition must hold

$$\gamma_1 > \frac{\alpha^{-(k)} \delta_{\max}^4 \boldsymbol{\varphi}^T [k] \mathbf{P} [k-1] \boldsymbol{\varphi} [k]}{\delta_{\min}^2 (\alpha + \boldsymbol{\varphi}^T [k] \mathbf{P} [k-1] \boldsymbol{\varphi} [k])} \quad (72)$$

Therefore, the inequalities in Eqs. (70), (71), and (72) should be taken into account when tuning the observer. The first step in this process is to select the forgetting factor α . Decreasing the forgetting factor will result in smoother observer estimates, along with a reduced steady-state estimation error. Secondly, the observer gain should be chosen as a fraction of the maximum root of the polynomial on the left-hand side of the inequality (70), scaled such that it lies in the range admissible by the inequality in Eq. (71), resulting in a dynamic gain for the observer. The scaling factor will, then, replace the gain as an observer tuning parameter. Smaller scaling factors result in larger observer gains which, in turn, expedite the observer convergence; however, this is at the cost of larger steady-state estimation errors. By obtaining the observer gains following this procedure, the matrix \mathbf{A} will be negative-definite. Therefore, the change in the Lyapunov function along the error system trajectories will be negative, which is a sufficient condition for the asymptotic convergence of the observer estimates to their true values.

4.2. SIMULATION RESULTS

As was shown in Section 3.3, the output-injection observer in Eq. (27) failed to asymptotically estimate the actual SOC values during 3C and 5C constant discharge

simulations due to large model uncertainties and, therefore, resulted in estimation MAPEs of 5.005% and 9.861%, respectively. In order to illustrate the effectiveness of the augmented observer, it is implemented on the same 3C and 5C datasets. Note that a discharge rate of 4C is typically considered as a high-rate in batteries used as energy sources [36]. Figures 4.1 and 4.2 show the estimated versus actual voltage and SOC for both of these tests. The initial SOC estimates in both of these tests are 60% of the actual initial values. As seen from Figures 4.1 and 4.2, the voltage estimates reach within 2.631% and 5.357% of their actual values in about 0.73 and 0.33 minutes for 3C and 5C tests, respectively, after which the SOC estimates remain in 0.2625% and 0.1974% on average of the actual values, respectively. Both of these MAPE values are considerably improved compared to the estimation MAPE values obtained with only the output-injection observer in Section 3.3 and also compared to the results of Dey et al. [26] in which the authors reported an error of about 9.000% for SOC estimation of 5C discharge test based on P2D model data.

Figure 4.3 shows the time evolution of the output model uncertainty approximation coefficients identified online for 3C and 5C constant-current discharge tests as well as their offline values. As described earlier, the offline coefficients in Eq. (20) were obtained by fitting the modified SP model to voltage and current values from the P2D model simulations for 0.2 and 1C constant-discharge tests. Furthermore, as was shown in Figure 2.2, the constant-coefficient approximation is not sufficient for an accurate description of the battery voltage, especially at high C rates. Therefore, the proposed adaptation algorithm adjusts the model coefficients online to account for uncertainties in the voltage model, as seen in Figure 4.3. It can be seen in this figure that

the evolution of the coefficient estimates is dictated by the error between the SP and P2D models, shown in Figure 2.2. Therefore, by providing an accurate voltage model, the online identification scheme can greatly improve the estimation capability of the output-injection observer and facilitate state estimation at discharge rates as high as 5C.

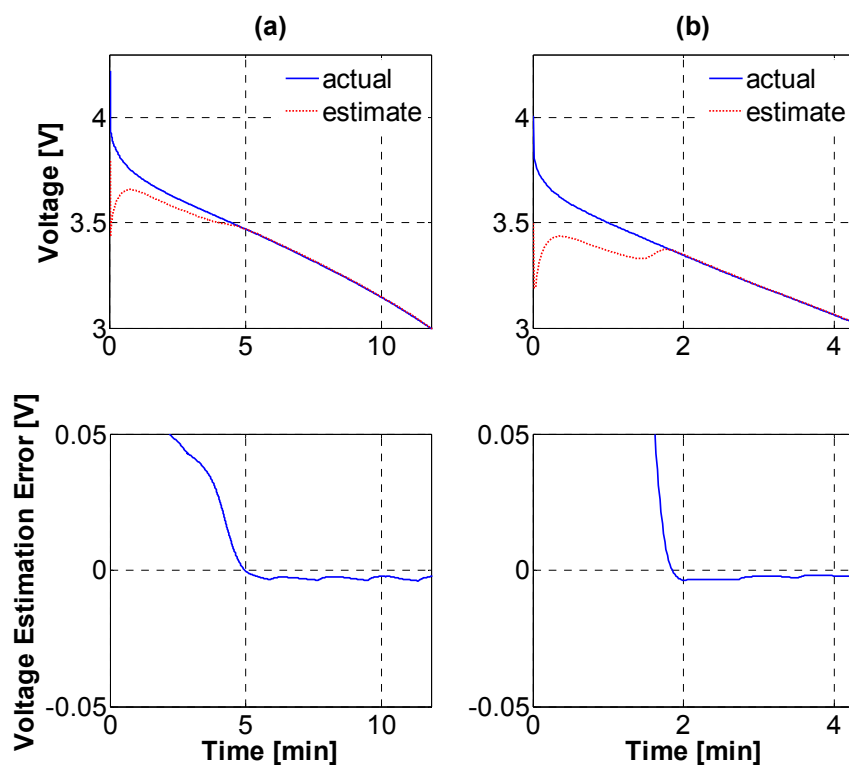


Figure 4.1. Actual versus estimated output voltage for (a) 3C and (b) 5C constant discharge simulations with the adaptive observer.

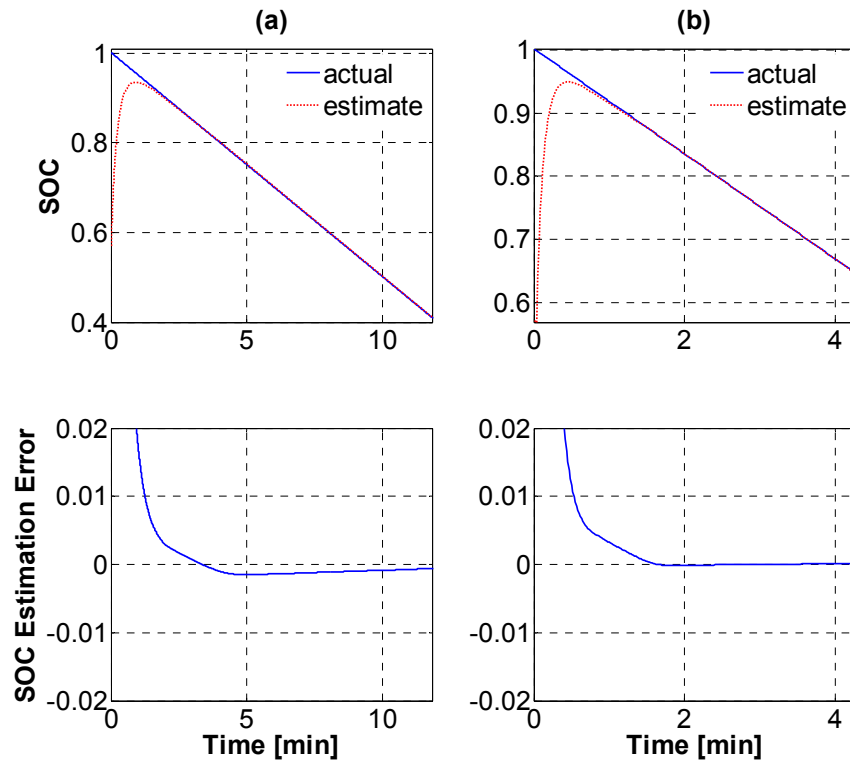


Figure 4.2. Actual versus estimated SOC for (a) 3C and (b) 5C constant discharge simulations with the adaptive observer.

Finally, the proposed observer is implemented on data corresponding to two real-world driving profiles, i.e., Urban Dynamometer Driving Schedule (UDDS) and Highway Fuel Economy Test (HWFET). The data are obtained from a Hardware-in-the-Loop (HiL) Hybrid Electric Vehicle (HEV) test bench [37] which emulates an actual HEV. Figure 4.4 shows a photograph of this test bench. The vehicle is assumed to run in pure-electric mode with the parameters reported in [37]. The battery emulator current profile is scaled to the battery cell in Table 2.1 and used as the input to the P2D model and the observer. The current profiles, along with their time derivative corresponding to UDDS and HWFET drive cycles, are shown in columns (a) and (b) of Figure 4.5, respectively. As seen in this figure, the current derivative exhibits fast jumps in the current profile

which can potentially be limiting in electrochemical model-based SOC estimation techniques requiring a smooth current profile [32].

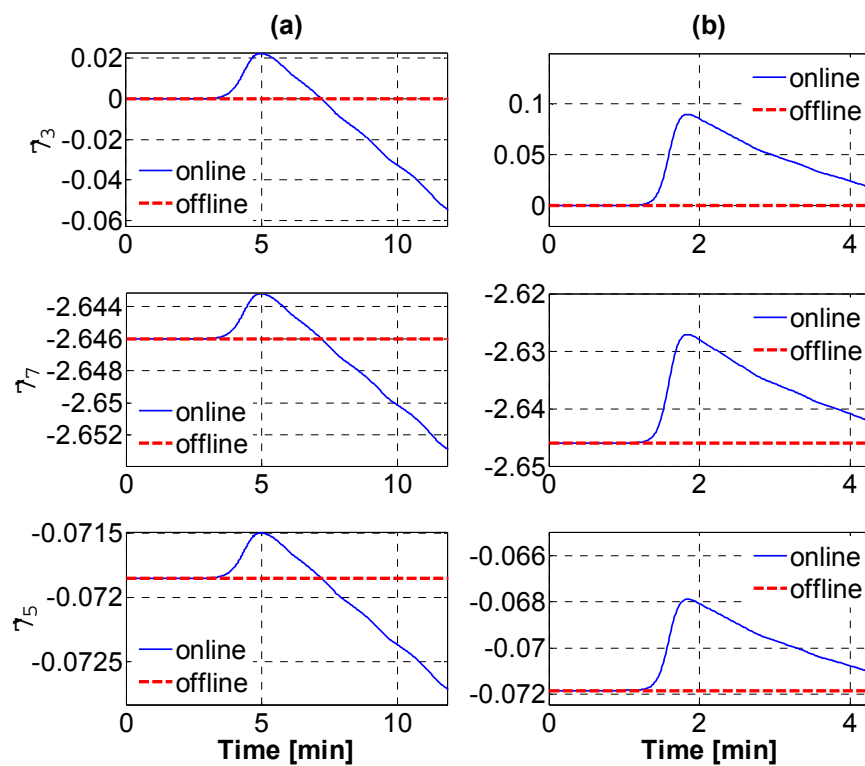


Figure 4.3. Output model uncertainty coefficients identified offline and online for (a) 3C and (b) 5C current profiles.



Figure 4.4. HiL test bench for emulating HEVs.

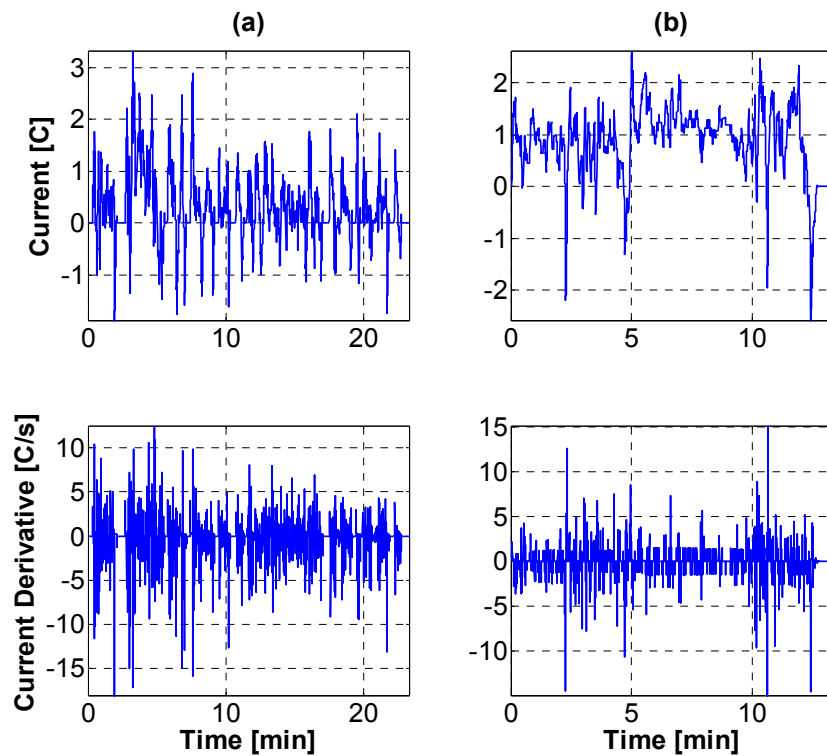


Figure 4.5. Current profile and current profile time derivative for (a) UDDES and (b) HWFET drive cycles.

The actual voltage and SOC obtained from the P2D model versus the observer estimates can be seen in Figures 4.6 and 4.7, respectively. Despite the fast changes in the current profiles, the observer implementation on the UDDS and HWFET datasets shows a good performance with MAPE values of 0.2751% and 0.2910%, respectively. Furthermore, Table 4.1 shows the sampling time, the time length of the current profile, the observer computational time, and the normalized computational time (i.e., computational time/time length) for the UDDS and HWFET current profiles. As can be seen in Table 4.1, the observer is capable of calculating the state estimates within one tenth of the sampling period. It should be noted that the proposed observer is implemented in Matlab on a desktop computer without any code optimization. Careful attention to optimizing the code structure and implementing the code on dedicated real-time processors, such as field programmable gate arrays, will dramatically decrease the observer computational time.

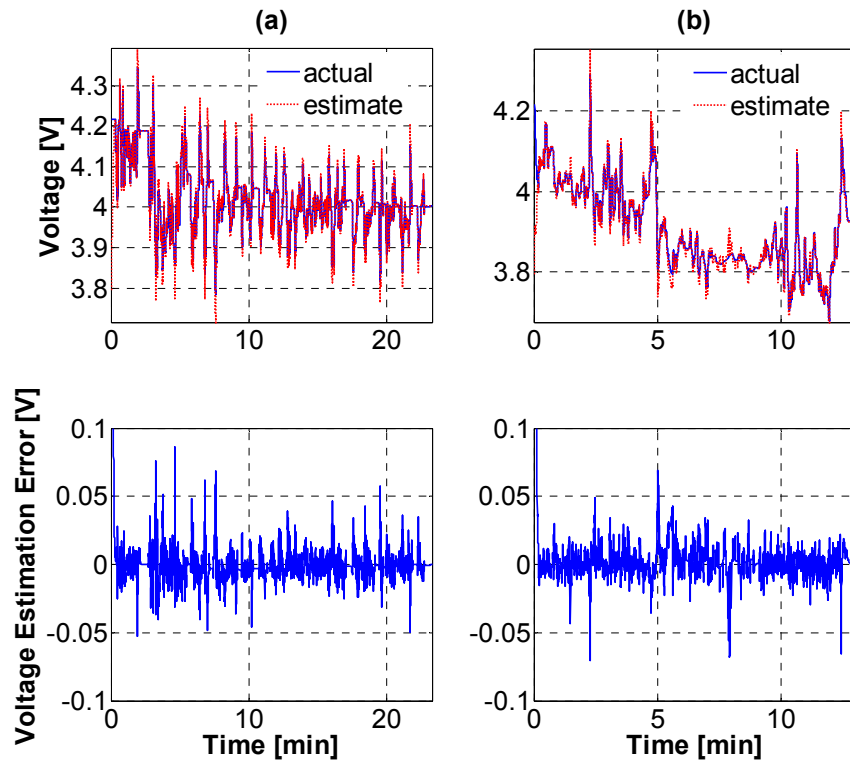


Figure 4.6. Actual versus estimated output voltage for (a) UDDS and (b) HWFET simulations with the adaptive observer.

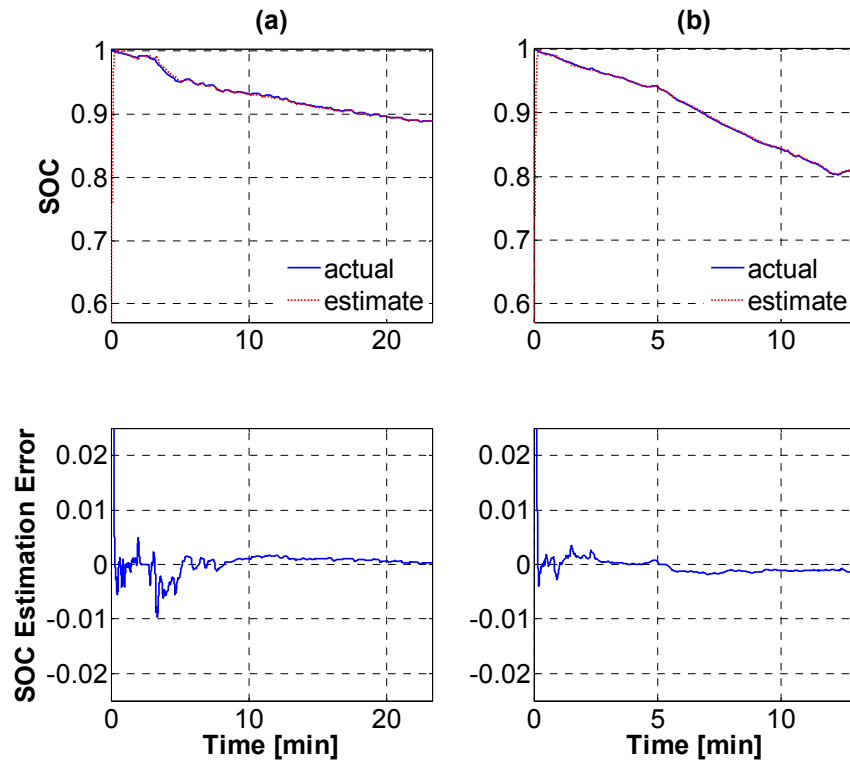


Figure 4.7. Actual versus estimated SOC for (a) UDDS and (b) HWFET simulations with the adaptive observer.

Table 4.1. Observer computational time for UDDS and HWFET current profiles

	UDDS	HWFET
Sampling Time [s]	0.1	0.1
Total Time [s]	1400	780
Computation Time [s]	8.084	4.530
Normalized Computation Time	5.774×10^{-3}	5.807×10^{-3}

5. SUMMARY AND CONCLUSIONS

In this paper, a reduced-order electrochemical model-based SOC estimation algorithm is proposed. The algorithm is based on a Luenberger-like observer coupled with an RLS with exponential forgetting parameter identification routine to compensate for the reduced-order model uncertainties. The asymptotic convergence of the state estimates to their true values is proved analytically using Lyapunov Stability. Furthermore, accurate SOC estimation with low MAPE values is achieved for a wide range of C rates. It is also observed that the state estimates reach their actual values in less than one minute, despite incorrect initial state estimates for these tests. As the proposed observer does not involve any PDE solution or matrix inversion, does not require any constraints on the battery current profile, and is analytically supported by Lyapunov theorem, it can provide an accurate and reliable electrochemical model-based solution for SOC estimation. As future work, the observer will be applied in other BMS functionalities such as State of Health (SOH) estimation. The identified output model uncertainties can be used as an indication of the battery SEI layer resistance. Furthermore, the state estimates obtained from the observer can be employed to provide an estimate of the total number of lithium ions inside the battery and, therefore, battery capacity, during open-circuit battery operation. Finally, the proposed observer design is a generic solution for state estimation in dynamic systems with output model uncertainty. In a recent work by the authors, a similar topology was implemented for internal temperature estimation of Polymer Electrolyte Membrane Fuel Cells, while simultaneously identifying the output voltage model uncertainties. The observer outputs were then used in a feedback controller to successfully regulate the output voltage.

Therefore, the proposed methodology can prove useful for state estimation in this class of dynamic systems.

REFERENCES

- [1] J.B. Goodenough and K.-S. Park, "The Li-ion rechargeable battery: A perspective," *Journal of the American Chemical Society*, vol. 135, pp. 1167–1176, 2013.
- [2] N. Lotfi, P. Fajri, S. Novosad, J. Savage, R.G. Landers, and M. Ferdowsi, "Development of an experimental testbed for research in lithium-ion battery management systems," *Energies*, vol. 6, pp. 5231–5258, 2013.
- [3] G.L. Plett, "Extended Kalman filtering for battery management systems of LiPB-based HEV battery packs: Part 3. State and parameter estimation," *Journal of Power Sources*, vol. 134, pp. 277–292, 2004.
- [4] S. Lee, J. Kim, J. Lee, and B.H. Cho, "State-of-charge and capacity estimation of lithium-ion battery using a new open-circuit voltage versus state-of-charge," *Journal of Power Sources*, vol. 185, pp. 1367–1373, 2008.
- [5] H. He, R. Xiong, X. Zhang, F. Sun, and J. Fan, "State-of-charge estimation of the lithium-ion battery using an adaptive extended Kalman filter based on an improved Thevenin model," *IEEE Transactions on Vehicular Technology*, vol. 60, pp. 1461–1469, 2011.
- [6] J. Du, Z. Liu, and Y. Wang, "State of charge estimation for Li-ion battery based on model from extreme learning machine," *Control Engineering Practice*, vol. 26, pp. 11–19, 2014.
- [7] S. Sepasi, R. Ghorbani, and B.Y. Liaw, "A novel on-board state of charge estimation method for aged Li-ion batteries based on model adaptive extended Kalman filter," *Journal of Power Sources*, vol. 245, pp. 337–344, 2013.
- [8] S. Sepasi, R. Ghorbani, and B.Y. Liaw, "Improved extended Kalman filter for state of charge estimation of battery pack," *Journal of Power Sources*, vol. 255, pp. 368–376, 2014.
- [9] F. Sun, X. Hu, Y. Zou, and S. Li, "Adaptive unscented Kalman filtering for state of charge estimation of a lithium-ion battery for electric vehicles," *Energy*, vol. 36, pp. 3531–3540, 2011.
- [10] N. Lotfi and R.G. Landers, "Robust nonlinear observer for state of charge estimation of li-ion batteries," *ASME Dynamic Systems and Control Conference*, October 17–19, 2012, Fort Lauderdale, FL, USA.
- [11] I.-S. Kim, "Nonlinear state of charge estimator for hybrid electric vehicle battery," *IEEE Transactions on Power Electronics*, vol. 23, pp. 2027–2034, 2008.

- [12] F. Zhang, G. Liu, and L. Fang, "A battery state of charge estimation method using sliding mode observer," *7th World Congress on Intelligent Control and Automation*, June 25–27, 2008, Chongqing, China.
- [13] X. Chen, W. Shen, Z. Cao, and A. Kapoor, "A novel approach for state of charge estimation based on adaptive switching gain sliding mode observer in electric vehicles," *Journal of Power Sources*, vol. 246, pp. 667–678, 2014.
- [14] M. McIntyre, T. Burg, D. Dawson, and B. Xian, "Adaptive state of charge (SOC) estimator for a battery," *American Control Conference*, June 14–16, 2006, Minneapolis, MN, USA.
- [15] M. Verbrugge, "Adaptive multi-parameter battery state estimator with optimized time-weighting factors," *Journal of Applied Electrochemistry*, vol. 37, pp. 605–616, 2007.
- [16] S. Wang, M. Verbrugge, J.S. Wang, and P. Liu, "Multi-parameter battery state estimator based on the adaptive and direct solution of the governing differential equations," *Journal of Power Sources*, vol. 196, pp. 8735–8741, 2011.
- [17] Y. Hu and S. Yurkovich, "Battery state of charge estimation in automotive applications using LPV techniques," *American Control Conference*, June 30–July 2, 2010, Baltimore, MD, USA.
- [18] Y. Zhang, C. Zhang, and X. Zhang, "State-of-charge estimation of the lithium-ion battery system with time-varying parameter for hybrid electric vehicles," *IET Control Theory and Applications*, vol. 8, pp. 160–167, 2014.
- [19] T.F. Fuller, M. Doyle, and J. Newman, "Simulation and optimization of the dual lithium ion insertion cell," *Journal of the Electrochemical Society*, vol. 141, pp. 1–10, 1994.
- [20] S. Santhanagopalan, Q. Guo, P. Ramadass, and R.E. White, "Review of models for predicting the cycling performance of lithium ion batteries," *Journal of Power Sources*, vol. 156, pp. 620–628, 2006.
- [21] N.A. Chaturvedi, R. Klein, J. Christensen, J. Ahmed, and A. Kojic, "Algorithms for advanced battery-management systems," *IEEE Control Systems Magazine*, vol. 30, pp. 49–68, 2010.
- [22] K.A. Smith, "Electrochemical control of lithium-ion batteries," *IEEE Control Systems Magazine*, vol. 30, pp. 18–25, 2010.

- [23] S. Moura, M. Krstic, and N.A. Chaturvedi, "Adaptive partial differential equation observer for battery state-of-charge/state-of-health estimation via an electrochemical model," *ASME Journal of Dynamic Systems, Measurement, and Control*, vol. 136, 011015, 2013.
- [24] V.R. Subramanian, V.D. Diwakar, and D. Tapriyal, "Efficient macro-micro scale coupled modeling of batteries," *Journal of the Electrochemical Society*, vol. 152, pp. 2002–2008, 2005.
- [25] DD. Domenico, A. Stefanopoulou, and G. Fiengo, "Lithium-ion battery state of charge and critical surface charge estimation using an electrochemical model-based extended Kalman filter," *ASME Journal of Dynamic Systems, Measurement, and Control*, vol. 132, 061302, 2010.
- [26] S. Dey, B. Ayalew, and P. Pisu, "Nonlinear robust observers for state-of-charge estimation of lithium-ion cells based on a reduced electrochemical model," *IEEE Transactions on Control Systems Technology*, vol., pp. 1–8, 2015.
- [27] M. Guo, G. Sikha, and R.E. White, "Single-particle model for a lithium-ion cell: thermal behavior," *Journal of the Electrochemical Society*, vol. 158, pp. 122–132, 2011.
- [28] S. Santhanagopalan and R.E. White, "Online estimation of the state of charge of a lithium ion cell," *Journal of Power Sources*, vol. 161, pp. 1346–1355, 2006.
- [29] S. Santhanagopalan and R.E. White, "State of charge estimation using an unscented filter for high power lithium ion cells," *International Journal of Energy Research*, vol. 34, pp. 152–163, 2010.
- [30] M. Samadi, S. Alavi, and M. Saif, "An electrochemical model-based particle filter approach for lithium-ion battery estimation," *IEEE Conference on Decision and Control*, December 10–13, 2012, Maui, Hawaii, USA.
- [31] H. Fang, Y. Wang, Z. Sahinoglu, T. Wada, and S. Hara, "Adaptive estimation of state of charge for lithium-ion batteries," *American Control Conference*, June 17–19, 2013, Washington, DC, USA.
- [32] Y. Wang, H. Fang, Z. Sahinoglu, T. Wada, and S. Hara, "Adaptive estimation of the state of charge for lithium-ion batteries: nonlinear geometric observer approach," *IEEE Transactions on Control Systems Technology*, vol. 23, pp. 948–962, 2015.
- [33] R. Klein, N. Chaturvedi, J. Christensen, J. Ahmed, R. Findeisen, and A. Kojic, "Electrochemical model based observer design for a lithium-ion battery," *IEEE Transactions on Control Systems Technology*, vol. 21, pp. 289–301, 2013.

- [34] M. Doyle, J. Newman, A.S. Gozdz, C.N. Schmutz, and J.-M. Tarascon, “Comparison of modeling predictions with experimental data from plastic lithium ion cells,” *Journal of the Electrochemical Society*, vol. 143, pp. 1890–1903, 1996.
- [35] J. Park, J.H. Seo, G. Plett, W. Lu, and A.M. Sastry, “Numerical simulation of the effect of the dissolution of LiMn₂O₄ particles on li-ion battery performance,” *Electrochemical and Solid-State Letters*, vol. 14, pp. 14–18, 2011.
- [36] K. Smith and C.-Y. Wang, “Solid-state diffusion limitations on pulse operation of a lithium ion cell for hybrid electric vehicles,” *Journal of Power Sources*, vol. 161, pp. 628–639, 2006.
- [37] P. Fajri, V.A.K. Prabhala, N. Lotfi, and M. Ferdowsi, “Emulating electric vehicle regenerative and friction braking effect using a Hardware-in-the-Loop (HIL) motor/dynamometer test bench,” *IEEE Industrial Electronics Conference*, October 29–November 1, 2014, Dallas, TX, USA.

III. PERFORMANCE CHARACTERIZATION AND CONTROL-ORIENTED MODELING OF OPEN-CATHODE FUEL CELL SYSTEMS

ABSTRACT

Open-cathode Polymer Electrolyte Membrane Fuel Cells (PEMFCs) have experienced increasing popularity in low to medium power applications in the recent years. However, they have not received much attention in the fuel cell systems literature. Furthermore, due to their low-cost nature, in practice they are usually equipped with simple open-loop controllers that, in turn, result in a reduced overall system efficiency. Aiming to overcome the control challenges regarding open-cathode PEMFCs, this paper is focused on establishing a foundation for analysis and control-oriented modeling of this type of fuel cells. More specifically, a literature survey about the temperature, humidity, and hydrogen and air supply effects on system performance, combined with experimental investigations comprise the analysis. Control-oriented nonlinear models, capable of capturing important system dynamics, are then developed and validated experimentally for individual components of air-forced open-cathode fuel cell systems. The comprehensive system-level understanding of the real-time operation of open-cathode PEMFCs and the control-oriented models developed in this paper can be used as a basis for advanced control and estimation design with ultimate goals of improving their performance, reducing their development and operational costs, and therefore, easing their widespread commercialization.

1. INTRODUCTION

While open-cathode Polymer Electrolyte Membrane Fuel Cells (PEMFCs) possess all of the advantages of closed-cathode PEMFCs, such as high efficiency and power density, long cell and stack life, low electrolyte corrosion, low noise levels, and low operating temperatures, they differ in that they have cathode channels exposed to atmosphere. In closed-cathode PEMFCs, the air is supplied by a compressor at pressures from near ambient to approximately 6 atm. On the other hand, open-cathode PEMFCs are usually operated near atmospheric pressure with the air being supplied either by convection or low-power fans. Higher pressures in closed-cathode PEMFCs mandate simultaneous cathode and anode pressure regulation in order to minimize their pressure difference [1]. However, in open-cathode PEMFC systems, due to near-atmospheric operating pressures, pressure regulation is not required. It should also be noted that although operating at higher pressures results in higher voltages, it induces considerable parasitic loads and cost (e.g., compressor, cooling system, humidification system). On the other hand, open-cathode fuel cells do not require humidification and are usually supplied with dry reactants. Novel materials such as composite catalysts in the catalyst layers, hydrophobic oxides in the Nafion membrane that increase the water uptake, and platinum catalyst in the Nafion membrane to locally generate the water [2], in addition to low operating temperatures, guarantee rapid humidification and ensure enough water is maintained in the membrane [3]. Furthermore, low humidity fuel cell operation has proved to be beneficial [4]. Therefore, open-cathode PEMFCs have become popular due to their portability and reduced number of required Balance-Of-Plant (BOP) components;

no compressors, supply or return manifolds, no cooling system components such as pumps and radiators, and no humidifiers.

There are two open-cathode PEMFC system configurations; air-breathing and air-forced. The air-breathing open-cathode PEMFC system does not have any components for air flow management; thus, air is acquired by diffusion and natural convection from the surrounding atmosphere [5]. Also, the produced water in the cathode is removed via evaporation. This configuration is suitable for applications such as cell phone emergency chargers. However, for higher powers, the generated heat needs to be actively dissipated; therefore, more air is required for the cathodic reaction [5-6]. In this case, air-forced systems, in which the cathode system consists of a fan or a blower to provide airflow through the cathode channels, are more desirable.

Water transport and content inside different fuel cell compartments are some of the important factors affecting its performance. Water is produced in the catalyst layers during reactions in the cathode and due to the water concentration gradient between the cathode and anode, water molecules diffuse through the membrane towards the anode, a process called back diffusion. These water molecules help humidify the membrane, which is essential for proton conductivity from the anode to the cathode. Membrane humidity and water content have a direct effect on the membrane resistance against proton transport. On the other hand, protons drag water molecules as they cross the membrane in a process called electro-osmotic drag. It is observed that at higher current draws, water transport through electro-osmotic drag exceeds the back diffusion [1].

The new generation open-cathode fuel cells design eliminates the need for external anode humidification. Water inside the fuel cells can be present as both liquid

and vapor. In the dead-end anode operation of fuel cells, liquid water molecules will settle to the bottom of the anode channels. Excess water accumulation in the anode channel can prevent hydrogen molecules from reaching the catalyst surfaces, and therefore, can result in a noticeable voltage drop. Furthermore, hydrogen starvation resulting from channel flooding can result in the corrosion of the carbon support in the cathode catalyst layer [3]. The corrosion rate is a function of the accumulated water. In addition to the water molecules, during back diffusion nitrogen and other impurities present in the air stream inside the cathode channels may be transported to the anode Gas Diffusion Layer (GDL). This nitrogen accumulation is sometimes referred to as nitrogen blanketing. Similar to water, these molecules can also displace hydrogen molecules from the reaction sites, causing hydrogen starvation. Although the nitrogen accumulation rate is much slower compared to water accumulation, it can still have detrimental effects. The detrimental effects of liquid water, water vapor, and nitrogen in the anode channel are discussed in Pokphet et al. [7] and Chen et al. [8].

Catalyst layer drying, on the other hand, can also have undesirable effects on fuel cell performance. Dry conditions inside closed-cathode fuel cells is mainly the result of high temperatures. However, for open-cathode fuel cells, dry reactants and high air mass flow rates that force the water molecules out of the cathode channels can intensify the drying. Pukrushpan et al. [9] and Pokphet et al. [7] state that both dry membranes/catalyst layers and flooded channels can cause high voltage losses, which negatively impact the performance and lifetime of PEMFCs. In [10], it is stated that dry membranes in open-cathode fuel cells used as backup units can be a major issue considering their long standby usage times. To this end, the authors employed modified Electrochemical

Impedance Spectroscopy (EIS) in order to estimate the membrane hydrations status. This information is used in order to monitor the fuel cell's capability for fast start-ups, in addition to designing standby humidity controllers.

The distributed nature of water propagation and water content inside the fuel cell necessitates the use of Partial Differential Equations (PDEs) to model their characteristics. In the last decade, a number of research groups have employed PDEs of various complexities to this end. A set of nonlinear PDEs is presented in [11] to describe the water distribution and propagation across the stack. A zero-dimensional moving front model is introduced in [12] in order to capture the water movement across the fuel cell while considering the location of the water phase transition inside the GDL. This model is later augmented with a channel model and then parameterized using in-situ measurements obtained from neutron imaging [13]. The authors in [14] use a similar moving front model to describe water propagation and accumulation in the fuel cell. This scheme represents the water propagation inside the GDL, water spilling into the anode channel, and filling and plugging of the anode channel. Finally, a multiscale model of an open-cathode fuel cell using Computational Fluid Dynamics is introduced in [15]. This model is aimed at demonstrating the effect of temperature-dependent water transport and filling dynamics of the electrode pores on the output voltage. Although the proposed models are shown to capture the coupled temperature and humidity effects on the fuel cell voltage, their high complexity and computational burden limit their applicability to control design.

Considering the aforementioned humidity effects, a proper water management strategy can greatly influence fuel cell stack life and efficiency. Optimal water

management would maintain an almost fully humidified membrane while preventing channel flooding [16]. There are numerous works in the literature on water management design for closed-cathode fuel cells [17-19]. The authors in [16] propose a dynamic water management methodology by controlling the durations of dry and humidified air flows. It is shown that by using this method the fuel cell voltage can be maintained in a narrow band. In general, water management is usually accomplished using occasional anode purging. Purging is traditionally performed as a sequence of purge pulses in two fashions: open-loop and current-based purging [20]. Inert nitrogen, water molecules, and other impurities present with the hydrogen are removed from the anode during purging, resulting in improved fuel cell performance.

An optimal purging sequence ensures improved hydrogen utilization, stack efficiency, and stack longevity while taking the fuel cell operating conditions into account. Ideally, the purge interval should be scheduled such that all of the accumulated water, nitrogen, and impurities are purged and as soon as the hydrogen front reaches the end of the channel purging stops. The period and width of the purge pulses depend mainly on the hydrogen purity and hydrogen and water permeation rates through the membrane. Special care should be given to the purge scheduling as purging too often will result in excessive hydrogen loss in addition to membrane drying. The amount of hydrogen loss depends on anode pressure, purge duration, temperature, and water and nitrogen accumulation. In addition to the hydrogen waste, long-term carbon corrosion rate, voltage losses during a purge cycle, and pressure fluctuations should also be taken into account [21-22]. It is also important to determine when to perform purging. Purging when the anode is still dry will decrease voltage due to a decrease in water and hydrogen

partial pressures. However, when the anode is flooded, purging will result in voltage recovery due to water molecule removal and an increase in the fuel cell active area [3]. Dumercy et al. [23] develop a stack model in order to determine the optimal purge frequency. They employ a constant purge pulse width; however, the purging is performed whenever one of the cell voltages drops below a certain threshold. The authors in [7-8] address the purge dynamics by investigating their effect on the fuel cell active area, hydrogen consumption, and voltage response and, therefore, the overall fuel cell system efficiency. The effect of purging on the water front propagation in the GDL and the anode channels and, subsequently, its effect on the fuel cell voltage is studied in detail in [8,14]. Based on the developed models in these works, optimization strategies are devised for the anode purge scheduling. Although the implementation results in these papers look promising, more research still needs to be conducted on the model identification and real-time implementation of the proposed methods. In open-cathode fuel cells, simple current-based purging is typically performed. Strahl et al. [3] study purging effects on the voltage considering cell location inside the stack, current density, and temperature in an open-cathode fuel cell. Voltage drop between purges is shown to be drastically smaller for cells closer to the anode entrance. Also, higher current densities result in larger voltage drops due to increased water generation and accumulation. Temperature increase is correlated to smaller voltage drops due to accelerated water evaporation. They conclude a trade-off should be made between the maximum power, stability, and system efficiency when creating a purge schedule.

Temperature has a strong effect on the fuel cell performance especially its humidity. High temperatures will increase the reactants' thermal activities, and therefore

the reaction rate, which results in a higher PEMFC system output voltage. The high temperatures can also help mitigate the water accumulation in the anode GDL through accelerating water evaporation rate. However, further temperature increase might result in cathode catalyst layer drying, which will dominate the positive effects of the temperature increase and lead to degradation and structural damage. In the fuel cell literature, substantial research has been conducted on the thermal modeling of PEMFC systems. The models developed in [24-27] account for ideal power generation, electrical power consumption, heat removed by a cooling fluid, and heat loss by convection to the environment. Meyer et al. [28] consider more details in their closed-cathode PEMFC thermal models than typical thermal models by describing the temperatures of the anode, cathode, cooling loop components, and the entire stack using the reactants' mass-flow rates.

Thermal management in air-forced open-cathode fuel cell systems is performed using air-delivery fans at the cathode entry. However, due to the long time constant of the temperature dynamics compared to other subsystem time constants and despite its importance in fuel cell system performance, thermal management is usually achieved through constant-speed fan operation and its effects are not studied rigorously. The authors in [29] propose a detailed procedure for the design and analysis of the cooling fans in a 2 kW air-forced open cathode fuel cell. Barreras et al. [30] introduce a non-model-based control strategy for a PEMFC used in a fuel cell hybrid vehicle. This controller is designed to regulate the fans' speed to some pre-defined values if the fuel cell temperature goes beyond a threshold. A high-temperature open-cathode fuel cell is developed and characterized using polarization voltage and single cell spectroscopy by

[31]. The authors, then, investigate the thermal effects on the start-up performance and polarization curve of the open-cathode fuel cells and develop a switching control algorithm to perform the coupled thermal and air flow management. Finally, aiming to maximize the fuel cell voltage and considering temperature effects, the authors in [27] design a non-model-based temperature controller and are able to show some promising simulation results.

This study provides a framework for the system-level understanding of performance and practical implementation of open-cathode fuel cells. More specifically, the performance characterization and modeling required for control design are studied in this paper. The effects of various phenomena including temperature, humidity, and hydrogen and air supply systems are analyzed by combining past research with experimental investigations. Then, a set of nonlinear control-oriented models are developed for the entire open-cathode fuel cell system. The modeling presented in this paper is built upon the authors' work in [32]. The models are taken such that they capture important dynamics of individual system components, as well as their interactions. Furthermore, applicability to practical control design and ease of identification are other factors considered in the model development. All of the developed models are identified and validated experimentally. These models were recently used as the basis for the design of an adaptive voltage regulation scheme in [33].

2. EXPERIMENTAL PERFORMANCE INVESTIGATIONS

In this section, important performance characteristics of open-cathode fuel cell systems are demonstrated using experimental observations. These results are also compared to previous work in literature.

The experimental open-cathode fuel cell system used in this work, along with some of its auxiliary components, is shown in Figure 2.1. A 500 W air-forced open-cathode PEMFC stack manufactured by Pearl Hydrogen and purchased from FuelCellsEtc is used. The fuel cell system runs in Dead-End Anode (DEA) mode. The DEA operation involves the direct feed of hydrogen to the anode using a manual pressure regulator. Two solenoid valves are used at the entrance and exit of the anode channels: the supply valve and purge valve, respectively. The former is used to initiate/stop the hydrogen flow into the fuel cell, whereas the latter is used for purging. Two 12 VDC 30 W fans with internal tachometers from NMBTM (Model No. NMB 3615KL-04W-B96) are located at the cathode exit in order to provide the air required for the fuel cell reaction and control its temperature. A mass-flow controller from Aalborg (Model No. GFC17) is used to measure the hydrogen mass-flow rate passing through the anode and also set the maximum hydrogen mass flow rate. The voltage sensor used for the stack terminal voltage measurement is a custom-made high-precision voltage divider. The current measurements are obtained using a Honeywell current sensor (Model No. CSLA2CD). Furthermore, ten temperature sensors manufactured by US Sensor (Model No. USP12397) are evenly placed among cathode channels in order to measure the internal fuel cell temperature. Two pressure sensors from Omega (Model No. PX209-015G5V) are used to measure the tank and anode inlet pressures. Finally, a programmable

electronic DC load from BK Precision (Model No. 8514) is used to emulate different fuel cell loads. Data acquisition (DAQ) and real-time control are achieved using two National Instruments cards. A multifunction card (NI-PCI 6225) is used for collecting sensor measurements and an analog output card (NI-PCI 6713) is used for supply and purge valve control, fan speed control, and communication with the mass-flow controller. The user interface with the DAQ cards is established using the Matlab xPC target toolbox.



Figure 2.1. Experimental air-forced open-cathode PEMFC system.

As mentioned in the Introduction, temperature increase in open-cathode fuel cells results in improved reaction kinetics and, therefore, increased fuel cell voltage. Figures 2.2 and 2.3 show the temperature effect on the output voltage of the experimental open-cathode fuel cell stack for current densities of 0.16 A cm^{-2} and 0.24 A cm^{-2} , respectively. The temperature shown in these figures is the average of the ten temperature sensors placed inside the cathode channels. Continuous exposure of these sensors to the cathodic

air flow causes the noise observed in the temperature measurements in Figures 2.2 and 2.3. Furthermore, the temperature profiles (subplot (b)) are achieved by adjusting the fans' PWM commands, as seen in subplot (a). The details of the temperature controller design and implementation are presented in [33].

As seen in Figures 2.2 and 2.3, an increase in the fuel cell temperature has an overall positive effect on the fuel cell performance as it results in an increase in the fuel cell output voltage. It can, however, be observed that there is a gradual decrease in the fuel cell voltage over time which can be attributed to cathode catalyst layer drying. This slow phenomenon is a result of water evaporation and desorption in the cathode catalyst layer pores which causes a reduction in the active reaction sites for protons and, therefore, voltage decline over time [15]. The gradual voltage drop is intensified at higher temperatures due to an increased evaporation rate. When the open-cathode fuel cell temperature reaches approximately 50 °C, the fuel cell voltage will start to drop drastically due to the lack of sufficient reaction sites in the dried catalyst layers. This effect was similarly observed and analyzed by Strahl et al. [15,27].

Another interesting observation is the effect of the operating temperature on the voltage and current density variations during purging in open-cathode fuel cells. Figures 2.4 and 2.5 show the voltage variations during purging for the different temperatures in Figures 2.2 and 2.3, respectively. The voltage drop during purging at 35 °C is a result of reduced hydrogen partial pressure. As the temperature increases to 40 °C, the voltage drop during purging decreases. It is speculated that this effect is attributed to an improved excess water removal from the anode channels due to increased evaporation rates. As the temperature further increases, the combination of purging and increased water

evaporation rate results in improved water removal, increasing the voltage more than the hydrogen partial pressure drop reduces it. Further investigation is needed in order to characterize this effect.

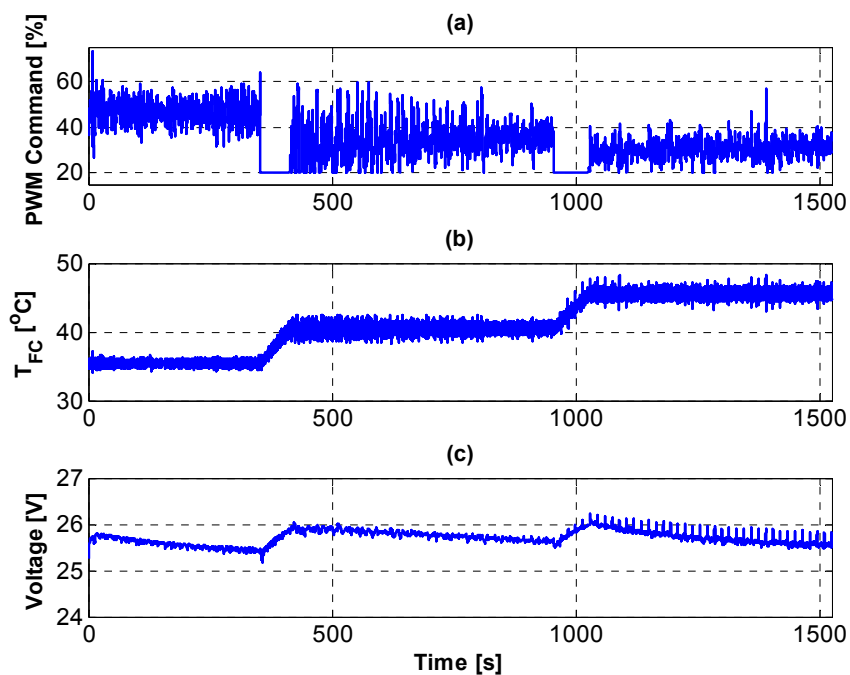


Figure 2.2. Fans' PWM command (a) in order to maintain the temperature profile (b) and the corresponding fuel cell voltage for 0.16 A cm^{-2} current density.

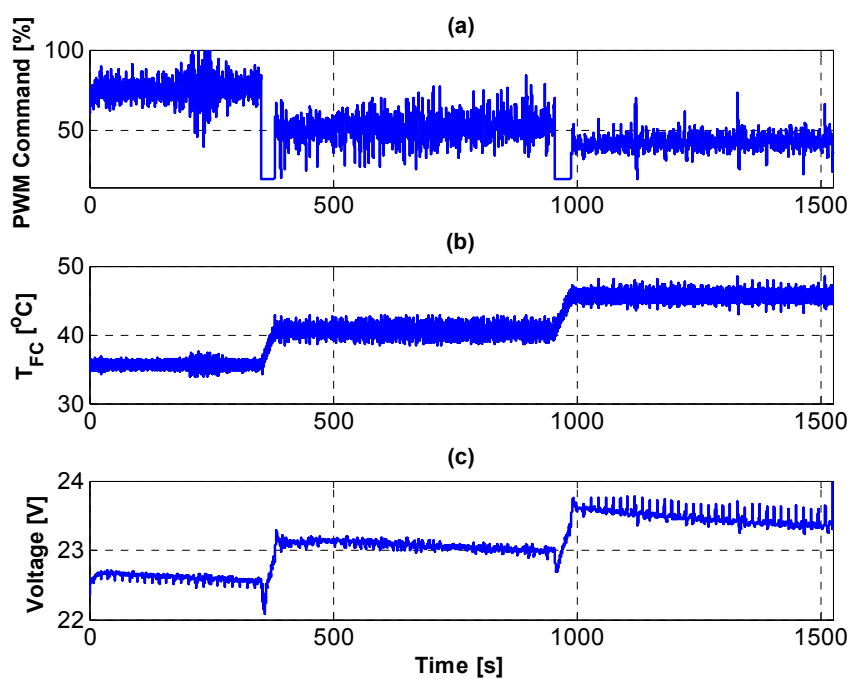


Figure 2.3. Fans' PWM command (a) in order to maintain the temperature profile (b) and the corresponding fuel cell voltage for 0.24 A cm^{-2} current density.

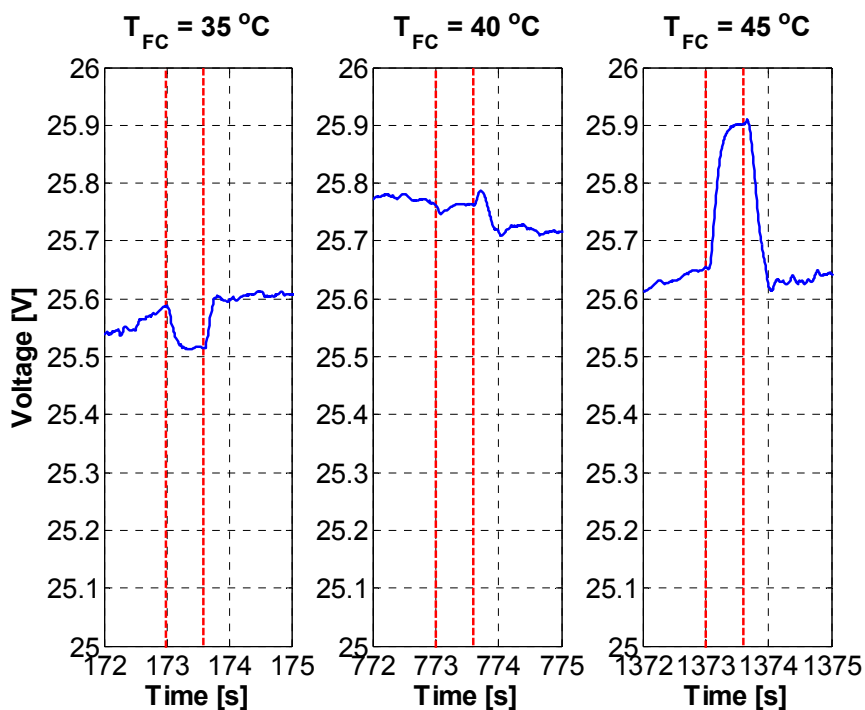


Figure 2.4. Fuel cell voltage during purging for test performed in Figure 2.2.

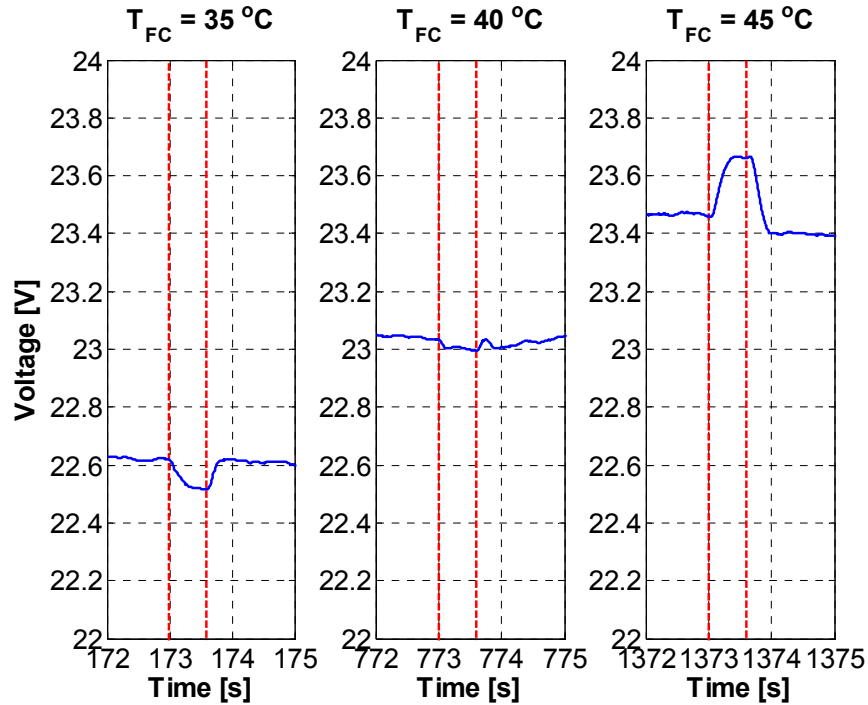


Figure 2.5. Fuel cell voltage during purging for test performed in Figure 2.3.

From these experimental observations, it can be seen that temperature has an important effect on open-cathode fuel cell performance. A trade-off between the different temperature effects discussed above can result in a temperature value which increases the fuel cell voltage while reducing its variations. After choosing the proper temperature set-point based on these considerations, a thermal management system capable of maintaining the reference temperature needs to be designed. The temperature controller design procedure is discussed in detail in [33].

Finally, a number of tests were performed in order to investigate the effect of purging duration and period on the output fuel cell voltage. Purging period and duration recommended by the manufacturer for the experimental open-cathode fuel cell system are 15 s and 600 ms, respectively. Figure 2.6 shows the results of three tests performed to

investigate the purging period effects. In each test, a current density of 0.2 A cm^{-2} and a temperature of $35 \text{ }^\circ\text{C}$ were chosen. During the first 290 s of the experiments, the manufacturer recommended purge period is used; however, for the remainder of the tests, the purge period is changed to 7.5 s and 30 s as seen in subplots (a) and (c), respectively. In the second test, shown in subplot (b), the purge period is not changed. By comparing these subplots, there does not seem to be a significant difference between the voltage values after changing the purge period.

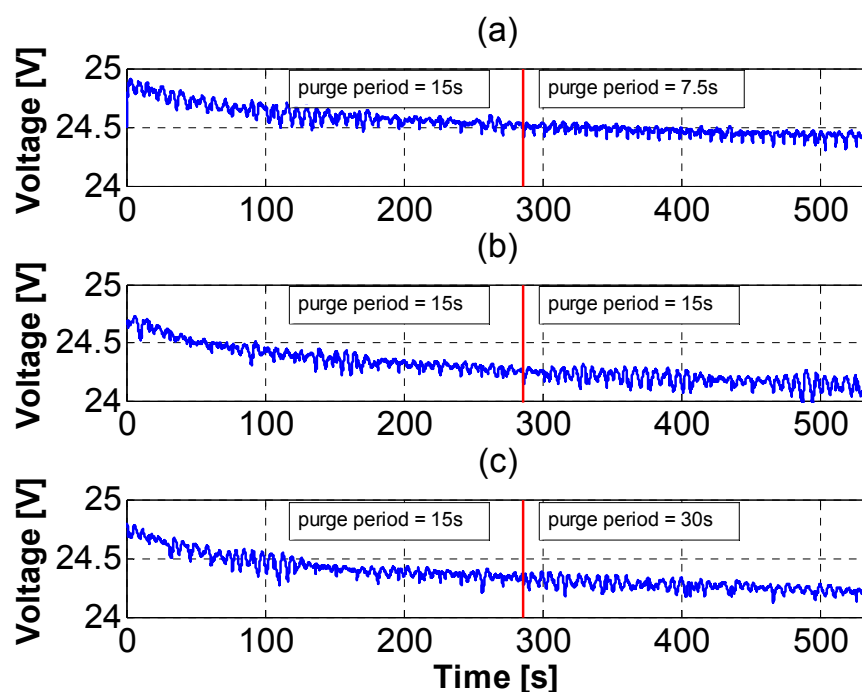


Figure 2.6. Output fuel cell voltage when changing the purge period from (a) 15 to 7.5 s, (b) 15 to 15 s, and (c) 15 to 30 s.

Similarly, Figure 2.7 shows the results of three tests performed in order to investigate the purging duration effects on the output voltage. Each test was conducted

for a current density of 0.2 A cm^{-2} and a temperature of $35 \text{ }^\circ\text{C}$. Again, during the first 290 s of the experiments, the manufacturer recommended purge duration is used; however, for the remainder of the tests, the purge duration is changed to 300 ms and 1200 ms as seen in subplots (a) and (c), respectively, and remains constant for the second test, as seen in subplot (b). Similar to the purging period, the purging duration does not appear to have a significant effect on the output voltage.

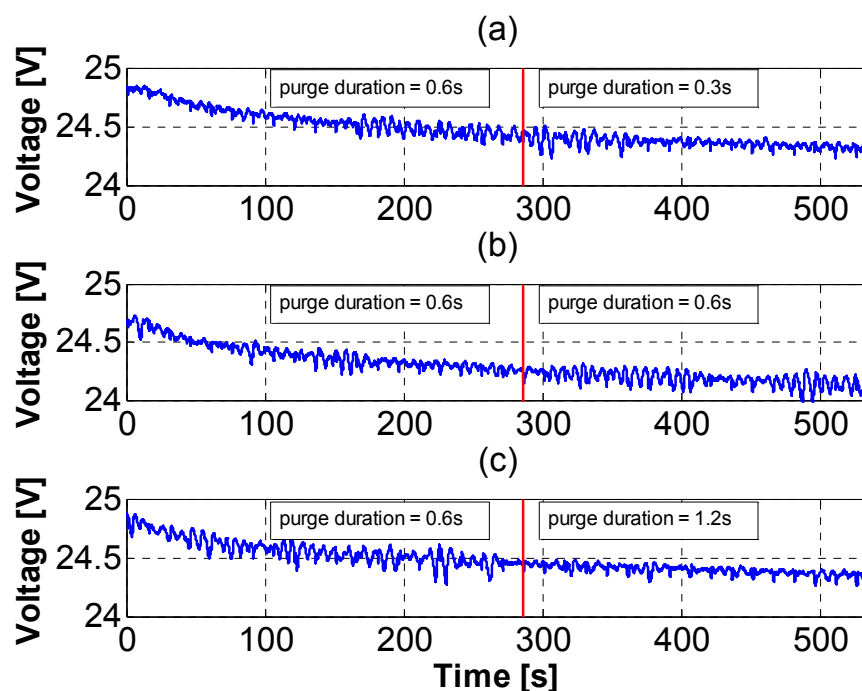


Figure 2.7. Output fuel cell voltage when changing the purge duration from (a) 600 to 300 ms, (b) 600 to 600 ms, and (c) 600 to 1200 ms.

Based on these results, it can be concluded that changes in the purge duration and period do not have a significant effect on the steady-state values of the open-cathode fuel cell output voltage. However, long-term purging effects, such as carbon corrosion, that

directly affect the fuel cell lifetime require further investigations and cannot be ignored. In this work, the purge duration and period recommended by the manufacturer are used.

3. MODELING

There are numerous papers in the literature on fuel cell modeling. In addition to the many efforts directed to high-fidelity electrochemical fuel cell modeling, control-oriented models have also attracted a fair amount of attention in the last decade [1,34-37]. The main focus of these works, however, has been on closed-cathode fuel cells. With an increased use of open-cathode fuel cells, control-oriented modeling of the entire open-cathode fuel cell system must be rigorously addressed.

3.1. VOLTAGE

For both closed and open-cathode fuel cells, the output voltage can be calculated as the ideal thermodynamic voltage resulting from the electrochemical reaction, minus voltage losses occurring inside the fuel cell. The voltage losses, namely activation, ohmic, and concentration losses, are due to the electrochemical energy barrier, ionic and electrical resistances, and reactant concentrations, respectively. In-depth discussions regarding thermodynamic fuel cell voltage and voltage losses can be found in [38]. Zhang et al. [6] describe the output voltage of air-forced open-cathode PEMFCs by modeling the activation and concentration effects. This model accounts for fuel cell stack temperature and hydrogen and oxygen flow rates, but not purging effects. Mokmeli et al. [20] develop an electrical model for an air-forced open-cathode PEMFC in which voltage losses due to hydrogen impurities are also taken into account. In other studies [1,35], a capacitance effect is introduced into the model to account for the fast dynamic behavior known as the charge double-layer effect. Temperature dependency of the fuel cell voltage is physically modeled in [15,27]. In these models, the main temperature effect is on the exchange current density. Experimental data show promising results for the model validation.

Further research on these models' identification and implementation procedures is required in order to make them suitable for control design. In order to reduce the computational complexity and facilitate control implementation, the transient effects of current density and temperature change on the fuel cell output voltage are ignored in this work and the control-oriented voltage models introduced in [1,39-40] are used as a basis for the modeling conducted in this paper. It should also be noted that the parameters' values of any model will change over time due to aging effects. A robust control and estimation methodology, such as the one presented in [33], will be able to handle these uncertainties in addition to other disturbances. Therefore, despite all of the complicated phenomena affecting the open-cathode fuel cell performance, proper control-oriented modeling can be used to design and implement robust control techniques that can account for modeling inaccuracies and systems disturbances. The control-oriented models are specifically chosen because of their ability to capture the positive temperature effects on the fuel cell voltage. In order to adapt these models to open-cathode fuel cells, two other assumptions are made. First, due to the near-atmospheric operation of open-cathode fuel cells, the cathode pressure is taken to be equal to atmospheric pressure. Secondly, saturation pressure is assumed to be independent of temperature due to the narrow operating temperature range of the open-cathode fuel cells.

The reversible or ideal voltage of a PEMFC, E^0 , can be computed using the Gibbs free energy change for the fuel cell electrochemical reactions at standard conditions, i.e., 298.15 °K and 1 atm [38]. Under non-standard conditions, the reversible voltage of a PEMFC can be calculated using the Nernst equation

$$V_{oc}(t) = E^0 + \frac{\Delta s}{2F}(T_{FC}(t) - T_{FC}^0) + \frac{RT_{FC}(t)}{2F} \left[\ln p_{H_2}(t) + \frac{1}{2} \ln p_{O_2} \right] \quad (1)$$

where t is the time (s), V_{oc} is the reversible or open-circuit fuel cell voltage (V), $\Delta s = -44.43$ is the entropy change of the reaction ($\text{J mol}^{-1} \text{K}^{-1}$), $F = 96485.34$ is Faraday's number (C.mol^{-1}), T_{FC} is the operating fuel cell temperature ($^{\circ}\text{K}$), $T_{FC}^0 = 298.15$ is the standard fuel cell temperature ($^{\circ}\text{K}$), $R = 8.3144621$ is the universal gas constant ($\text{J mol}^{-1} \text{K}^{-1}$), and p_{H_2} and p_{O_2} are unitless hydrogen and oxygen partial pressures in the anode and cathode, respectively, with respect to atmospheric pressure. Due to near atmospheric operation of the fuel cell, the oxygen partial pressure is $p_{O_2} = 0.21$; whereas, the hydrogen partial pressure p_{H_2} is considered as one of the measurable system states. It should be noted that the hydrogen partial pressure also depends on the generated water pressure and therefore, the assumption of a measurable hydrogen partial pressure might not always hold true and can potentially introduce errors in the voltage model. As it is shown in [33], such uncertainties in the model can be taken care of by an uncertainty estimator.

The Nernst equation describes the open-circuit voltage of the PEMFC; however, as soon as current is drawn from the fuel cell, the output fuel cell voltage will be

$$V_{FC}(t) = V_{oc}(t) - V_{act}(t) - V_{ohm}(t) - V_{conc}(t) \quad (2)$$

where V_{act} is the activation overvoltage (V), V_{ohm} is the ohmic overvoltage (V), and V_{conc} is the concentration overvoltage (V). As can be seen in [38], equations describing different voltage losses in a fuel cell can be complicated and might require the identification of numerous parameters; however, it is shown in [1] that some semi-

empirical control-oriented models can be used to accurately describe the fuel cell output voltage. The activation overvoltage, induced by the fuel cell reaction kinetics, is the amount of voltage that is lost in order to overcome the reaction energy barrier. It is typically described by the Butler-Volmer equation or the simpler Tafel equation; however, in this work, the following control-oriented model will be used [1]

$$V_{act}(t) = v_0(t) + v_a(t) \left(1 - e^{-c_1 i_{FC}(t)}\right) \quad (3)$$

where $i_{FC}(t) = I_{FC}(t)/A_{FC}$ is the current density (A cm⁻²), A_{FC} is the fuel cell active area (cm²), and

$$v_0(t) = a_1 + \frac{\Delta s}{2F} (T_{FC}(t) - T_{FC}^0) + a_2 T_{FC}(t) \quad (4)$$

$$v_a(t) = b_1 T_{FC}(t) + b_2 \quad (5)$$

where the constant coefficients a_1 , a_2 , b_1 , b_2 , and c_1 are identified empirically.

The ohmic overvoltage, which is due to resistance against charge transfer in the fuel cell, obeys Ohm's law of conduction and can be expressed by

$$V_{ohm}(t) = R_{ohm} i_{FC}(t) \quad (6)$$

where R_{ohm} is the ohmic resistance ($\Omega \cdot \text{cm}^2$). While the fuel cell ohmic resistance is attributed to electrolyte, electrodes, and interconnect resistances, it is mainly dominated by electrolyte conductivity against ionic charge transfer. Electrolyte conductivity strongly

depends on the water content in the electrolyte which, in turn, is a function of the fuel cell temperature. The models describing the relationship between temperature, humidity, and ionic conductivity are complex and require the identification of numerous model parameters. In this work, the ohmic resistance is approximated by a linear relationship with the temperature, similar to the model introduced in [40-41], as

$$R_{ohm}(t) = d_1 + d_2 T_{FC}(t) \quad (7)$$

where d_1 and d_2 are constant coefficients to be identified empirically.

Finally, the concentration overvoltage stems from voltage losses caused by poor mass transport in the supply and removal of reactants and products in the fuel cell. The concentration and mass transport losses depend mainly on the fuel cell geometry and mass transport properties. The concentration overvoltage is expressed by [1]

$$V_{conc}(t) = i_{FC}(t) (mi_{FC}(t))^n \quad (8)$$

where m and n are constant coefficients. More details on the voltage losses occurring inside the fuel cell can be found in [38]. By substituting for the voltage losses in Eq. (2) from Eqs. (3)-(8), and combining similar terms, the fuel cell voltage can be written as

$$V_{FC}(t) = a + \frac{RT_{FC}(t)}{2F} \left[\ln p_{H_2}(t) + \frac{1}{2} \ln p_{O_2}(t) \right] + bT_{FC}(t) + (cT_{FC}(t) + d) e^{-ei_{FC}(t)} - (f + gT_{FC}(t)) i_{FC}(t) - \left[i_{FC}(t) (mi_{FC}(t))^n \right] \quad (9)$$

The total fuel cell stack voltage is

$$V_{FC,st}(t) = N_{FC}V_{FC}(t) \quad (10)$$

where N_{FC} is the number of cells.

There are $N_{FC} = 40$ fuel cells in the experimental open-cathode fuel cell stack used in this paper. Furthermore, the fuel cell active area is $A_{FC} = 50 \text{ cm}^2$. Identification experiments were performed in order to obtain the other model parameters in Eq. (9). In these tests, the input PWM command to the fans was kept constant at 70% while the fuel cell current density increased from 0 to 0.28 A cm^{-2} , in 2 A steps. Using a constrained nonlinear least squares algorithm in Matlab's Optimization Toolbox, the model parameters are identified by fitting the experimental data. These parameters are $a = -4.6 \times 10^{-2}$, $b = 2.9 \times 10^{-3}$, $c = 5.41 \times 10^{-4}$, $d = -9.80 \times 10^{-3}$, $e = 514$, $f = -3.88$, $g = 4.90 \times 10^{-3}$, $m = 2.72 \times 10^{-7}$, and $n = -0.0760$.

Figure 3.1 shows the experimental voltage and the model output voltage in Eq. (10) as a function of the fuel cell current density. The experimental dataset shown in Figure 3.1 is a validation dataset obtained at 50% fan PWM command with current density steps of 300 s. The average output voltage in the last 120 s of each step was taken as the experimental voltage value corresponding to the specific current density in Figure 3.1. As seen in this figure, there is a good consistency between the measured and modeled voltage values with a Mean Average Percentage Error (MAPE) of 2.55%.

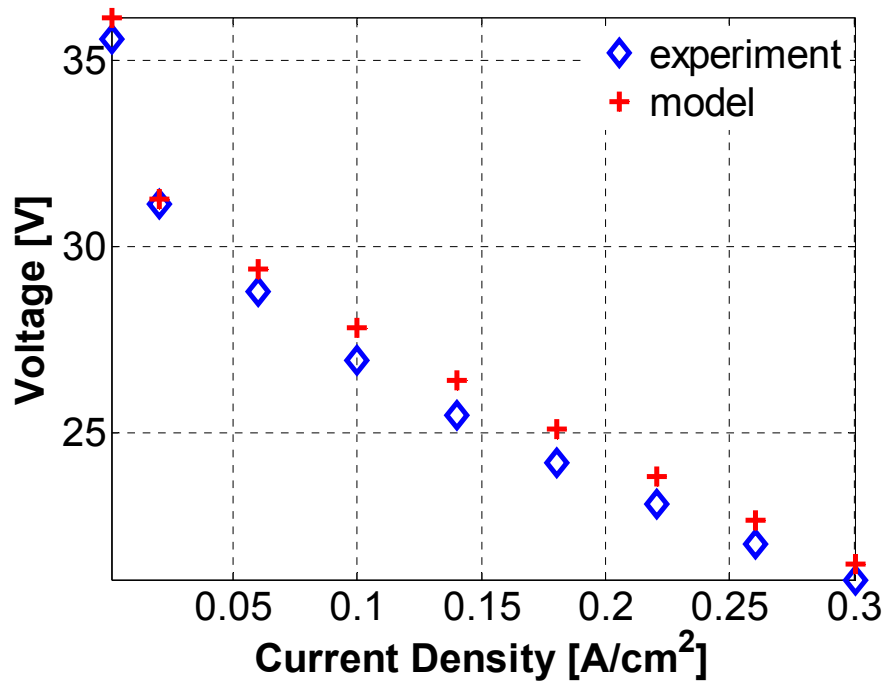


Figure 3.1. Experimental and model fuel cell voltages with 50% fan PWM command.

3.2. AIR DELIVERY SYSTEM DYNAMICS

In this section, the air-delivery subsystem for open-cathode fuel cells is analyzed. In open-cathode fuel cells, air-delivery is achieved using fans which pull the air through the cathode channels. In this section, fan dynamics will be discussed and an empirical model describing the relationship between the fan PWM command and rotational velocity will be developed.

3.2.1. Fan Operating Point Determination. In open-cathode PEMFCs, the pressure drop opposing the air flow in the air channels is [5]

$$\Delta p_{total}(t) = \frac{\rho v^2(t)}{2} \left(f_r \frac{l_c}{D_H} \right) + \frac{\rho v^2(t)}{2} (K_{L,entry} + K_{L,exit}) \quad (11)$$

where the first term describes the friction loss due to air flow along the cathode channels and the second term accounts for the minor losses at the entry and exit sections of the cathode. In Eq. (11) Δp_{total} is the total pressure drop (Pa), f_f is the friction factor, l_c is the channels' length (m), D_H is the hydraulic diameter (m), $\rho = 1.1839$ is the air density at Standard Temperature and Pressure (STP) (kg m^{-3}), and $v(t)$ is the air velocity (m s^{-1}). The parameters $K_{L,entry}$ and $K_{L,exit}$ are the minor loss coefficients at the cathode entry and exit, respectively, and can be approximated using tabulated values [42]

$$K_{L,entry} = 5.00 \times 10^{-2} \quad K_{L,exit} = 1.00 \quad (12)$$

The hydraulic diameter is

$$D_H = \frac{4(w_c h_c)}{2(w_c + h_c)} \quad (13)$$

where w_c and h_c are the channel width (m) and height (m), respectively.

In [5], Reynolds numbers below and above 500 are found to distinguish between laminar and transitional-turbulent flows, respectively, in open-cathode PEMFCs where the Reynolds number is

$$\text{Re}(t) = \frac{\rho v(t) D_H}{\mu} \quad (14)$$

where $\mu = 1.85 \times 10^{-5}$ is the air dynamic viscosity at STP ($\text{Pa}\cdot\text{s}$). For the laminar region, the following empirical equation is proposed for the friction factor [5]

$$f_r = \frac{1}{\text{Re}} \left[58.91 + 50.66 \exp\left(\frac{-3.4}{w_c/h_c}\right) \right] \quad (15)$$

For the turbulent region, the friction factor is empirically modeled as [5]

$$\frac{1}{\sqrt{f_r}} = -10 \log_{10} \left(0.218 + \frac{65.6}{\text{Re}(t) \sqrt{f_r}} \right) \quad (16)$$

The relationship between air velocity v (m s^{-1}) and air volumetric flow rate Q ($\text{m}^3 \text{s}^{-1}$) is

$$Q(t) = A_{Ca} v(t) \quad (17)$$

where A_{Ca} is the fuel cell cathode cross-sectional area (m^2). Using Eq. (17), the air mass-flow rate passing through the fuel cell stack is

$$\dot{m}_{air}(t) = \rho Q(t) \quad (18)$$

For a given fan, the performance curve illustrates the relationship between fan volumetric flow rate and pressure drop at the nominal rotational speed. In order to determine the fan operating point, its performance curve is intersected with the fuel cell pressure drop-air flow rate relationship. To this end, for a range of air flow rates, the corresponding air velocity is calculated via Eq. (17). The pressure drop is then computed as a function of air velocity using Eqs. (11)-(16). The intersection of the fan performance curve with the fuel cell pressure drop-air flow rate will result in the fan operating point. For other rotational speeds, the fan's operating flow rate is

$$Q_2(t) = \frac{Q_1}{\omega_1} \omega_2(t) \quad (19)$$

where ω_1 is the nominal fan speed (rpm), ω_2 is an arbitrary fan speed (rpm), Q_1 is the fan operating flow rate ($\text{m}^3 \text{s}^{-1}$), and Q_2 ($\text{m}^3 \text{s}^{-1}$) is the resulting flow rate corresponding to ω_2 (rpm).

3.2.2. Modeling Experimental Fuel Cell Fans. For the experimental system used for the studies in this paper, Table 3.1 summarizes the important fuel cell system physical parameters and their numerical values. The fans' performance curve and the fuel cell pressure drop-air flow rate curve are shown in Figure 3.2. Equations (15) and (16) are used to compute the friction factor in generating the fuel cell performance curve. Using the maximum air flow rate through the fans, i.e., $7.16 \times 10^{-2} \text{ m}^3 \text{ s}^{-1}$, the maximum Reynolds number that can be achieved is approximately 2200. Therefore, depending on the air velocity, air flow rate through the cathode channels can exhibit laminar or turbulent behavior. The intersection of the two curves is used in order to determine the fans' operating point, which is $\Delta p_{total} = 104 \text{ Pa}$ and $Q = 2.22 \text{ m}^3 \text{ min}^{-1}$. It is assumed that the fans' performance curve is expressed at the fan speed mentioned in the datasheet and Table 3.1. Therefore, for any given rotational speed, the air flow rate through the fans is calculated using Eq. (19) where $\omega_1 = 6000 \text{ rpm}$ is assumed to be the speed at which the performance curve is expressed and Q_1 is obtained from Figure 3.2.

Table 3.1. Experimental fuel cell system physical parameters

Parameter	Value
Cathode channel length, l_c	5.54×10^{-2} m
Cathode channel width, w_c	3.61×10^{-3} m
Cathode channel height, h_c	1.07×10^{-3} m
Cathode cross-sectional area, A_{Ca}	6.81×10^{-3} m ²
Performance curve fan speed, ω_1	6.00×10^3 rpm
Fan maximum air flow rate	7.16×10^{-2} m ³ s ⁻¹

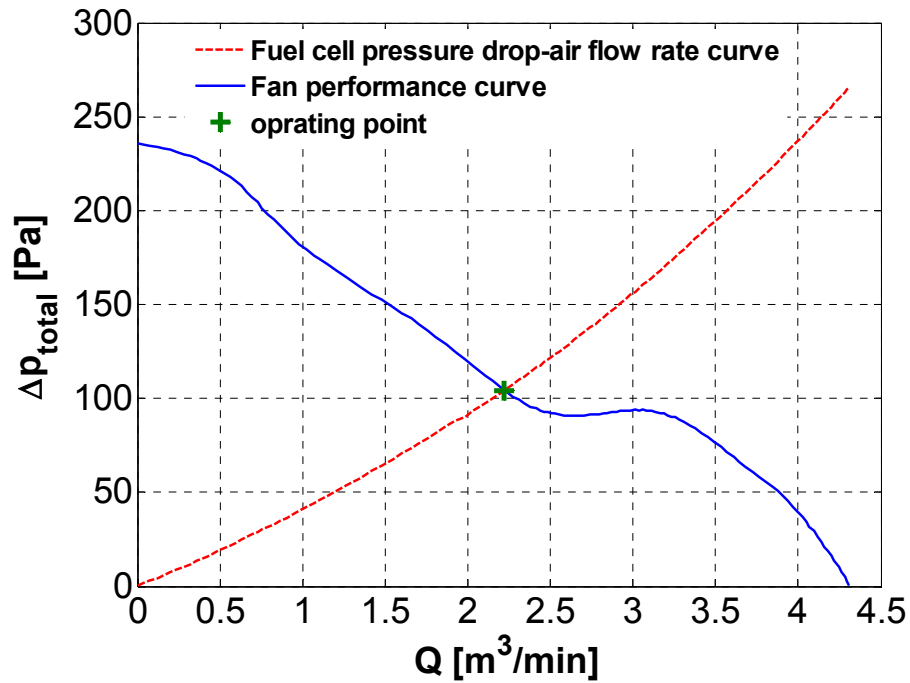


Figure 3.2. Fans' performance curve and fuel cell pressure drop-air flow rate curves.

A static model is used to express the relationship between the input PWM command to the fans and their rotational speed. This static model is identified with the least squares method using the experimental data. The experimental fan rotational

velocity, used for model identification, is obtained by step changes of 10% in the input PWM command. The model is

$$\omega(t) = 159.1u_{fan}(t) - 1211, \quad u_{fan,min} \leq u_{fan}(t) \leq u_{fan,max} \quad (20)$$

where u_{fan} is the PWM command to the fans (%), which has a lower threshold of $u_{fan,min} = 20\%$ and an upper threshold of $u_{fan,max} = 100\%$. The minimum threshold is taken so that the minimum air flow rate for the fuel cell reaction is provided. As shown in Figure 3.3, comparing the static model output in Eq. (20) versus validation data obtained by 15% increments in PWM command to the fans results in MAPE = 4.25%.

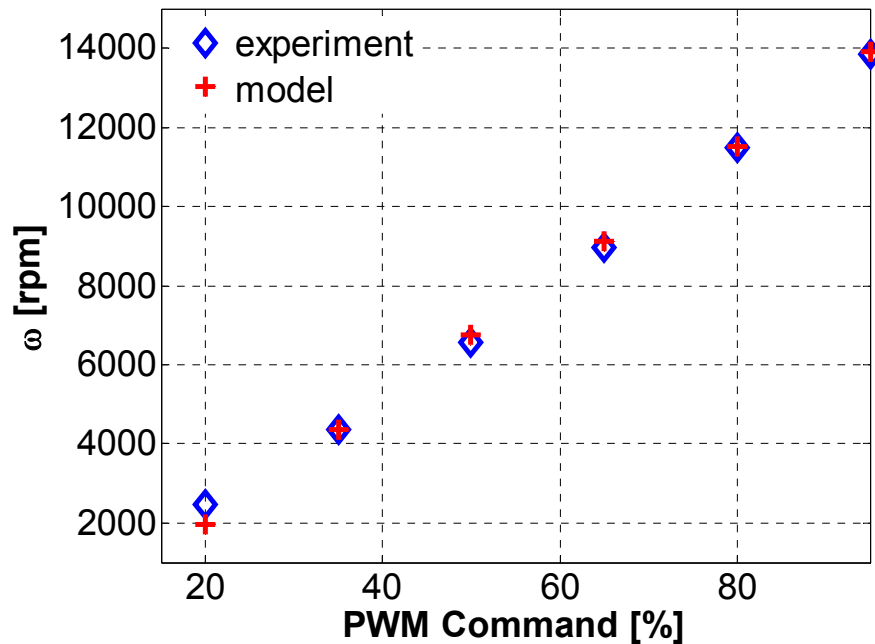


Figure 3.3. Validation results for fan rotational speed model versus experimental data.

3.3. TEMPERATURE

The temperature dynamics inside the open-cathode PEMFC stack is described using the following lumped-parameter energy balance

$$C_t \frac{dT_{FC}(t)}{dt} = P_{total}(t) - P_{FC}(t) - \dot{Q}_{coolant}(t) \quad (21)$$

where C_t is the thermal capacitance ($J \text{ } ^\circ K^{-1}$), T_{FC} is the fuel cell stack temperature ($^\circ K$), which is assumed to be the average temperature inside the fuel cell, P_{total} is the total power released by the electrochemical reactions (W), P_{FC} is the electrical power output (W), and $\dot{Q}_{coolant}$ is the heat lost due to cooling from the air flow (W). The total power released from the electrochemical reactions as a function of the hydrogen consumption rate, and therefore, the fuel cell current is

$$P_{total}(t) = \dot{M}_{H_2,used} \Delta H = \frac{N_{FC} I_{FC}(t)}{2F} \Delta H \quad (22)$$

where $\dot{M}_{H_2,used}$ is the used hydrogen molar flow rate (mol s^{-1}) and $\Delta H = 285.5 \times 10^3$ is the enthalpy change of hydrogen ($J \text{ mol}^{-1}$). The electrical output power is

$$P_{FC}(t) = V_{FC}(t) I_{FC}(t) \quad (23)$$

In open-cathode PEMFC systems, cooling is performed by the fans pulling air through the cathode. The amount of heat removed by the blown air is

$$\dot{Q}_{coolant}(t) = \eta_{fan} \dot{m}_{air}(t) c_p (T_{FC}(t) - T_{amb}) \quad (24)$$

where η_{fan} is the cooling efficiency, \dot{m}_{air} is the air mass-flow rate (kg s^{-1}), $c_p = 1006$ is specific heat coefficient of air ($\text{J kg}^{-1} \text{ }^\circ\text{K}^{-1}$), and T_{amb} is the ambient temperature ($^\circ\text{K}$).

The values of the cooling efficiency and thermal capacitance obtained by fitting the experimental data to the model in Eq. (21) are

$$C_t = 1.00 \times 10^3 \text{ JK}^{-1} \quad \text{and} \quad \eta_{fan} = 43.7\% \quad (25)$$

The same identification dataset used in the voltage modeling section is employed in order to obtain the parameters above. Figure 3.4 shows the modeled temperature using these parameters versus the validation dataset used in the voltage modeling section in which the fan PWM command was set to 50% and the current density was increased from 0.02 to 0.3 A cm^{-2} with 0.04 A cm^{-2} steps. As seen in this figure, there is a good consistency between the experimental temperature measurements and the modeled temperature, which results in an MAPE = 1.79%. It should be noted that the internal fuel cell temperature is a spatially distributed state inside the fuel cell and, as mentioned earlier, the experimental temperature measurements shown in Figure 3.4 are the average of ten temperature sensors placed evenly among the cathode channels. Therefore, the proposed model is capable of accurately describing the average internal fuel cell temperature.

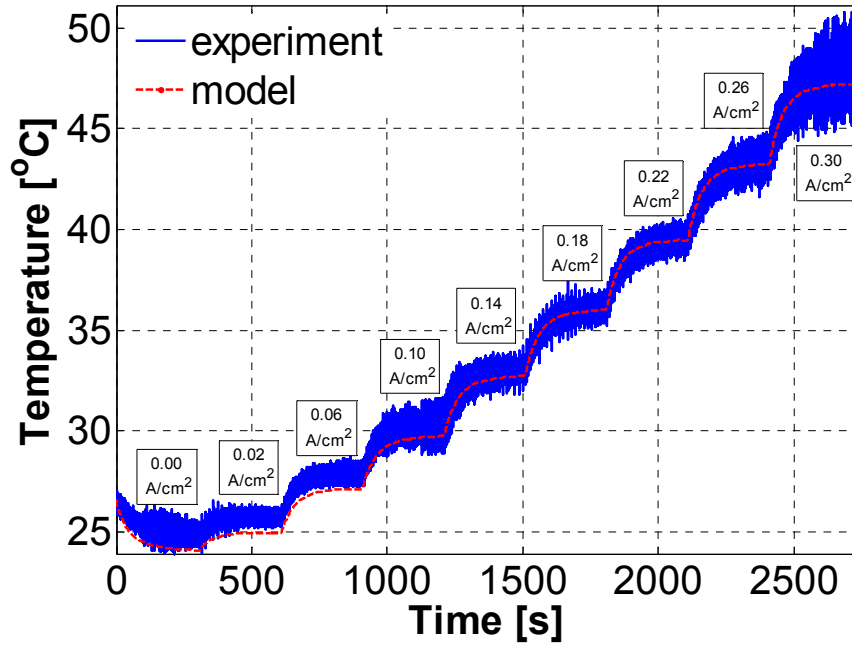


Figure 3.4. Experimental and model temperatures for step changes in current density.

3.4. PURGING

One of the advantages of dead-end fuel cells is that they will only consume as much hydrogen as required. The nominal hydrogen mass flow rate [38] is

$$\dot{m}_{H_2, nom} = N_{FC} \left(\dot{m}_{H_2, OCV} + M_{H_2} \frac{I_{FC}}{2F} \right) \quad (26)$$

where $\dot{m}_{H_2, OCV}$ is the hydrogen mass flow rate (g s^{-1}) required to generate the fuel cell open-circuit voltage and $M_{H_2} = 2$ is the hydrogen molar mass (g mol^{-1}).

In this section, based on purging tests performed on the experimental open-cathode fuel cell, empirical control-oriented models are developed that address the purging effects on the hydrogen pressure and mass flow rate dynamics. Purging is usually performed using a solenoid valve which is controlled by an on/off digital signal. It was

observed that the pressure and hydrogen mass-flow rate dynamics inside the anode channels are strongly dependent on the purge valve state. Depending on the solenoid valve state, the hydrogen pressure dynamics inside the anode channels can be expressed as

$$\frac{P_{H_2}(s)}{U(s)} = \begin{cases} \frac{p_{\text{tank}} - \Delta p_p}{\tau_{p_1}s + 1}, & \text{purge valve: open} \\ \frac{p_{\text{tank}}}{\tau_{p_2}s + 1}, & \text{purge valve: closed} \end{cases} \quad (27)$$

where $P_{H_2}(s)$ is the hydrogen pressure Laplace transform, $U(s)$ is the unit step function, p_{tank} is the hydrogen tank pressure (kPa), and Δp_p is the pressure drop during purging (kPa). Furthermore, τ_{p_1} and τ_{p_2} are the pressure dynamics empirical time constants (s) when the purge valve is open and closed, respectively. Finally, $p_{H_2}(0) = p_{\text{tank}}$ when the purge valve is open and $p_{H_2}(0) = p_{\text{tank}} - \Delta p_p$, when the purge valve is closed.

The hydrogen mass-flow rate inside the fuel cell is not only a function of the purge pulse, it also depends on the hydrogen pressure dynamics. Depending on the purge valve state, the hydrogen mass flow rate can be expressed as

$$\frac{\dot{M}_{H_2}(s)}{U(s)} = \begin{cases} \dot{m}_{H_2, \text{max}}, & \text{purge valve: open} \\ \frac{\dot{m}_{H_2, \text{nom}}}{\tau_{\dot{m}_{H_2}}s + 1} e^{-\tau_d s}, & \text{purge valve: closed} \end{cases} \quad (28)$$

where $\dot{M}_{H_2}(s)$ is the hydrogen mass flow rate Laplace transform, $\dot{m}_{H_2, \text{max}}$ is the maximum hydrogen mass flow rate (g s^{-1}) allowed by the mass-flow controller, $\dot{m}_{H_2, \text{nom}}$ is

given in Eq. (26), τ_d is the time delay (s) after which the mass flow rate reacts to the purge valve closing, and $\tau_{\dot{m}_{H_2}}$ is the mass flow rate empirical time constant (s) when the purge valve is closed. It should be noted that based on the experimental observations, the hydrogen mass flow rate and pressure dynamics' time constants, when the purge valve is closed, are equal, i.e. $\tau_{\dot{m}_{H_2}} = \tau_{p_2}$. Finally, the initial hydrogen mass flow rate when the purge valve closes is $\dot{m}_{H_2}(0) = \dot{m}_{H_2, \max}$.

In order to identify and validate the models in Eqs. (27) and (28), the dataset used for Figure 2.2 is employed. The hydrogen pressure and mass flow rate measurements at 35 °C are used for the model identification and the measurements at 40 and 45 °C are used for validation. The empirical parameters obtained during the identification process are $p_{tank} = 112$ kPa, $\Delta p_p = 21.9$ kPa, $\tau_{p_1} = 5.00 \times 10^{-2}$ s, $\tau_{p_2} = 9.51 \times 10^{-2}$ s, $\dot{m}_{H_2, \max} = 0.150$ g s⁻¹, $\dot{m}_{H_2, OCV} = 1.30 \times 10^{-3}$ g s⁻¹, and $\tau_d = 0.400$ s. Figure 3.5 shows the identification and validation results for the pressure and hydrogen mass flow rate models. The MAPEs between the model outputs and the experimental data shown in Figure 3.5 are presented in Table 3.2.

Table 3.2. MAPE of pressure and mass flow rate models for data in Figure 3.5.

	T = 35 °C	T = 40 °C	T = 45 °C
Pressure Model	0.439%	0.417%	0.417%
Mass Flow Rate Model	6.85%	11.5%	7.84%

The larger MAPE values for the hydrogen mass flow rate model are due to the constant mass flow rate assumption during purging. As can be seen in Figure 3.5 as soon as the purge valve opens the hydrogen flow exhibits an oscillatory response. This response is mainly due to the turbulent hydrogen flow during purging, which is not studied in this work. Finally, the control-oriented anode pressure and hydrogen mass flow rate models, presented in this section, can be used in future studies to design optimal purging strategies.

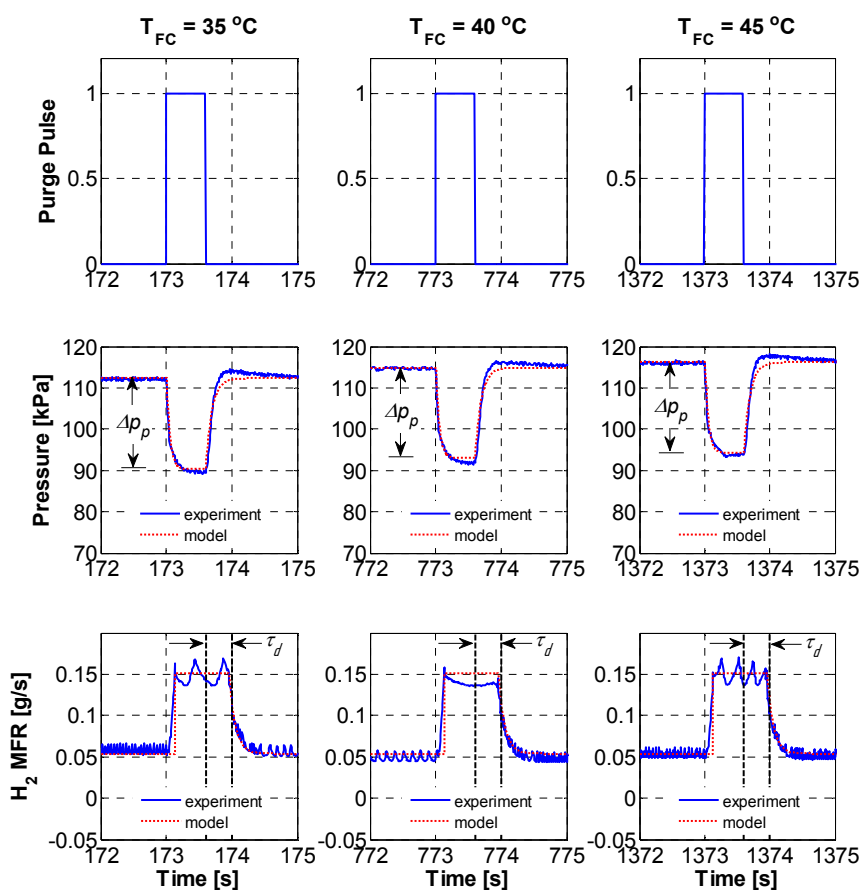


Figure 3.5. Anode pressure and hydrogen mass flow rate models versus experimental data during purge pulse.

4. SUMMARY AND CONCLUSIONS

Considering the numerous advantages of open-cathode fuel cells and their increasing use in low to medium power applications in recent years, rigorous studies are required to characterize their performance in order to design control methodologies capable of improving their efficiency and reliability, reducing their costs, and therefore, help with their widespread commercialization. To this end, this paper is specifically designated to provide a comprehensive understanding of the important aspects of open-cathode fuel cells operation and to develop models capable of describing their behavior. Performance characteristics such as humidity, purging, and temperature, were reviewed and then the temperature and purging effects were investigated experimentally. Furthermore, a set of nonlinear control-oriented models was proposed specifically for air-forced open-cathode fuel cells. The effectiveness of the proposed models to capture the coupled dynamics inside the fuel cell was validated experimentally. The framework provided in this paper can be used as a foundation for developing advanced control and estimation methodologies for open-cathode fuel cells. One of the important control challenges in open-cathode fuel cells, namely, voltage regulation was recently studied in another work by the authors based on the background provided in this paper.

REFERENCES

- [1] J.T. Pukrushpan, A.G. Stefanopoulou, and H. Peng, *Control of fuel cell power systems: Principles, modeling, analysis, and feedback design*, Springer, New York, 2004.
- [2] H. Su, L. Xu, H. Zhu, Y. Wu, L. Yang, S. Liao, H. Song, Z. Liang, and V. Birss, "Self-humidification of a PEM fuel cell using a novel Pt/SiO₂/C anode catalyst," *International Journal of Hydrogen Energy*, vol. 35, pp. 9110–9123, 2010.
- [3] S. Strahl, A. Husar, and J. Riera, "Experimental study of hydrogen purge effects on performance and efficiency of an open-cathode proton exchange membrane fuel cell system," *Journal of Power Sources*, vol. 248, pp. 474–482, 2014.
- [4] J. Zhang, Y. Tang, C. Song, X. Cheng, J. Zhang, and H. Wang, "PEM fuel cells operated at 0% relative humidity in the temperature range of 23–120 °C," *Electrochimica Acta*, vol. 52, pp. 5095–5101, 2007.
- [5] F. Barreras, A.M. Lopez, A. Lozano, and J.E. Barranco, "Experimental study of the pressure drop in the cathode side of air-forced open-cathode proton exchange membrane fuel cells," *International Journal of Hydrogen Energy*, vol. 36, pp. 7612–7620, 2011.
- [6] L. Zhang, D. Xu, and W.G. Hurley, "Modelling and simulation of a portable fuel cell system," *International Power Electronics and Motion Control Conference*, September 6–8, 2010, Ohrid, Macedonia.
- [7] T. Pokphet, W. Khan-ngern, and J. Charoensuk, "Effect of hydrogen purging period on system performance of PEMFC," *International Conference on Electrical Engineering/Electronics, Computer, Telecommunications and Information Technology*, May 19–21, 2010, Chiang Mai, Thailand.
- [8] J. Chen, J.B. Siegel, A.G. Stefanopoulou, and J.R. Waldecker, "Optimization of purge cycle for dead-ended anode fuel cell operation," *International Journal of Hydrogen Energy*, vol. 38, pp. 5092–5105, 2013.
- [9] J.T. Pukrushpan, A.G. Stefanopoulou, and H. Peng, "Control of fuel cell breathing," *IEEE Control Systems Magazine*, vol. 24, pp. 30–46, 2004.
- [10] B. Bidoggia and S.K. Kær, "Estimation of membrane hydration status for standby proton exchange membrane fuel cell systems by complex impedance measurement: Constant temperature stack characterization," *International Journal of Hydrogen Energy*, vol. 38, pp. 4054–4066, 2013.

- [11] B.A. McCain, A.G. Stefanopoulou, and I.V. Kolmanovsky, "On the dynamics and control of through-plane water distributions in PEM fuel cells," *Chemical Engineering Science*, vol. 63, pp. 4418–4432, 2008.
- [12] J.B. Siegel and A.G. Stefanopoulou, "Through the membrane and along the channel flooding in PEMFCs," *American Control Conference*, June 10–12, 2009, St. Louis, MO, USA.
- [13] J.B. Siegel and A.G. Stefanopoulou, "Parameterization of GDL liquid water front propagation and channel accumulation for anode purge scheduling in fuel cells," *American Control Conference*, June 30–July 2, 2010, Baltimore, MD, USA.
- [14] G. Ripaccioli, J.B. Siegel, A.G. Stefanopoulou, and S.D. Cairano, "Derivation and simulation results of a hybrid model predictive control for water purge scheduling in a fuel cell," *ASME Dynamic Systems and Control Conference*, October 12–14, 2009, Hollywood, CA, USA.
- [15] S. Strahl, A. Husar, and A.A. Franco, "Electrode structure effects on the performance of open-cathode proton exchange membrane fuel cells: A multiscale modeling approach," *International Journal of Hydrogen Energy*, vol. 39, pp. 9752–9767, 2014.
- [16] I.S. Hussaini and C.Y. Wang, "Dynamic water management of polymer electrolyte membrane fuel cells using intermittent RH control," *Journal of Power Sources*, vol. 195, pp. 3822–3829, 2010.
- [17] T.F. Fuller and J. Newman, "Water and thermal management in solid-polymer-electrolyte fuel cells," *Journal of the Electrochemical Society*, vol. 140, pp. 1218–1225, 1993.
- [18] P. Berg, K. Promislow, J. Pierre, J. Stumper, and B. Wetton, "Water management in PEM fuel cells," *Journal of the Electrochemical Society*, vol. 151, pp. 341–353, 2004.
- [19] T.V. Nguyen and M. Knobbe, "A liquid water management strategy for PEM fuel cell stacks," *Journal of Power Sources*, vol. 114, pp. 70–79, 2003.
- [20] A. Mokmeli and S. Asghari, "An investigation into the effect of anode purging on the fuel cell performance," *International Journal of Hydrogen Energy*, vol. 35, pp. 9276–9282, 2010.
- [21] E. Kimball, T. Whitaker, Y.G. Kevrekidis, and J.B. Benziger, "Drops, slugs, and flooding in polymer electrolyte membrane fuel cells," *AIChE Journal*, vol. 54, pp. 1313–1332, 2008.

- [22] W. Baumgartner, P. Parz, S. Fraser, E. Wallner, and V. Hacker, "Polarization study of a PEMFC with four reference electrodes at hydrogen starvation conditions," *Journal of Power Sources*, vol. 182, pp. 413–421, 2008.
- [23] L. Dumercy, M.-C. Pera, R. Glises, D. Hissel, S. Hamandi, F. Badin, and J.-M. Kauffmann, "PEFC stack operation in anodic dead end mode," *Fuel Cells*, vol. 4, pp. 352–357, 2004.
- [24] W. Na and B. Gou, "A thermal equivalent circuit for PEM fuel cell temperature control design," *IEEE International Symposium on Circuits and Systems*, May 18–21, 2008, Seattle, WA, USA.
- [25] P. Hu, G.-Y. Cao, X.-J. Zhu, and M. Hu, "Coolant circuit modeling and temperature fuzzy control of proton exchange membrane fuel cells," *International Journal of Hydrogen Energy*, vol. 35, pp. 9110–9123, 2010.
- [26] J.C. Amphlett, R.F. Mann, B.A. Peppley, P.R. Roberge, and A. Rodrigues, "A model predicting transient responses of proton exchange membrane fuel cells," *Journal of Power Sources*, vol. 61, pp. 183–188, 1996.
- [27] S. Strahl, A. Husar, P. Puleston, and J. Riera, "Performance improvement by temperature control of an open-cathode PEM fuel cell system," *Fuel Cells*, vol. 14, pp. 466–478, 2014.
- [28] R.T. Meyer and B. Yao, "Modeling and simulation of a modern PEM fuel cell system," *ASME International Conference on Fuel Cell Science, Engineering and Technology*, June 19–21, 2006, Irvine, CA, USA.
- [29] A.M. Lopez-Sabiron, J. Barroso, V. Roda, J. Barranco, A. Lozano, and F. Barreras, "Design and development of the cooling system of a 2 kW nominal power open-cathode polymer electrolyte fuel cell stack," *International Journal of Hydrogen Energy*, vol. 37, pp. 7289–7298, 2012.
- [30] F. Barreras, M. Maza, A. Lozano, S. Bascones, V. Roda, J.E. Barranco, M. Cerqueira, and A. Verges, "Design and development of a multipurpose utility AWD electric vehicle with a hybrid powertrain based on PEM fuel cells and batteries," *International Journal of Hydrogen Energy*, vol. 37, pp. 15367–15379, 2012.
- [31] T. Kurz and J. Keller, "Heat management in a portable high temperature PEM fuel cell module with open cathode," *Fuel Cells*, vol. 11, pp. 518–525, 2011.
- [32] J. Ishaku, N. Lotfi, H. Zomorodi, and R.G. Landers, "Control-oriented modeling for open-cathode fuel cell systems," *American Control Conference*, June 4–6, 2014, Portland, OR, USA.

- [33] N. Lotfi, H. Zomorodi, and R.G. Landers, "Thermal management and voltage stabilization in air-forced open-cathode fuel cells," *ASME Dynamic Systems and Control Conference*, October 28 – 30, 2015, Columbus, OH, USA.
- [34] M.H. Nehrir and C. Wang, *Modeling and control of fuel cells distributed generation applications*, Wiley–IEEE Press, New Jersey, 2009.
- [35] B. Gou, W. Na, and B. Diong, *Fuel cells: modelling, control, and applications*, CRC Press, Boca Raton, 2010.
- [36] S. Ahmed and P. Enjeti, "PEM fuel cell stack model development for real-time simulation applications," *IEEE Transactions on Industrial Electronics*, vol. 58, pp. 4217–4231, 2011.
- [37] J. Corrêa and F. Farret, "An electrochemical-based fuel-cell model suitable for electrical engineering automation approach," *IEEE Transactions on Industrial Electronics*, vol. 51, pp.1103–1112, 2004.
- [38] R.P. O'Hayre, S.-W. Cha, W. Colella, and F.B. Prinz, *Fuel cell fundamentals*, John Wiley and Sons, Inc., New York:, 2009.
- [39] J. Amphlett, R. Baumert, R. Mann, B. Peppley, and P. Roberge, "Performance modeling of the Ballard Mark IV solid polymer electrolyte fuel cell," *Journal of the Electrochemical Society*, vol. 142, pp. 9–15, 1995.
- [40] P. Pathapati, X. Xue, and J. Tang, "A new dynamic model for predicting transient phenomena in a PEM fuel cell system," *Renewable Energy*, vol. 30 pp. 1–22, 2005.
- [41] L. Tang, N. Lotfi, J. Ishaku, and R.G. Landers, Dynamic modeling and control of PEM fuel cell systems, in: S.E. Grasman, *Hydrogen energy and vehicle systems*, CRC Press, 2012, pp. 79–122.
- [42] R.W. Fox and A.T. McDonald, *Introduction to fluid mechanics*, John Wiley and Sons, Inc., New York, 1985.

IV. ACTIVE DISTURBANCE REJECTION CONTROL FOR VOLTAGE STABILIZATION IN OPEN-CATHODE FUEL CELLS THROUGH TEMPERATURE REGULATION

ABSTRACT

Temperature regulation is an important control challenge in open-cathode fuel cell systems. In this paper, a feedback controller, combined with a novel output-injection observer, is designed and implemented for fuel cell stack temperature control. The first functionality of the observer is to smooth the noisy temperature measurements. To this end, the observer gain is calculated based on Kalman filter theory which, in turn, results in a robust temperature estimation despite temperature model uncertainties and measurement noise. Furthermore, the observer is capable of estimating the output voltage model uncertainties. It is shown that temperature control not only ensures the fuel cell temperature reference is properly tracked, but, along with the uncertainty estimator, can also be used to stabilize the output voltage. Voltage regulation is of great importance for open-cathode fuel cells, which typically suffer from gradual voltage decay over time due to their dead-end anode operation. Moreover, voltage control ensures predictable and fixed fuel cell output voltages for given current values, even in the presence of disturbances. The observer stability is proved using Lyapunov theory, and the observer's effectiveness in combination with the controller is validated experimentally. The results show promising controller performances in regulating fuel cell temperature and voltage in the presence of model uncertainties and disturbances.

1. INTRODUCTION

While open-cathode Polymer Electrolyte Membrane Fuel Cells (PEMFCs) possess the advantages of closed-cathode PEMFCs, such as high efficiency and power density, long cell and stack life, low electrolyte corrosion, low noise levels, and low operating temperatures, they differ in that they have cathode channels exposed to the atmosphere. In closed-cathode PEMFCs, the air is supplied by a compressor at pressures from near ambient to approximately 6 atm. On the other hand, open-cathode PEMFCs are usually operated near atmospheric pressure with the air being supplied by either convection or low-power fans. Higher pressures in closed-cathode PEMFCs mandate simultaneous cathode and anode pressure regulation in order to minimize their pressure difference and avoid potential damage. However, in open-cathode PEMFC systems, due to near-atmospheric operating pressures, pressure regulation is not required. It should also be noted that although operating at higher pressures results in higher voltages, it induces considerable parasitic loads (e.g., compressor, cooling system, humidification system) and corresponding costs. However, open-cathode fuel cells do not require humidification and are usually supplied with dry reactants; therefore, open-cathode PEMFCs have become popular due to their portability and reduced number of required Balance-Of-Plant (BOP) components: compressors, supply or return manifolds, pumps and radiators for cooling, and humidifiers.

In spite of the numerous advantages of fuel cells, their safe, reliable, and efficient operation is still among the main challenges facing their widespread commercialization. The use of advanced and robust control methodologies capable of considering the complex interactions between different subsystems in fuel cells can greatly help

overcome these obstacles and ease their further development and employment. Open-cathode fuel cells, in particular, have not received much attention in the fuel cell literature. Due to their low cost, they are typically equipped with simple controllers which, in turn, results in their underutilization.

The majority of the papers on the control of PEMFCs focus on the challenges in closed-cathode PEMFC systems, specifically, their application in hybrid fuel cell-battery/supercapacitor systems and the optimization of the energy flow between different system components [1,2]. Another important control problem in closed-cathode fuel cells has been the cathode air flow management in order to prevent oxygen starvation and improve the overall system efficiency. Suh et al. [3] proposed a decentralized controller in order to minimize oxygen starvation by properly manipulating air flow. An explicit constrained model predictive controller was proposed in [4,5] for this purpose. Oxygen excess ratio i.e., the ratio of the supplied oxygen to the oxygen used in the fuel cell reaction, has been used as an indicator of the sufficiency of the oxygen supply [6]. A feedforward controller was developed in [7] in order to control the oxygen excess ratio, while the authors in [8,9] augmented the feedforward controller with a linear quadratic regulator structure for this purpose. Finally, the desired oxygen excess ratio was maintained using a nonlinear model-based controller in [10].

Other research in the closed-cathode PEMFC controls field has considered the minimization of fuel and consumed energy. In these studies, the hydrogen and/or oxygen flow rates are adjusted in such a way that minimum auxiliary and fuel consumption is achieved. Tekin et al. [11] used fuzzy logic in determining an air flow set-point in order to minimize energy consumption. In [12], air flow rate and output current were used as

control variables to minimize fuel consumption for different load demands. Air and hydrogen flow rate adjustments have also been employed for output voltage regulation. An adaptive air flow rate controller capable of the voltage regulation in the presence of plant uncertainties was developed in [13]. Furthermore, Wang et al. [14] used a multivariable H_∞ controller to regulate the output voltage by adjusting air and hydrogen flow rates.

Another important consideration for fuel cell performance is to maintain the stack temperature in a desired range. A PI controller was proposed in [15] for temperature regulation, whereas the authors in [16] achieved this objective by manipulating the coolant mass flow rate using a feedback linearization controller. Furthermore, an incremental fuzzy controller with integral action was proposed in [17]. In [18], a systematic approach was introduced to calculate the optimal temperature as a function of input air relative humidity and stoichiometry, which was then used as the temperature reference for the controller.

Although some of these works can readily be applied to open-cathode fuel cells, there are few studies specifically addressing their real-world control challenges. Strahl et al. [19] proposed an extremum seeking algorithm in order to determine the maximum voltage of an open-cathode fuel cell for a given current draw considering coupled temperature and humidity effects. The authors combined the extremum seeking algorithm with a PI controller in order to regulate the fuel cell voltage at its maximum value. Although the authors demonstrated promising simulation results, practical implementation of the proposed controller requires further investigation. A detailed procedure for the design and analysis of the cooling fans in a 2 kW air-forced open-

cathode fuel cell was presented in [20]. Also, Barreras et al. [21] proposed a non-model-based temperature control strategy for an open-cathode PEMFC used in a fuel cell hybrid vehicle. The controller adjusts the fans' speed to some predefined setpoints when the temperature exceeds a threshold.

Another important control challenge for open-cathode fuel cell systems is the design of purging strategies. Purging is mainly intended to remove excess water and other impurities in the anode channels, thereby maintain the desired humidity level. Purging is traditionally performed with a constant duration and period, as recommended by the fuel cell manufacturer. It can also be performed in a closed-loop manner using the fuel cell current as the feedback signal [22]. Recently, optimization strategies have been used in order to determine the optimal purging schedule based on its effect on the fuel cell active area, hydrogen consumption, voltage response and, therefore, the overall fuel cell system efficiency [23-25].

In this paper, temperature and voltage control, two of the important control problems in open-cathode fuel cells, will be investigated. Temperature has an important effect on fuel cell performance. Higher operating temperatures result in an increased fuel cell output voltage, larger voltage variations during purging, and even cathode catalyst layer drying in the case of extreme temperatures [26]. Therefore, a controller capable of dynamically maintaining the desired temperature, while considering model and process uncertainties, is required in order to ensure the fuel cell's desired performance. Temperature control in open-cathode fuel cells is typically handled in an open-loop fashion by running the fans continuously at a constant speed [27], which induces undesirable auxiliary power consumption. At lower current demands where increased

temperature is actually desirable, the fans can operate at lower speeds, thereby minimizing power consumption. However, a non-zero minimum fan speed is essential in order to guarantee the minimum air flow required to prevent oxygen starvation. In spite of the aforementioned advantages of operating open-cathode fuel cells at constant temperatures, a gradual voltage decrease over time is observed during this mode of operation. This phenomenon, along with the strong dependence of the fuel cell voltage on operating conditions, causes large voltage uncertainties for any given current draw; thereby increasing the complexity and cost of the required power electronics circuitry. In a previous work by authors [28], this issue was addressed by manipulating the temperature reference in order to maintain a constant output voltage. In this paper, this objective is achieved by augmenting a novel observer to the feedback temperature controller. The observer is capable of simultaneously estimating both the internal fuel cell temperature and the output voltage uncertainties. The observer stability is proved using Lyapunov stability and its effectiveness, as part of the control scheme, is shown experimentally. The proposed observer/controller set is robust against model uncertainties and ensures a fixed and predictable output fuel cell voltage as the operating conditions change. This feature can greatly simplify the design of open-cathode fuel cell systems and the power electronics to which they interface.

2. TEMPERATURE CONTROL

2.1. EXPERIMENTAL SYSTEM

The open-cathode fuel cell used in this work is a 500 W air-forced open-cathode PEMFC stack with 40 cells and an active area of 50 cm². The auxiliary components for the fuel cell stack include a hydrogen supply valve, a mass flow controller, a purge valve, two fans for combined air delivery and thermal management, and sensors for pressure, voltage, current, and internal and ambient temperature measurements. Details of the fuel cell stack and its auxiliary components can be found in [29]. Data acquisition and real-time control are achieved using two National Instruments cards. The multifunction card (NI-PCI 6225) is used for collecting sensor measurements and the analog output card (NI-PCI 6713) is used for supply and purge valve control and fan speed control. Supply and purge valve control are performed using digital signals; whereas, fan speed control is achieved using a Pulse Width Modulation (PWM) signal. The purge duration and period are chosen to be the manufacturer's original settings of 0.6 s and 15 s, respectively. The user interface with the National Instruments cards is created in Simulink using the Simulink Real-Time toolbox. The implemented code is executed on a target computer for real-time implementation with a sampling period of 100 ms.

2.2. CONTROLLER DESIGN

The internal temperature and voltage dynamics, respectively, can be written in compact form as [28]

$$\frac{dT_{FC}(t)}{dt} = l(I_{FC}(t), p_{H_2}(t), p_{O_2}, \dot{m}_{air}(t))T_{FC}(t) + h(I_{FC}(t), T_{amb}(t), \dot{m}_{air}(t)) \quad (1)$$

$$V_{FC}(t) = g(I_{FC}(t), p_{H_2}(t), p_{O_2})T_{FC}(t) + f(I_{FC}(t)) \quad (2)$$

where t is time (s), T_{FC} is the operating fuel cell temperature (K), I_{FC} is the fuel cell current (A), \dot{m}_{air} is the air mass-flow rate (kg s^{-1}), T_{amb} is the ambient temperature (K), and p_{H_2} and p_{O_2} are unitless hydrogen and oxygen partial pressures with respect to atmospheric pressure in the anode and cathode, respectively. Finally, the functions $f(\cdot)$, $g(\cdot)$, $h(\cdot)$, and $l(\cdot)$, respectively, are

$$\begin{aligned} f(\cdot) &= N_{FC} \left[a_1 + a_4 e^{-a_5 i_{FC}} - a_6 i_{FC} - \left(i_{FC} (a_8 i_{FC})^{a_9} \right) \right] \\ g(\cdot) &= N_{FC} \left[\frac{R}{2F} \left[\ln p_{H_2} + \frac{1}{2} \ln p_{O_2} \right] + a_2 + a_3 e^{-a_5 i_{FC}} - a_7 i_{FC} \right] \\ h(\cdot) &= \frac{1}{C_t} \left[\frac{N_{FC} \Delta H_{FC}(t)}{2F} - f(I_{FC}(t)) I_{FC}(t) + \eta_{fan} \dot{m}_{air}(t) c_p T_{amb}(t) \right] \\ l(\cdot) &= \frac{1}{C_t} \left[-g(I_{FC}(t), p_{H_2}(t), p_{O_2}) I_{FC}(t) - \eta_{fan} \dot{m}_{air}(t) c_p \right] \end{aligned} \quad (3)$$

where N_{FC} is the number of cells, $i_{FC}(t) = I_{FC}(t)/A_{FC}$ is the current density (A cm^{-2}), A_{FC} is the fuel cell active area (cm^2), $R = 8.3144621$ is the universal gas constant ($\text{J mol}^{-1} \text{K}^{-1}$), $F = 96485.34$ is Faraday's number (C mol^{-1}), C_t is the thermal capacitance (J K^{-1}), $\Delta H = 285.5 \times 10^3$ is the enthalpy change of hydrogen (J mol^{-1}), η_{fan} is the cooling efficiency, $c_p = 1006$ is specific heat coefficient of air ($\text{J kg}^{-1} \text{K}^{-1}$), and the coefficients a_1 , a_2 , a_3 , a_4 , a_5 , a_6 , a_7 , a_8 , and a_9 are identified experimentally [29].

In order to design the temperature controller, at each sampling time $t = t^*$, Eq. (1) is linearized about an equilibrium point $(\bar{T}_{FC}, \bar{\dot{m}}_{air})$, which can be obtained by solving

$$F(\bar{T}_{FC}, \bar{\dot{m}}_{air}) = l(I_{FC}(t^*), p_{H_2}(t^*), p_{O_2}, \bar{\dot{m}}_{air}(t^*))\bar{T}_{FC} + h(I_{FC}(t^*), T_{amb}(t^*), \bar{\dot{m}}_{air}(t^*)) = 0 \quad (4)$$

The temperature about which the linearization is performed is taken as the reference temperature $\bar{T}_{FC} = T_{FC,ref}(t^*)$. Therefore, using Eq. (4), the corresponding equilibrium air mass flow rate is

$$\bar{\dot{m}}_{air} = \frac{\frac{N_{FC}\Delta H}{2F} I_{FC}(t^*) - \left(f(I_{FC}(t^*)) + T_{FC,ref}(t^*) \cdot g(I_{FC}(t^*), p_{H_2}(t^*), p_{O_2}) \right) I_{FC}(t^*)}{\eta_{fan} c_p (T_{FC,ref}(t^*) - T_{amb}(t^*))} \quad (5)$$

Finally, the linearized temperature dynamics can be written as

$$\begin{aligned} \frac{d\delta T_{FC}(t)}{dt} &= \left[\frac{\partial F}{\partial T_{FC}}(t^*) \right]_{(\bar{T}_{FC}, \bar{\dot{m}}_{air})} \delta T_{FC}(t) + \left[\frac{\partial F}{\partial \dot{m}_{air}}(t^*) \right]_{(\bar{T}_{FC}, \bar{\dot{m}}_{air})} \delta \dot{m}_{air}(t) \\ &= \alpha \delta T_{FC}(t) + \beta \delta \dot{m}_{air}(t) \end{aligned} \quad (6)$$

where the incremental fuel cell temperature and incremental air mass flow rate, respectively, are $\delta T_{FC}(t) = T_{FC}(t) - \bar{T}_{FC}$ and $\delta \dot{m}_{air}(t) = \dot{m}_{air}(t) - \bar{\dot{m}}_{air}$. Using the state feedback control law

$$\delta \dot{m}_{air}(t) = \dot{m}_{air}(t) - \bar{\dot{m}}_{air} = -k_c \delta T_{FC}(t) \quad (7)$$

the linearized closed-loop system is

$$\frac{d\delta T_{FC}(t)}{dt} = [\alpha - \beta k_c] \delta T_{FC}(t) \quad (8)$$

If the gain k_c is chosen such that $\alpha - \beta k_c$ is negative, then the temperature closed-loop system is asymptotically and locally stable, the transient dynamics will be overdamped, and the settling time can be adjusted by manipulating k_c . Using Eq. (7), the air mass flow rate is

$$\dot{m}_{air}(t) = \bar{m}_{air} - k_c (T_{FC}(t) - \bar{T}_{FC}) \quad (9)$$

Finally, the actual control input, i.e., the input PWM command to the fans, is obtained using the empirical relationship [29]

$$u_{fan}(t) = \begin{cases} u_{fan,min}, & \dot{m}_{air}(t) \leq \dot{m}_{air,min} \\ \frac{1}{159.1} \left(\frac{\omega_1}{\rho Q_1} \dot{m}_{air}(t) + 1211 \right), & \dot{m}_{air,min} < \dot{m}_{air}(t) \leq \dot{m}_{air,max} \\ u_{fan,max}, & \dot{m}_{air}(t) > \dot{m}_{air,max} \end{cases} \quad (10)$$

where ω_1 (rpm) and Q_1 ($\text{m}^3 \text{s}^{-1}$) are the nominal fan rotational speed and air flow rate, respectively. Furthermore, the limits $\dot{m}_{air,min} = 0.0144 \text{ kg s}^{-1}$ and $\dot{m}_{air,max} = 0.108 \text{ kg s}^{-1}$ are obtained from the fans operating constraints, i.e., $u_{fan,min} = 20\%$ and $u_{fan,max} = 100\%$.

In order to investigate controller performance, a constant current density of 0.2 A cm^{-2} is drawn from the experimental fuel cell. The control objective for this test is to regulate the fuel cell temperature at 35, 40, and 45 °C. The controller gain k_c is obtained by linearizing the system at each time instant and solving the equation $\alpha - \beta k_c = -q$. The variable q is taken as 1 in order to guarantee closed-loop stability and generate a desirable

transient performance. Figure 2.1 shows the average fuel cell temperature, the fans' input duty cycle, and the fuel cell output voltage.

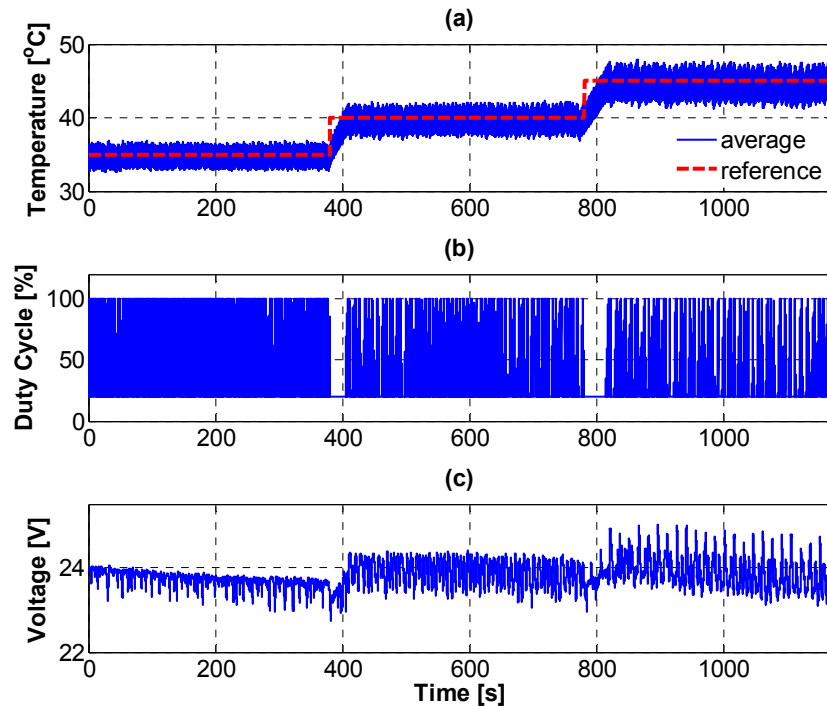


Figure 2.1. (a) Controlled average fuel cell temperature, (b) fan duty cycle, and (c) output voltage for $i_{FC} = 0.2 \text{ A cm}^{-2}$.

The temperature sensors are placed inside the cathode channels in order to measure the internal fuel cell temperature. The sensors' exposure to air flow, which is not smooth in the cathode channels, created by the fans' operation causes the measurement noise seen in Figure 2.1. Due to this noise, the control objective is achieved at the expense of continuous saturation of the control signal. In other words, the noisy nature of the temperature measurement, which is used as the feedback signal, causes the fans to start and stop continuously. This saturation can lead to long-term structural damage to the

fuel cell membrane and catalyst layers. Furthermore, as shown in subplot (c) of Figure 2.1, this behavior results in undesirable oscillations in the fuel cell output voltage.

2.3. OUTPUT-INJECTION OBSERVER DESIGN

In order to address the noisy temperature measurements and generate a smooth temperature estimate to use as the feedback signal in the controller, an output-injection observer is proposed in this subsection. To this end, the system dynamics in Eq. (1) are expressed in the state-space representation

$$\dot{x}(t) = l(u(t), \mathbf{d}(t))x + h(u(t), \mathbf{d}(t)) \quad (11)$$

where $x(t) = T_{FC}(t)$ is the system state, $u(t) = \dot{m}_{\text{air}}(t)$ is the control input which is assumed to be known, and the term $\mathbf{d}(t)$ is assumed to be the vector of measurable fuel cell system disturbances, i.e., $\mathbf{d}(t) = [T_{\text{amb}}(t) \quad I_{FC}(t) \quad p_{H_2}(t) \quad p_{O_2}]^T$. Finally, by defining the output vector as $\mathbf{y}(t) = [T_{FC}(t) \quad V_{FC}(t)]^T$, the output equation is

$$\mathbf{y}(t) = \mathbf{C}(t)x(t) + \mathbf{D}(t) \quad (12)$$

where the vectors $\mathbf{C}(t)$ and $\mathbf{D}(t)$, respectively, are

$$\mathbf{C}(t) = \begin{bmatrix} 1 \\ g(\mathbf{d}(t)) \end{bmatrix} \quad \mathbf{D}(t) = \begin{bmatrix} 0 \\ f(\mathbf{d}(t)) \end{bmatrix} \quad (13)$$

Considering significant uncertainty in the voltage model [28], it is assumed that the function $f(\cdot)$ can be written as $f(\mathbf{d}(t)) = f_1(\mathbf{d}(t)) + f_2(\mathbf{d}(t))$ where $f_1(\mathbf{d}(t))$ is the nominal part

of this function, expressed in Eq. (3), and $f_2(\mathbf{d}(t))$ is the unknown and unmolded part of Eq. (2). Therefore,

$$\mathbf{D}(t) = \underbrace{\begin{bmatrix} 0 \\ f_1(\mathbf{d}(t)) \end{bmatrix}}_{\mathbf{D}_1(t)} + \underbrace{\begin{bmatrix} 0 \\ f_2(\mathbf{d}(t)) \end{bmatrix}}_{\mathbf{D}_2(t)} \quad (14)$$

The following observer is then proposed for temperature estimation

$$\begin{aligned} \dot{\hat{x}}(t) &= l(u(t), \mathbf{d}(t))\hat{x}(t) + h(u(t), \mathbf{d}(t)) + \mathbf{K}(t)(\mathbf{y}(t) - \hat{\mathbf{y}}(t)) \\ \hat{\mathbf{y}}(t) &= \mathbf{C}(t)\hat{x}(t) + \mathbf{D}_1(t) + \hat{\mathbf{D}}_2(t) \end{aligned} \quad (15)$$

where $\hat{x}(t)$, $\hat{\mathbf{y}}(t)$, and $\hat{\mathbf{D}}_2(t)$ are estimates of the state, output, and output uncertainty, respectively, and $\mathbf{K}(t)$ is the observer gain. By defining the state and uncertainty estimation errors as $\tilde{x}(t) = x(t) - \hat{x}(t)$ and $\tilde{\mathbf{D}}_2(t) = \mathbf{D}_2(t) - \hat{\mathbf{D}}_2(t)$, respectively, the state estimation error system dynamics are

$$\begin{aligned} \dot{\tilde{x}}(t) &= l(u(t), \mathbf{d}(t))\tilde{x}(t) - \mathbf{K}(t)(\mathbf{C}(t)\tilde{x}(t) + \mathbf{D}_2(t) - \hat{\mathbf{D}}_2(t)) \\ &= (l(u(t), \mathbf{d}(t)) - \mathbf{K}(t)\mathbf{C}(t))\tilde{x}(t) - \mathbf{K}(t)\tilde{\mathbf{D}}_2(t) \end{aligned} \quad (16)$$

The observer gain $\mathbf{K}(t)$ is calculated based on Kalman filter theory to result in a smooth temperature estimate while being robust to model uncertainty and measurement noise [30]

$$\mathbf{K}(t) = p(t)\mathbf{C}^T(t)\mathbf{R}_c^{-1} \quad (17)$$

where \mathbf{R}_c is the measurement noise covariance matrix and $p(t)$ is the covariance which is propagated using

$$\dot{p}(t) = -(\mathbf{C}^T(t)\mathbf{R}_c^{-1}\mathbf{C}(t))p^2(t) + 2p(t)l(u(t), \mathbf{d}(t)) + q_c \quad (18)$$

where q_c is the standard deviation of the temperature model uncertainty. It should be mentioned that the measurement noise and temperature model uncertainty are assumed to be zero-mean Gaussian noises. At each sampling time, by substituting the input and disturbance measurements in Eqs. (17) and (18) to calculate for the observer gain $\mathbf{K}(t)$, a stable closed loop, i.e., $l(u(t), \mathbf{d}(t)) - \mathbf{K}(t)\mathbf{C}(t) < 0$ will be achieved.

The output equation uncertainty estimation error $\tilde{\mathbf{D}}_2(t)$ can be written as

$$\tilde{\mathbf{D}}_2(t) = \mathbf{D}_2(t) - \hat{\mathbf{D}}_2(t) = \begin{bmatrix} 0 \\ \tilde{f}_2(t) \end{bmatrix} \quad (19)$$

where $\tilde{f}_2(t) = f_2(t) - \hat{f}_2(t)$ is the estimation error of the uncertain function $f_2(t)$. It is assumed that this function can be approximated using a set basis functions $\boldsymbol{\phi}$ and a coefficient vector $\boldsymbol{\eta}$

$$f_2(t) = \boldsymbol{\eta}^T \boldsymbol{\phi}(\mathbf{d}(t)) \quad (20)$$

The basis functions can, in general, be polynomial functions of all of the measurable inputs to the output equation. While the order of the polynomials and therefore, number of the unknown coefficients, depend on the typical errors seen in the output model, higher-order polynomials result in higher approximation accuracies; however, the

implementation cost will also increase accordingly. The unknown coefficient vector $\boldsymbol{\eta}$ is estimated based on recursive least squares theory as

$$\hat{\boldsymbol{\eta}}(t) = \mathbf{S}(t)\boldsymbol{\varphi}(\mathbf{d}(t))\left[V_{FC}(t) - \hat{V}_{FC}(t)\right] \quad (21)$$

where $\hat{\boldsymbol{\eta}}(t)$ is the estimated coefficient vector and the matrix $\mathbf{S}(t)$ is the solution to the following differential equation

$$\dot{\mathbf{S}}(t) = \lambda\mathbf{S}(t) - \mathbf{S}(t)\boldsymbol{\varphi}(\mathbf{d}(t))\boldsymbol{\varphi}^T(\mathbf{d}(t))\mathbf{S}(t) \quad (22)$$

where λ is the forgetting factor. In order to investigate the stability of the proposed observer, the following candidate Lyapunov function is considered

$$V = \frac{1}{2}\gamma\tilde{x}^2(t) + \frac{1}{2}\tilde{\boldsymbol{\eta}}^T(t)\mathbf{S}^{-1}(t)\tilde{\boldsymbol{\eta}}(t) \quad (23)$$

where γ is a positive constant. By taking the time derivative of the Lyapunov function along the trajectories of the systems in Eqs. (16) and (21)

$$\begin{aligned} \dot{V} &= \gamma\tilde{x}(t)\dot{\tilde{x}}(t) - \tilde{\boldsymbol{\eta}}^T(t)\mathbf{S}^{-1}(t)\dot{\tilde{\boldsymbol{\eta}}}(t) + \frac{1}{2}\tilde{\boldsymbol{\eta}}^T(t)\frac{d}{dt}(\mathbf{S}^{-1}(t))\tilde{\boldsymbol{\eta}}(t) \\ &= \gamma\tilde{x}(t)\left((l(u(t), \mathbf{d}(t)) - \mathbf{K}(t)\mathbf{C}(t))\tilde{x}(t) - \mathbf{K}(t)\tilde{\mathbf{D}}_2(t)\right) \\ &\quad - \tilde{\boldsymbol{\eta}}^T(t)\mathbf{S}^{-1}(t)\left(\mathbf{S}(t)\boldsymbol{\varphi}(\mathbf{d}(t))\left[V_{FC}(t) - \hat{V}_{FC}(t)\right]\right) + \frac{1}{2}\tilde{\boldsymbol{\eta}}^T(t)\frac{d}{dt}(\mathbf{S}^{-1}(t))\tilde{\boldsymbol{\eta}}(t) \end{aligned} \quad (24)$$

As mentioned earlier, the observer gain $\mathbf{K}(t) = [k_1(t) \ k_2(t)]$, which is calculated using the Kalman filter formulation in Eqs. (17) and (18), results in a negative closed-

loop eigenvalue, denoted $l_c(t) = l(u(t), \mathbf{d}(t)) - \mathbf{K}(t)\mathbf{C}(t)$. Furthermore, by applying the matrix inversion lemma to Eq. (22)

$$\frac{d}{dt}(\mathbf{S}^{-1}(t)) = -\lambda \mathbf{S}^{-1}(t) + \boldsymbol{\varphi}(t)\boldsymbol{\varphi}^T(t) \quad (25)$$

Therefore, the Lyapunov function derivative in Eq. (24) can be written as

$$\begin{aligned} \dot{V} &= \gamma \tilde{x}(t) \left(l_c \tilde{x}(t) - k_2(t) \tilde{\boldsymbol{\eta}}^T(t) \boldsymbol{\varphi}(\mathbf{d}(t)) \right) - \tilde{\boldsymbol{\eta}}^T(t) \boldsymbol{\varphi}(\mathbf{d}(t)) g(t) \tilde{x}(t) \\ &\quad - \frac{\lambda}{2} \tilde{\boldsymbol{\eta}}^T(t) \mathbf{S}^{-1}(t) \tilde{\boldsymbol{\eta}}(t) - \frac{1}{2} \tilde{\boldsymbol{\eta}}^T(t) \boldsymbol{\varphi}(\mathbf{d}(t)) \boldsymbol{\varphi}^T(\mathbf{d}(t)) \tilde{\boldsymbol{\eta}}(t) \\ &\leq \gamma l_c \tilde{x}^2(t) - k_2 \gamma \tilde{\boldsymbol{\eta}}^T(t) \boldsymbol{\varphi}(\mathbf{d}(t)) \tilde{x}(t) - \tilde{\boldsymbol{\eta}}^T(t) \boldsymbol{\varphi}(\mathbf{d}(t)) g(t) \tilde{x}(t) \\ &\quad - \frac{1}{2} \tilde{\boldsymbol{\eta}}^T(t) \boldsymbol{\varphi}(\mathbf{d}(t)) \boldsymbol{\varphi}^T(\mathbf{d}(t)) \tilde{\boldsymbol{\eta}}(t) \end{aligned} \quad (26)$$

This inequality can be expressed in a more compact form

$$\dot{V} \leq - \begin{bmatrix} \tilde{x}(t) & \tilde{\boldsymbol{\eta}}^T(t) \end{bmatrix} \underbrace{\begin{bmatrix} -\gamma l_c & \frac{\boldsymbol{\varphi}^T(\mathbf{d}(t))}{2} (k_2(t)\gamma + g(t)) \\ \frac{\boldsymbol{\varphi}(\mathbf{d}(t))}{2} (k_2(t)\gamma + g(t)) & \frac{\boldsymbol{\varphi}(\mathbf{d}(t)) \boldsymbol{\varphi}^T(\mathbf{d}(t))}{2} \end{bmatrix}}_{\mathbf{Q}} \begin{bmatrix} \tilde{x}(t) \\ \tilde{\boldsymbol{\eta}}(t) \end{bmatrix} \quad (27)$$

By investigating the matrix \mathbf{Q} , it can be easily observed that by proper choice of the coefficient γ the matrix \mathbf{Q} will be positive-definite. Therefore, the Lyapunov function derivative is negative, implying asymptotic convergence of the estimation errors to zero. The observer performance in estimating the temperature is shown in the next subsection

in conjunction with the feedback controller. Furthermore, the estimated voltage model uncertainty will later be used in the voltage controller structure.

2.4. TEMPERATURE CONTROLLER PERFORMANCE

In this section, the temperature controller performance when using the estimated temperature from the observer is investigated. To this end, a current density of 0.2 A cm^{-2} is drawn from the fuel cell. Furthermore, the desired fuel cell reference temperature as shown in Figure 2.2 is similar to the test performed in Figure 2.1. The parameters tuned for the observer implementation are $p(0) = 100$, $q_c = 1$, $\mathbf{S}(0) = 100$, $\lambda = 0.95$, $\mathbf{R}_c = [1 \ 0; 0 \ 20]$. Furthermore, based on experimental investigations, it was observed that a scalar approximation was sufficient to capture the output model uncertainties.

The estimated and reference fuel cell temperatures are shown in Figure 2.2(a). As seen in this figure, the controller can closely track the desired reference temperature using the observer estimate in the feedback loop resulting in a Mean Average Percentage Error (MAPE) of 0.932% between the estimated and reference temperatures. The convergence speed is mainly limited by the fans' saturation limits. The fan input duty cycle is shown in Figure 2.2(b). As seen in this figure, the controller accomplishes its objective without frequent control signal saturation compared to when the observer is not utilized. However, when $T_{FC,ref} = 35 \text{ }^\circ\text{C}$ the fans operate near their full load in order to maintain the low reference temperature, resulting in excessive saturation of the PWM command signal. Finally, as seen in Figure 2.2(c), the fuel cell voltage is less noisy compared to the fuel cell voltage when implementing temperature control without the observer, as was shown in Figure 2.1(c). The oscillations seen in the voltage in this figure occur due to pressure variations during purging. Considering the previous test results with the

experimental fuel cell [28], this temperature-dependent phenomenon is considerably intensified, which can be attributed to the structural degradation and aging of the fuel cell.

A gradual voltage decrease over time can also be seen in Figures 2.1(c) and 2.2(c). This is due to the cathode catalyst layer drying, which typically occurs during the dead-end anode operation of the fuel cell. This slow phenomenon is a result of water evaporation and desorption in the cathode catalyst layer pores that cause a reduction in the active proton reaction sites and, therefore, voltage decline over time [26]. This behavior in the fuel cell output voltage will be compensated for by the voltage regulation scheme in the next section.

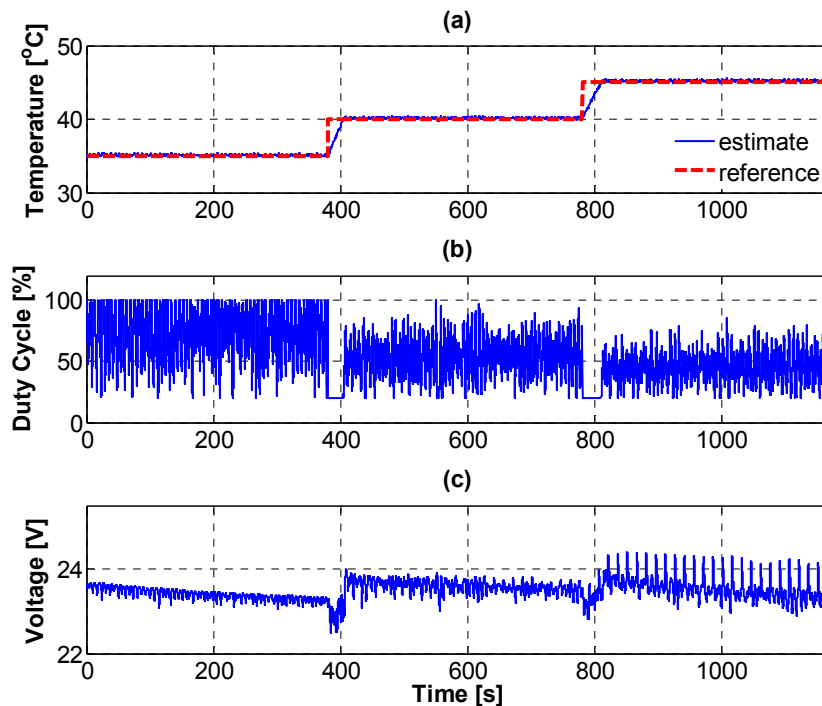


Figure 2.2. (a) Reference and estimated temperatures when using controller with temperature estimate from observer as feedback signal and corresponding (b) control signal and (c) output voltage.

The effect of the controller gain q (and therefore, k_c) on its performance is investigated using experimental data. To this end, for $i_{FC} = 0.2 \text{ A cm}^{-2}$, a reference temperature of $35 \text{ }^\circ\text{C}$ is set for the temperature controller. Figure 2.3 shows the steady state tracking errors and fan input duty cycle for two cases in which the controller gain, q is taken as 0.5 and 5. As seen in this figure, the controller gain of 0.5 (column (a)) results in an average absolute steady state error of $0.455 \text{ }^\circ\text{C}$, whereas this error is reduced to $0.122 \text{ }^\circ\text{C}$ (73.2% decrease) for the gain of 5 (column (b)). The MAPE values between the reference and estimated temperatures for gains of 0.5 and 5 are $0.147 \text{ }^\circ\text{C}$ and $0.0395 \text{ }^\circ\text{C}$, respectively. On the other hand, the controller gain of 0.5 results in a smoother control signal (40% peak-to-peak variations) compared to the gain of 5 (80% peak-to-peak

variations). Due to non-smooth fan operation for $q = 5$, there are more oscillations in the fuel cell temperature as seen in Figure 2.3. Therefore, a compromise needs to be made in choosing the controller gain. For the subsequent experiments in this paper, a gain of $q = 2$ is chosen for the temperature controller.

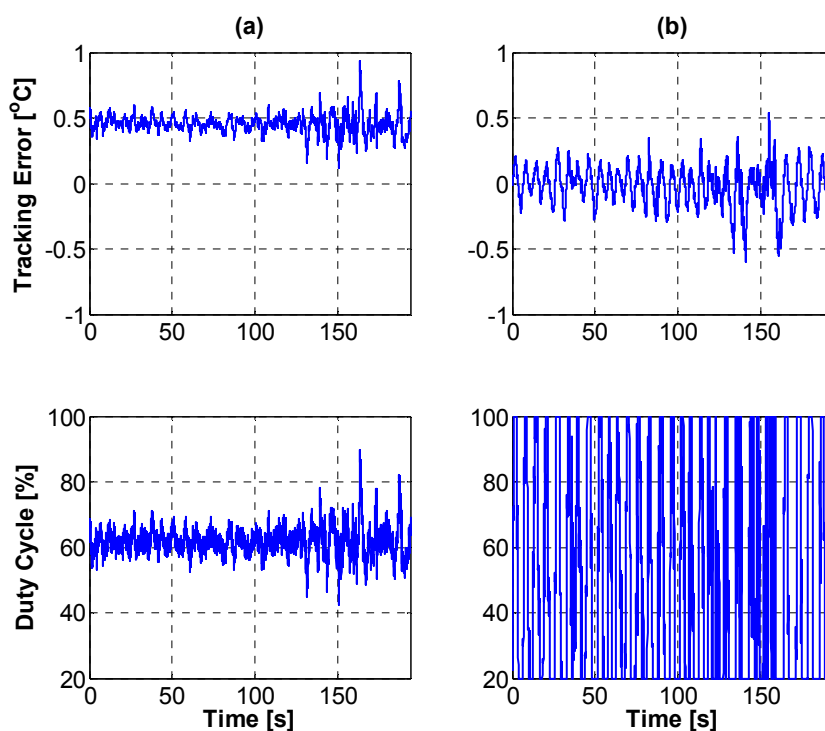


Figure 2.3. Temperature tracking error and duty cycle for $i_{FC} = 0.2 \text{ A cm}^{-2}$ and (a) $q = 0.5$ and (b) $q = 5$.

3. VOLTAGE CONTROL

As seen in Figures 2.1 and 2.2, constant temperature operation of the open-cathode fuel cell can result in a gradual voltage decrease over time. Furthermore, as various operating conditions in open-cathode fuel cells can cause a considerable amount of uncertainty in the fuel cell voltage, it is essential to maintain a fixed and predictable output voltage. Considering the voltage model in Eq. (2), voltage control can be achieved by manipulating its controllable inputs, i.e. hydrogen partial pressure, p_{H_2} and temperature, T_{FC} . The dead-end anode operation of the open-cathode fuel cells guarantees that they consume as much hydrogen as required. Therefore, as current densities change, the hydrogen mass flow rate is automatically adjusted to provide sufficient fuel for the fuel cell operation. Although increasing hydrogen mass flow rate can potentially be used to modulate the output voltage, this will be achieved at the cost of higher hydrogen consumption and added auxiliary components such as hydrogen mass flow controllers and pressure regulators. Therefore, in this section, voltage regulation is achieved by manipulating the reference fuel cell temperature.

Using the voltage model in Eq. (2), the temperature reference corresponding to a given voltage reference, $V_{FC,ref}$, is

$$T_{FC,ref}(t) = \frac{V_{FC,ref} - f(\mathbf{d}(t))}{g(\mathbf{d}(t))} = \frac{V_{FC,ref} - f_1(\mathbf{d}(t)) - f_2(\mathbf{d}(t))}{g(\mathbf{d}(t))} \quad (28)$$

As previously shown, the uncertain part of the voltage model, i.e., $f_2(\mathbf{d}(t))$ can be approximated by estimating the unknown coefficient vector $\hat{\boldsymbol{\eta}}(t)$ using the proposed

observer. By substituting the estimated uncertainty in Eq. (28), the temperature reference corresponding to $V_{FC,ref}$ can be calculated on-line using

$$T_{FC,ref}(t) = \frac{V_{FC,ref} - f_1(\mathbf{d}(t)) - \hat{\boldsymbol{\eta}}^T(t)\boldsymbol{\varphi}(\mathbf{d}(t))}{g(\mathbf{d}(t))} \quad (29)$$

Therefore, if the reference temperature in Eq. (29) is used as the input to the temperature controller, the fuel cell output voltage will approach the desired value, $V_{FC,ref}$. Figure 3.1 shows a block diagram of the voltage regulation scheme employed in this paper. As seen in this figure, fuel cell voltage, temperature, current, anode pressure, and input command to the fans are used as measurements for the voltage regulation scheme. The air mass flow rate passing through the cathode channels is obtained using the fan model. Any uncertainties in the temperature and fan model are accounted for in the observer design, whereas the voltage model uncertainties are accounted for using the estimated output uncertainty.

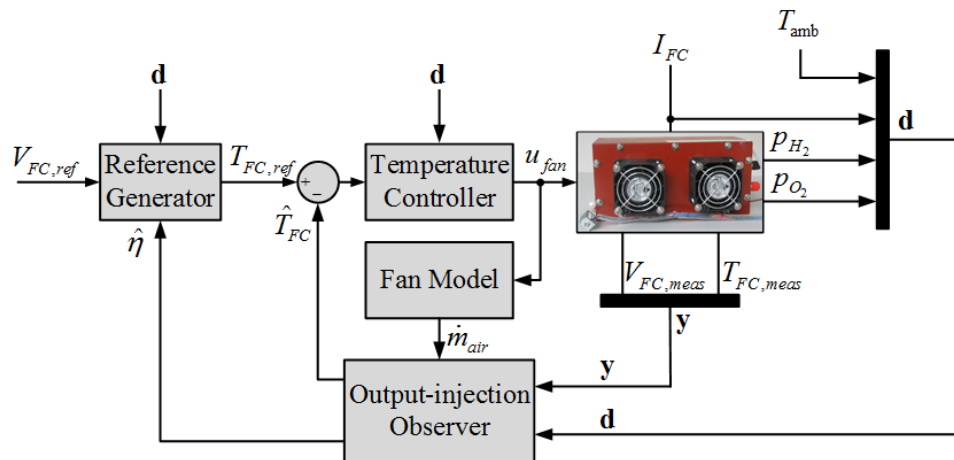


Figure 3.1. Fuel cell stack voltage regulation scheme.

Figure 3.2 shows the experimental results of a comparison between constant-temperature (column (a)) and constant-voltage (column (b)) operations of the open-cathode fuel cell system for $i_{FC} = 0.2 \text{ A cm}^{-2}$. In this figure, the measured and reference voltages, the estimated and reference temperatures, and the temperature tracking errors are shown. The desired constant voltage for the fuel cell operation corresponding to $i_{FC} = 0.2 \text{ A cm}^{-2}$ is taken to be 22.5 V, which is chosen in the fuel cell voltage range corresponding to $i_{FC} = 0.2 \text{ A cm}^{-2}$ as seen in Figure 2.2(c). Furthermore, the reference fuel cell temperature used in the constant-temperature operation is selected to be a typical operating temperature, in this case 35 °C. As seen in Figure 3.2, running the fuel cell solely in constant-temperature mode results in a decrease of approximately 4% in the output voltage within 2000 s. Moreover, as seen in this figure, the temperature controller is capable of closely tracking the reference temperature for both cases. The MAPEs between the estimated and reference temperatures for the constant-temperature and constant-voltage tests are 0.360% and 0.312%, respectively, which are within the temperature variations and less than 1.00% of the constant temperature reference. For the constant-voltage test, it can be seen that voltage regulation is achieved by gradually increasing the temperature controller reference signal resulting in a MAPE = 0.252%.

The voltage controller performance for $i_{FC} = 0.16, 0.22, \text{ and } 0.28 \text{ A cm}^{-2}$ is shown in Figure 3.3. The reference voltages corresponding to $i_{FC} = 0.16, 0.22, \text{ and } 0.28 \text{ A cm}^{-2}$ are 25.5, 23.0, and 20.5 V, respectively. These reference voltages for the given current densities are chosen based on the observed voltage measurements in the typical operating temperature range for the experimental open-cathode fuel cell used in this study. As seen in Figure 3.3(a), the controller is able to closely regulate the output fuel cell voltages at

the corresponding reference values with a MAPE = 1.27% between the measured and reference fuel cell voltages. In addition to steady-state voltage regulation, the transient fuel cell voltage is also properly controlled by the proposed controller as seen in Figure 3.3. In other words, the fast temperature effect on the fuel cell voltage dominates the slower transient effects due to current density changes and, consequently, the controller manages to regulate the voltage at its steady state value in about 60 s for a current density change from 0.16 to 0.22 A cm⁻² and in about 35 s for a current density change from 0.22 to 0.28 A cm⁻². The reason for the change in the transient response is that the controller has fixed gains, while the operating condition varied to a degree where the system dynamics changed appreciably. However, the time constant of the voltage dynamics due to current density changes without the controller is between 100 and 200 s. Furthermore, Figure 3.3(b) shows the reference and estimated fuel cell temperatures and the tracking error, which has a MAPE = 0.797%. Again, the reference temperature is being increased by the voltage controller in order to overcome the voltage drop and facilitate voltage regulation. As seen in Figure 3.3, the fuel cell voltage for $i_{FC} = 0.28$ A cm⁻² exhibits a non-smooth behavior in the form of oscillations with a magnitude of approximately 1.8 V. In addition to the aforementioned aging of the experimental fuel cell, this phenomenon is also due to estimation errors in the output equation uncertainty. From the voltage measurements in Figures 2.1 and 2.2, it can be observed that there is a significant variation between the fuel cell voltage behavior during purging at different temperatures. The control-oriented voltage model in Eq. (2), especially, the function $g(\cdot)$ is not capable of capturing this effect. Therefore, the proposed estimation methodology fails to correctly identify the output equation uncertainties. The uncertainties in the function $g(\cdot)$ also

contribute to the errors in reference temperature determination in Eq. (29). Incorporating control-oriented models capable of describing the effect of this phenomenon on the fuel cell voltage can significantly improve the performance of the proposed observer and therefore, voltage regulation scheme. This modeling work is currently under development.

In order to investigate the limitations of the proposed voltage controller, two tests have been performed as shown in Figure 3.4. In the first test (column a), a voltage reference of 22.5 V is chosen corresponding to $i_{FC} = 0.2 \text{ A cm}^{-2}$; whereas, in the second test (column b), a higher voltage reference of 23.5 V is selected for the same current density. In column (a) of Figure 3.4, the fuel cell voltage and temperature for the first test are shown. As seen in these subplots, in order to facilitate voltage regulation, the reference temperature increases gradually from 31.7 °C to about 36.6 °C in approximately 27 min and remains constant afterwards. On the other hand, for $V_{FC,ref} = 23.5 \text{ V}$, the fuel cell reference temperature rise is much faster as can be seen in column (b) of Figure 3.4 and, as soon as the temperature reaches approximately 52 °C, the voltage starts to drop due to intensified cathode catalyst layer drying. After reaching 55 °C, the temperature stops increasing; however, the fuel cell voltage keeps dropping. One possible solution to this problem is to alternatively switch between voltage and temperature control. In other words, as soon as the reference temperature for the voltage controller reaches a temperature where the voltage starts decreasing, the controller should regulate the temperature at a lower setpoint. This would result in an increase in the dropping fuel cell voltage until it reaches the original voltage reference at which point the

controller will switch back to voltage control. This algorithm is currently under development by the authors.

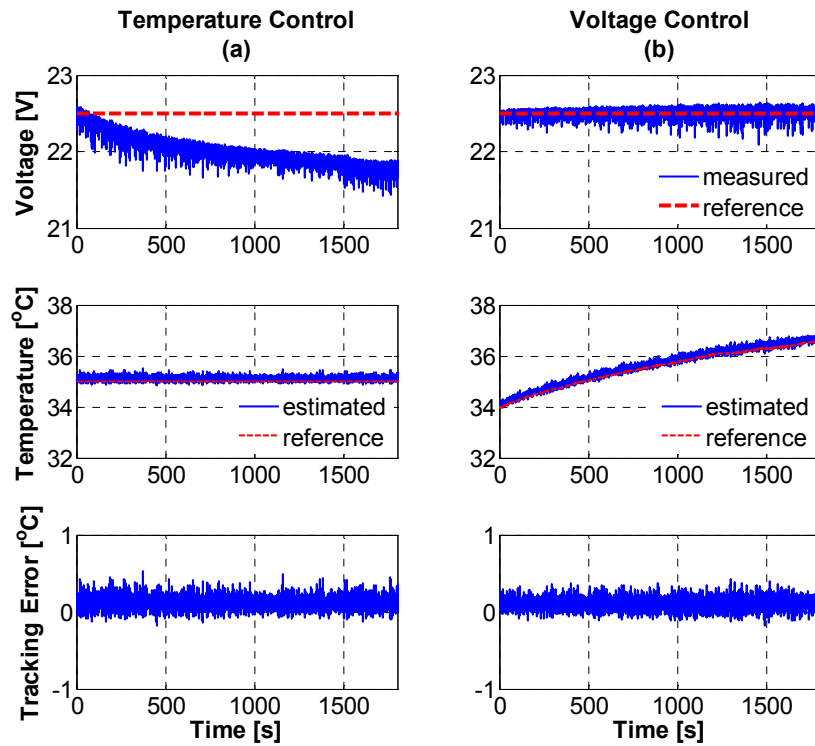


Figure 3.2. Measured and reference voltages, estimated and reference temperatures, and temperature tracking error for (a) constant-temperature and (b) constant-voltage fuel cell operations.

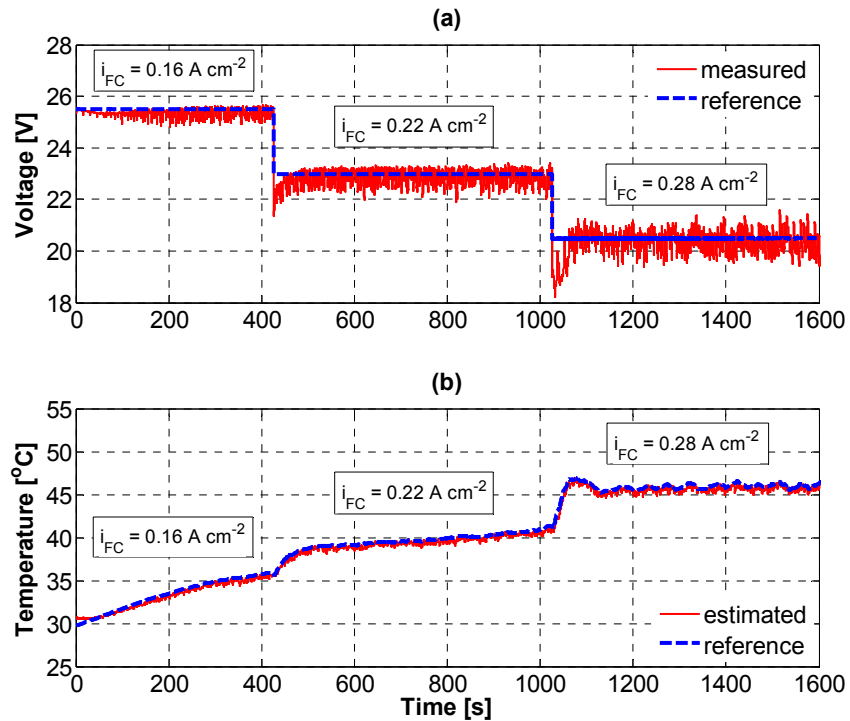


Figure 3.3. Reference and measured (a) fuel cell voltage and (b) temperature for voltage regulation experiments.

In summary, by properly choosing a voltage reference in the typical operating range for a given current density, the proposed voltage controller can guarantee a fixed polarization curve for the fuel cell and eliminate voltage model uncertainties. This polarization curve could be determined at the design stage. Any uncertainty in this polarization curve during the lifetime of the fuel cell would be compensated for by the voltage controller. Thus, the voltage controller can not only be used to compensate for the gradual voltage decrease, it can also be used to ensure a predictable output voltage for each current demand.

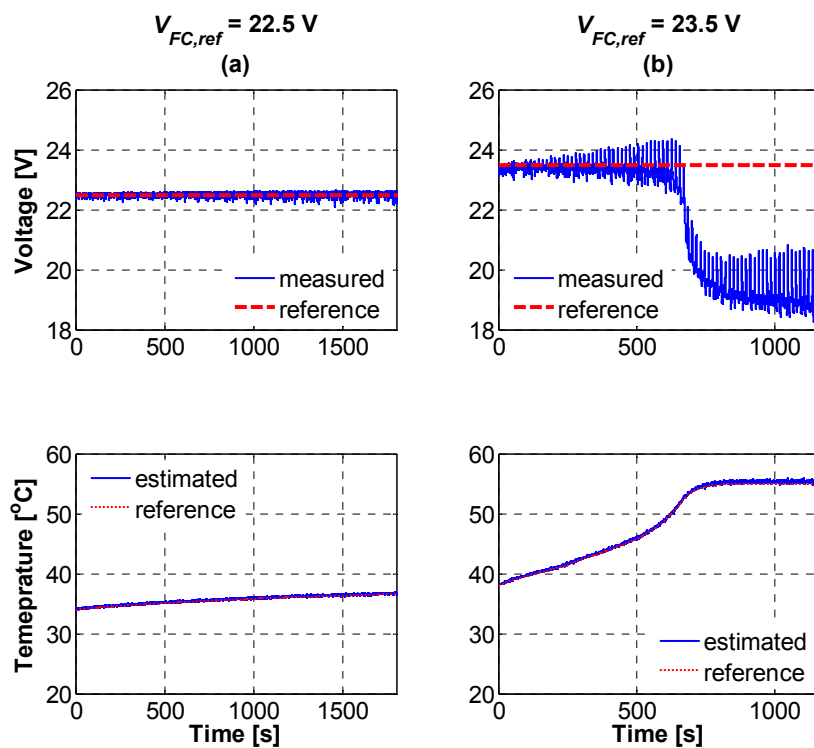


Figure 3.4. Fuel cell voltage and temperature for voltage regulation at (a) $V_{FC,ref} = 22.5$ V and (b) $V_{FC,ref} = 23.5$ V.

4. SUMMARY AND CONCLUSIONS

In this paper, temperature and voltage control problems in air-forced open-cathode fuel cells were formulated and solved for a laboratory fuel cell system. The temperature controller was shown to be able to accurately maintain the fuel cell temperature for constant and time-varying references. Also, the voltage controller was shown to result in a constant output voltage for constant current draws, and was able to improve the transient voltage response during current density changes. Finally, the performance of the proposed controller strongly depends on the selected voltage reference. While lower voltage references exhibit a stable performance, higher voltage set points can result in a faster temperature rise and, therefore, the possibility of reaching high temperatures which will, in turn, result in performance degradation. Future work will include incorporating adaptation into the controller to reduce voltage oscillations at high power demands and maintain the reference fuel cell voltage if the reference temperature reaches the system temperature limits by using a switching controller. The use of the voltage controller can eliminate undesirable uncertainty in the fuel cell output voltage, resulting in a fixed pre-determined polarization curve and simplifying the design of the interfacing power electronics circuitry.

REFERENCES

- [1] W. Greenwell and A. Vahidi, "Predictive control of voltage and current in a fuel cell-ultracapacitor hybrid," *IEEE Transactions on Industrial Electronics*, vol. 57, pp. 1954–1963, 2010.
- [2] Z. Jiang and R. Dougal, "A compact digitally controlled fuel cell/battery hybrid power source," *IEEE Transactions on Industrial Electronics*, vol. 53, pp. 1094–1104, 2006.
- [3] K.-W. Suh and A.G. Stefanopoulou, "Effects of control strategy and calibration on hybridization level and fuel economy in fuel cell hybrid electric vehicle," *SAE Technical Paper*, 2006.
- [4] A. Arce and D. Ramirez, "Constrained explicit predictive control strategies for PEM fuel cell system," *IEEE Conference on Decision and Control*, December 12–14, 2007, New Orleans, LA, USA.
- [5] A. Arce, A.J. Real, C. Bordons, and D.R. Ramírez, "Real-time implementation of a constrained MPC for efficient airflow control in a PEM fuel cell," *IEEE Transactions on Industrial Electronics*, vol. 57, pp. 1892–1905, 2010.
- [6] J.T. Pukrushpan, H. Peng, and A.G. Stefanopoulou, "Control-oriented modeling and analysis for automotive fuel cell systems," *Journal of Dynamic Systems, Measurement, and Control*, vol. 126, pp. 14–25, 2004.
- [7] M. Grujicic, K.M. Chittajallu, E.H. Law, and J.T. Pukrushpan, "Model-based control strategies in the dynamic interaction of air supply and fuel cell," *Journal of Power and Energy*, vol. 218A, pp. 487–499, 2004.
- [8] J.T. Pukrushpan, A.G. Stefanopoulou, and H. Peng, "Modeling and control for PEM fuel cell stack system," *American Control Conference*, May 8–10, 2002, Anchorage, AK, USA.
- [9] J.T. Pukrushpan, A.G. Stefanopoulou, and H. Peng, "Control of fuel cell breathing," *IEEE Control Systems Magazine*, vol. 24, pp. 30–46, 2004.
- [10] M.A. Danzer, J. Wilhelm, H. Aschemann, and E.P. Hofer, "Model-based control of cathode pressure and oxygen excess ratio of a PEM fuel cell system," *Journal of Power Sources*, vol. 176, pp. 515–522, 2008.
- [11] M. Tekin, D. Hissel, M.-C. Pera, and J.-M. Kauffmann, "Energy consumption reduction of a PEM fuel cell motor-compressor group thanks to efficient control laws," *Journal of Power Sources*, vol. 156, pp. 57–63, 2006.

- [12] C.A. Ramos-paja, C. Bordons, A. Romero, R. Giral, and L. Martínez-salamero, "Minimum fuel consumption strategy for PEM fuel cells," *IEEE Transactions on Industrial Electronics*, vol. 56, pp. 685–696, 2009.
- [13] Y.-P. Yang, F.-C. Wang, H.-P. Chang, Y.-W. Ma, and B.-J. Weng, "Low power proton exchange membrane fuel cell system identification and adaptive control," *Journal of Power Sources*, vol. 164, pp. 761–771, 2007.
- [14] F.-C. Wang, H.-T. Chen, Y.-P. Yang, and J.-Y. Yen, "Multivariable robust control of a proton exchange membrane fuel cell system," *Journal of Power Sources*, vol. 177, pp. 393–403, 2008.
- [15] S. Choe and J. Ahn, "Dynamic simulator for a PEM fuel cell system with a PWM DC/DC converter," *IEEE Transactions on Energy Conversion*, vol. 23, pp. 669–680, 2008.
- [16] J.R. Kolodziej, "Thermal dynamic modeling and nonlinear control of a proton exchange membrane fuel cell stack," *Journal of Fuel Cell Science and Technology*, vol. 4, pp. 255–260, 2007.
- [17] P. Hu, G.-Y. Cao, X.-J. Zhu, and M. Hu, "Coolant circuit modeling and temperature fuzzy control of proton exchange membrane fuel cells," *International Journal of Hydrogen Energy*, vol. 35, pp. 9110–9123, 2010.
- [18] L.A.M. Riascos and D.D. Pereira, "Optimal temperature control in PEM fuel cells," *IEEE Industrial Electronics Conference*, November 3–5, 2009, Porto, Portugal.
- [19] S. Strahl, A. Husar, P. Puleston, and J. Riera, "Performance improvement by temperature control of an open-cathode PEM fuel cell system," *Fuel Cell*, vol. 3, pp. 466–478, 2014.
- [20] A.M. Lopez-Sabiron, J. Barroso, V. Roda, J. Barranco, A. Lozano, and F. Barreras, "Design and development of the cooling system of a 2 kW nominal power open-cathode polymer electrolyte fuel cell stack," *International Journal of Hydrogen Energy*, vol. 37, pp. 7289–7298, 2012.
- [21] F. Barreras, M. Maza, A. Lozano, S. Bascones, V. Roda, J.E. Barranco, M. Cerqueira, and A. Verges, "Design and development of a multipurpose utility AWD electric vehicle with a hybrid powertrain based on PEM fuel cells and batteries," *International Journal of Hydrogen Energy*, vol. 37, pp. 15367–15379, 2012.
- [22] A. Mokmeli and S. Asghari, "An investigation into the effect of anode purging on the fuel cell performance," *International Journal of Hydrogen Energy*, vol. 35, pp. 9276–9282, 2010.

- [23] T. Pokphet, W. Khan-ngern, and J. Charoensuk, "Effect of hydrogen purging period on system performance of PEMFC," *International Conference on Electrical Engineering/Electronics, Computer, Telecommunications and Information Technology*, May 19–21, 2010, Chiang Mai, Thailand.
- [24] J. Chen, J.B. Siegel, A.G. Stefanopoulou, and J.R. Waldecker, "Optimization of purge cycle for dead-ended anode fuel cell operation," *International Journal of Hydrogen Energy*, vol. 38, pp. 5092–5105, 2013.
- [25] G. Ripaccioli, J.B. Siegel, A.G. Stefanopoulou, and S.D. Cairano, "Derivation and simulation results of a hybrid model predictive control for water purge scheduling in a fuel cell," *ASME Dynamic Systems and Control Conference*, October 12–14, 2009, Hollywood, CA, USA.
- [26] S. Strahl, A. Husar, and A.A. Franco, "Electrode structure effects on the performance of open-cathode proton exchange membrane fuel cells: A multiscale modeling approach," *International Journal of Hydrogen Energy*, vol. 39, pp. 9752–9767, 2014.
- [27] M. Matian, A. Marquis, and N. Brandon, "Model based design and test of cooling plates for an air-cooled polymer electrolyte fuel cell stack," *International Journal of Hydrogen Energy*, vol. 36, pp. 6051–6066, 2011.
- [28] N. Lotfi, H. Zomorodi, and R.G. Landers, "Thermal management and voltage stabilization in air-forced open-cathode fuel cells," *Dynamic Systems and Control Conference*, October 28–30, 2015, Columbus, OH, USA.
- [29] J. Ishaku, N. Lotfi, H. Zomorodi, R.G. Landers, "Control-oriented modeling for open-cathode fuel cell systems," *American Control Conference*, June 4–6, 2014, Portland, OR, USA.
- [30] D. Simon, *Optimal state estimation: Kalman, H infinity, and nonlinear approaches*, John Wiley and Sons, New Jersey, 2006.

SECTION

2. SUMMARY, CONCLUSIONS, AND FUTURE WORK

This dissertation provides a foundation for the characterization, performance analysis, and modeling of Li-ion batteries and open-cathode PEM fuel cells with the ultimate goal of designing control methodologies to improve their performance and reduce their costs and help with their widespread commercialization. Some of the most important control problems, namely temperature control and voltage stabilization in open-cathode PEM fuel cells and SOC estimation in Li-ion batteries, are formulated and solved based on a novel estimation approach that is proposed in this dissertation. A summary of the individual papers in the dissertation along with the future research directions are presented in the following subsections:

2.1. SUMMARY AND CONCLUSIONS

In Paper I, the development of an experimental Li-ion battery research testbed is presented. After a detailed description of design considerations and system development, battery characterization and modeling are studied, and some of the essential functionalities of BMSs are reviewed. The most commonly-used algorithms for each of these subsystems, along with their advantages and disadvantages, are introduced and open research areas in BMS design are reviewed. Finally, some initial experimental test results are presented to illustrate the capabilities of the testbed.

In Paper II, a reduced-order electrochemical model-based SOC estimation algorithm is proposed. The algorithm is based on a Luenberger-like observer coupled with an RLS with exponential forgetting parameter identification routine to compensate for the reduced-order model uncertainties. The asymptotic convergence of the state

estimates to their true values is proved analytically using Lyapunov Stability. Furthermore, accurate SOC estimation with low MAPE values is achieved for a wide range of C rates. It is also observed that the state estimates reach their actual values in less than one minute, despite incorrect initial state estimates for these tests. As the proposed observer does not involve any PDE solution or matrix inversion, does not require any constraints on the battery current profile, and is analytically supported by Lyapunov theorem, it can provide an accurate and reliable electrochemical model-based solution for SOC estimation.

Paper III is designated to investigate the important aspects of open-cathode fuel cells operation including their performance and modeling with the ultimate goal of designing controllers to improve the overall system performance. In this paper important performance characteristics of open-cathode fuel cells, i.e., humidity, purging, and temperature, are reviewed, and then the temperature and purging effects are investigated experimentally. Furthermore, a set of nonlinear control-oriented models is proposed specifically for air-forced open-cathode fuel cells. The effectiveness of the proposed models to capture the coupled dynamics inside the fuel cell is validated experimentally. The framework provided in this paper can be used as a foundation to develop other control methodologies to improve the efficiency and performance of the open-cathode fuel cells.

Finally, in Paper IV, temperature and voltage control problems in air-forced open-cathode fuel cells are formulated and solved for a laboratory fuel cell system. The temperature controller is shown to be able to accurately maintain the fuel cell temperature for constant and time-varying references. Also, the voltage controller is shown to result in

a constant output voltage for constant current draws, and is able to improve the transient voltage response during current density changes. The use of the voltage controller can eliminate undesirable uncertainty in the fuel cell output voltage, resulting in a fixed pre-determined polarization curve and simplifying the design of the interfacing power electronics circuitry.

2.2. FUTURE WORK

Despite an extensive number of publications in the area of Li-ion batteries and BMS design, there are still numerous research opportunities in this field, including battery State of Health (SOH) modeling and estimation, thermal modeling, and battery protection. Specially, BMS challenges specific to battery packs such as extending cell-level SOC estimation and protection to packs, optimal cell balancing, and thermal management require more rigorous research. The developed experimental research testbed can be used for electrical, thermal, and lifetime characterization of Li-ion batteries in addition to validating the effectiveness of the aforementioned BMS functionalities.

The proposed output-injection observer in Paper II can also be applied in other BMS functionalities such as SOH estimation. The identified output model uncertainties can be used as an indication of the battery SEI layer resistance. Furthermore, the state estimates obtained from the observer can be employed to provide an estimate of the total number of lithium ions inside the battery and, therefore, battery capacity, during open-circuit battery operation.

In the area of open-cathode PEM fuel cells, it was observed that the performance of the proposed voltage controller in Paper IV strongly depends on the selected voltage reference. While lower voltage references exhibit a stable performance, higher voltage set

points can result in a faster temperature rise and, therefore, the possibility of reaching high temperatures which will, in turn, result in performance degradation. Therefore, future work includes designing a switching controller to maintain the reference fuel cell voltage if the reference temperature reaches the system temperature limits. Furthermore, designing an optimal and real-time purge scheduling considering the fuel cell degradation mechanisms is another important challenge in open-cathode PEM fuel cells that needs to be studied.

Finally, the proposed output-injection adaptive observer design is a generic solution for state estimation in dynamic systems with output model uncertainty. Analytical stability proof and the effectiveness of this methodology, shown in Papers II and IV, demonstrate its potential for state estimation in other uncertain dynamic systems.

VITA

Nima Lotfi was born in Tabriz, Iran, in 1984. He earned his Bachelor of Science from Sahand University of Technology, Tabriz, Iran, in 2006 and his Master of Science from Sharif University of Technology, Tehran, Iran, in 2010. He has been a PhD student in the Mechanical and Aerospace Engineering Department of Missouri University of Science and Technology since May 2010. During his studies at the university, he worked under the supervision of Prof. Robert G. Landers and received Doctor of Philosophy in Mechanical Engineering in July 2016.